



# Mathematical Models for Guiding Pneumatic Soft Actuator Design

## Permanent link

<http://nrs.harvard.edu/urn-3:HUL.InstRepos:40050116>

## Terms of Use

This article was downloaded from Harvard University's DASH repository, and is made available under the terms and conditions applicable to Other Posted Material, as set forth at <http://nrs.harvard.edu/urn-3:HUL.InstRepos:dash.current.terms-of-use#LAA>

## Share Your Story

The Harvard community has made this article openly available.  
Please share how this access benefits you. [Submit a story](#).

[Accessibility](#)

Mathematical Models for Guiding Pneumatic Soft Actuator Design

A dissertation presented

by

Fionnuala Patricia Connolly

to

The John A. Paulson School of Engineering and Applied Sciences

in partial fulfillment of the requirements

for the degree of

Doctor of Philosophy

in the subject of

Applied Mathematics

Harvard University

Cambridge, Massachusetts

May, 2018

©2018 Fionnuala Patricia Connolly

All rights reserved.

## Mathematical Models for Guiding Pneumatic Soft Actuator Design

## Abstract

Soft actuators are the components responsible for producing motion in soft robots. Although soft actuators have facilitated a variety of innovative applications of soft robots, there is a need for design tools that can help to efficiently and systematically design actuators for particular functions. Mathematical modeling can provide quantitative insights into the response of soft actuators. These insights can be used to guide actuator design, thus accelerating the design process.

By performing finite element simulations of fiber-reinforced soft actuators, I quantify the relationship between the fiber angle of the actuators and their deformation as a function of inflation pressure. I then verify the simulation results by experimentally characterizing the actuators. By combining actuator segments in series, combinations of motions tailored to specific tasks can be achieved. I demonstrate this by using the results of simulations of separate actuators to design a segmented wormlike soft device, capable of propelling itself through a tube and performing an orientation-specific peg insertion task at the end of the tube.

Following on from this work, I then use nonlinear elasticity theory to develop analytical models of fiber-reinforced soft actuators. I present a design strategy that takes a kinematic trajectory as its input and uses the analytical models, together with optimization, to identify the optimal design parameters for an actuator that will follow this trajectory upon pressurization. I experimentally verify my modeling approach and demonstrate how the strategy works, by designing actuators that replicate the motion of the index finger and thumb.

Finally, I study a newer type of pneumatic soft actuator, made from textiles. Textiles are promising materials for soft actuators, as they are lightweight, conformable, stretchable, and intrinsically anisotropic. I perform mechanical characterization to identify textiles which have the properties necessary to produce a bending actuator. I then describe a layered lamination manufacturing approach, which allows us to quickly and easily coat textiles to make them air-impermeable, and seal them together to form an airtight pocket. I present a mathematical model of the actuators and use this model to design actuators for an assistive glove.



# Contents

|   |           |
|---|-----------|
| <b>Acknowledgements</b>   | <b>v</b>  |
| <b>1 Introduction</b>   | <b>1</b>  |
| 1.1 Motivation . . . . .  | 1         |
| 1.2 Thesis contributions . . . . .  | 2         |
| 1.3 Thesis organization . . . . .   | 2         |
| <b>2 Overview of Pneumatic Soft Actuators</b>   | <b>3</b>  |
| 2.1 McKibben actuators . . . . .  | 3         |
| 2.2 Muscle motor actuators . . . . .  | 5         |
| 2.3 Flexible microactuators . . . . .   | 5         |
| 2.4 Fiber-reinforced actuators . . . . .  | 6         |
| 2.5 Pleated pneumatic artificial muscles . . . . .  | 7         |
| 2.6 PneuNets . . . . .  | 7         |
| 2.7 Vacuum-powered actuators . . . . .  | 8         |
| 2.8 Conclusions . . . . .   | 8         |
| <b>3 Mechanical Programming of Soft Actuators by Varying Fiber Angle</b>                                    | <b>9</b>  |
| 3.1 Introduction . . . . .  | 9         |
| 3.2 Finite element analysis and model verification . . . . .  | 11        |
| 3.3 Locomotion through a tube . . . . .   | 16        |
| 3.4 Materials and Methods . . . . .   | 18        |
| 3.4.1 Finite element analysis . . . . .   | 18        |
| 3.4.2 Calculating radial stretch, axial stretch, and twist . . . . .  | 19        |
| 3.4.3 Experimental characterization . . . . .   | 22        |
| 3.5 Conclusions . . . . .   | 24        |
| <b>4 Automatic Design of Fiber-Reinforced Soft Actuators for Trajectory Matching</b>                        | <b>25</b> |
| 4.1 Introduction . . . . .  | 25        |
| 4.2 Analytical modeling of actuator segments . . . . .  | 27        |
| 4.2.1 Modeling extension, expansion, and twist . . . . .  | 29        |
| 4.2.2 Modeling bending . . . . .  | 30        |
| 4.2.3 Comparing analytical and experimental results . . . . .   | 31        |
| 4.3 Replicating complex motions . . . . .   | 33        |
| 4.3.1 Index finger motion . . . . .   | 36        |
| 4.3.2 Thumb motion . . . . .  | 37        |
| 4.4 Conclusions . . . . .   | 39        |
| <b>5 Sew-free Anisotropic Textile Composites for Rapid Design and Manufacturing of Soft Wearable Robots</b> | <b>40</b> |
| 5.1 Introduction . . . . .  | 40        |
| 5.2 Textile selection and modeling . . . . .  | 42        |
| 5.3 Actuator fabrication . . . . .  | 43        |
| 5.4 Actuator modeling . . . . .   | 44        |
| 5.5 Application to assistive glove . . . . .  | 47        |
| 5.6 Conclusions . . . . .   | 50        |

|          |  |           |
|----------|--|-----------|
| <b>6</b> | <b>Conclusions and Outlook</b>                     | <b>51</b> |
| 6.1      | Accomplishments of this thesis . . . . .           | 51        |
| 6.2      | Future work . . . . .                              | 52        |
| 6.2.1    | Forces and interactions . . . . .                  | 52        |
| 6.2.2    | Dynamic effects . . . . .                          | 53        |
| 6.2.3    | Control . . . . .                                  | 54        |
| <b>A</b> | <b>Supporting Information for Chapters 3 and 4</b> | <b>55</b> |
| A.1      | Material characterization . . . . .                | 55        |
| A.2      | Actuator fabrication . . . . .                     | 56        |
| A.2.1    | Extending/Expanding/Twisting actuators . . . . .   | 57        |
| A.2.2    | Bending actuators . . . . .                        | 58        |
| A.2.3    | Segmented actuators . . . . .                      | 59        |
| A.3      | Finite element analysis . . . . .                  | 61        |
| A.4      | Analytical modeling . . . . .                      | 61        |
| A.4.1    | Strain energy for the actuators . . . . .          | 62        |
| A.4.2    | Modeling extension, expansion, and twist . . . . . | 64        |
| A.4.3    | Modeling bending . . . . .                         | 72        |
| A.5      | Replicating finger motion . . . . .                | 78        |
| A.5.1    | Processing the input data . . . . .                | 79        |
| A.5.2    | Optimization . . . . .                             | 80        |
| A.5.3    | Glove . . . . .                                    | 81        |
| A.5.4    | Thumb actuator: reconstructing 3d motion . . . . . | 85        |
| <b>B</b> | <b>Supporting Information for Chapter 5</b>        | <b>87</b> |
| B.1      | Textile Characterization and Modeling . . . . .    | 87        |
| B.1.1    | Mechanical testing . . . . .                       | 87        |
| B.1.2    | Modeling . . . . .                                 | 91        |
| B.2      | Actuator Fabrication . . . . .                     | 93        |
| B.3      | Testing the actuators . . . . .                    | 96        |
| B.4      | Actuator Modeling . . . . .                        | 97        |
| B.5      | Application to assistive glove . . . . .           | 103       |
| B.5.1    | Articulated actuators . . . . .                    | 103       |
| B.5.2    | Glove fabrication . . . . .                        | 107       |

## Acknowledgements

I would like to thank my advisors, Professor Katia Bertoldi and Professor Conor Walsh, for their guidance, encouragement, and patience, and for fostering such friendly and collaborative environments in their groups. Thanks also to my committee members Professor Robert Howe and Professor Scott Kuindersma for their willingness to help and for their insightful comments on my thesis, and to Professor Robert Wood, Professor David Clarke, Professor Robert Howe, and Professor Luis Dorfmann (Tufts University) for the use of their lab facilities.

I am grateful to Panos Polygerinos for his energetic encouragement during the first couple of years of my PhD, to Siddharth Sanan for our weekly brainstorming meetings, and to Diana Wagner for her enthusiasm and hard work. Many people donated time and expertise to my cause over the years, including Tom Blough, Kevin Galloway, Ehsan Hajiesmaili, Sauro Liberatore, Kausalya Mahadevan, Ciarán O'Neill, Dorothy Orzel, Johannes Overvelde, Ahmad Rafsanjani, Ellen Roche, Frey Tesfaye, and James Weaver. I would like to thank all of these people and many others in the Biodesign Lab and Bertoldi Group - it was a privilege to be a part of two labs full of such welcoming, helpful, and intelligent people.

Starting grad school was a big upheaval for me and I am grateful to all my friends in the extended Conant/Perkins dorm family for going through it with me - in particular, I would like to thank Alex, Claire, Dan, Kevin, Leah, Nabiha, and Vivien. Thanks also to all the members of the Dudley Chorus 2012-2016 for brightening up Tuesday evenings. I would like to thank the occupants of Room 312 - visitors and residents alike, especially Alperen, Chris, Jozefien, Martina, Qian, Will, and Yash; here's to the ultimate Friday! I would like to thank my housemates - Christine B., Christine C., Leslie, and Ling - for helping me through the final stretch with chats, walks, and eh, semesterly workout sessions.

Thank you to Steffi for helping me endure/enjoy all the intense emotional experiences grad school has to offer; I'll always look back fondly on the Shaler Lane days.

I would like to thank my sisters, Róisín and Méabh, for their support and encouragement and my parents for all their investments in my education, from helping me with my homework in primary school, to chauffeuring me to various extra-curricular activities, to providing weekly PhD pep talks via Skype; I couldn't have done it without them.

# 1 Introduction

## 1.1 Motivation

Popular conceptions of robots include humanoid robots such as Honda's Asimo,[1] or factory robots consisting of a series of rigid links and joints. These robots operate very well in a controlled environment; they can perform very precise motions and apply very high forces. However, interacting with delicate objects, moving over uneven terrain, or encountering unexpected obstacles can be challenging for this class of robots. To address this problem, soft robots - robots made partially or completely out of soft materials - have been developed. Their intrinsic compliance makes them more suitable than their rigid counterparts for certain applications. For example, in medical or assistive applications, where robots are in close contact with humans, the compliance of soft robots makes them safer than rigid robots. However, it is also this compliance which makes soft robots difficult to control. Mathematical models can help us to overcome some of these difficulties, and this is the topic explored in this thesis.

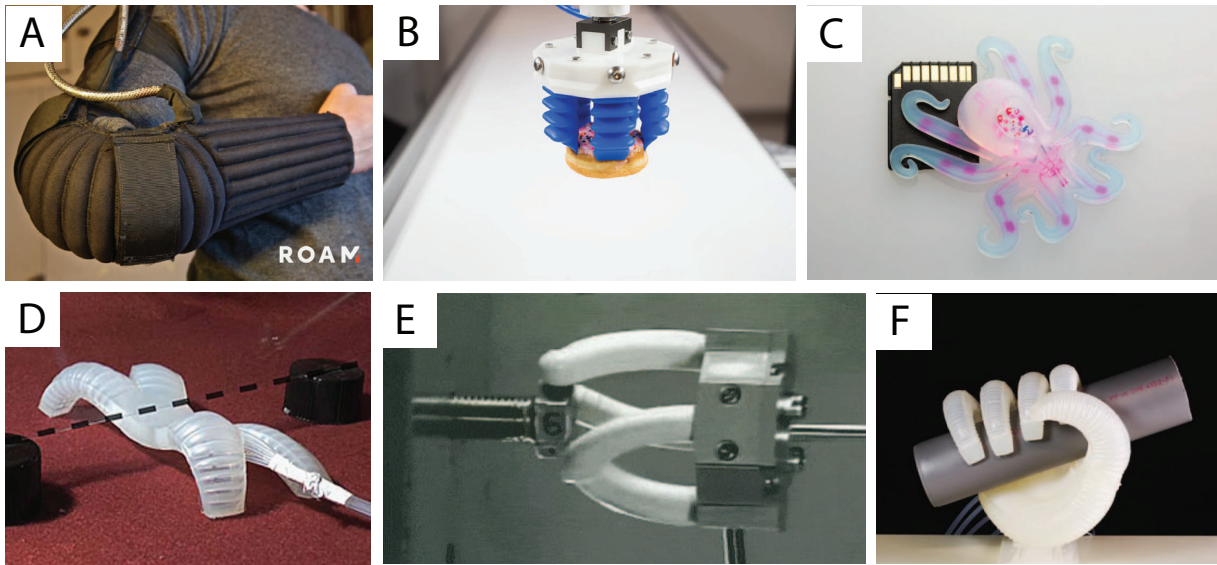


Figure 1.1: Soft robotic devices (A) fabric exoskeleton for elbow assistance[5] (B) food and beverage gripper[6] (C) a fully soft, autonomous robot[7] (D) multi-segmented soft robot[8] (E) flexible microactuators are combined to form a multi-fingered robot hand[9] (F) compliant, robotic hand capable of dexterous grasping[10]

Soft robots were conceived at least as early as the 1950s,[2] but in the last decade many more research groups have begun working on soft robotics. Soft robotic devices have accomplished tasks such as grasping, locomotion, and muscle assistance (Figure 1.1). There are many different elements

which go towards making fully-functioning soft robots; researchers have focused their efforts on developing soft actuators, soft sensors, and soft electronics, to name a few.[3, 4] This thesis focuses on soft actuators, in particular, the development of models for soft pneumatic actuators.

## **1.2 Thesis contributions**

Soft actuators are the components of soft robots which provide motion. One of the most common methods of actuation for soft robots is pneumatic pressure. While many types of soft actuators, particularly pneumatic soft actuators, have been developed, the actuator design process is mostly empirical, and based on trial and error. To make the design process more systematic and efficient, I propose the development of mathematical models for the actuators.

The main purpose of this thesis is the exploration of modeling concepts for soft actuators, to guide their design. Without reliable modeling approaches, soft actuator design is based on empirical guidelines and trial and error. By developing models of soft actuators, we gain information ahead of time about how the behavior of the actuator depends on its geometry and the materials used. Actuator models can be used either for design purposes or for actuator control. In the current work, however, I focus on the use of models for actuator design, with the goal of informing and streamlining the design process.

## **1.3 Thesis organization**

The following chapter presents a survey on the main types of pneumatic soft actuators which have been developed, and a summary of the major modeling achievements thus far. Chapter 3 describes the use of finite element analysis to explore the design space of fiber-reinforced elastomeric actuators. I examine the effect of fiber angle on actuator behavior and use the insights gained from the models to create a worm-like device which locomotes through a tube. Chapter 4 describes analytical models which are used to further explore the design space of fiber-reinforced elastomeric actuators. These models are then used to design actuators which follow specified trajectories. Chapter 5 presents a different type of soft actuator, made from textiles. I describe methods for rapidly manufacturing and modeling these actuators and demonstrate the application of these methods to the development of a glove which mimics hand motion. Finally, in the conclusions, I summarize the contributions of the thesis and give some recommendations for future directions for the field.

## 2 Overview of Pneumatic Soft Actuators

Over the last seventy years or so, many different types of soft actuators have been developed. Some are made from electroactive polymers,[11, 12] some use shape memory alloys,[13] but the most commonly used soft actuators are those which are pneumatically actuated, and this type of actuator will be the focus of the remainder of this thesis. The first soft actuator, called a pneumatic artificial muscle, or McKibben actuator (or sometimes referred to as a braided fluid actuator), was developed in the 1950s.[14] The actuator consists of an elastomeric bladder surrounded by a braided mesh, and upon pressurization, it undergoes radial expansion and axial contraction, similar to a contracting muscle (Figure 2.1A). From the beginning, soft actuators were developed with medical applications in mind; McKibben developed the pneumatic artificial muscle as an assistive device for his daughter, whose hands had been paralyzed by polio. While the McKibben actuator is still the most well-known type of soft actuator, many more types of pneumatic soft actuators have since been developed. The main pneumatic soft actuators and the different approaches taken to modeling them will be outlined in the rest of this chapter.

### 2.1 McKibben actuators

McKibben actuators are the most developed type of soft actuator, and a lot of work has been done on modeling them. The earliest work was that by Schulte,[14] which focused on characterization of the actuators. It presented data on the relationship between applied internal pressure, actuator length, and force output, as well as examining the effect of different parameters, such as thickness of fibers in the braided mesh, on performance of the actuator. Between the 1960s and 1980s, the McKibben actuator fell out of use and efforts to model such actuators stopped. However, when the actuator was commercialized by the Bridgestone Corporation in the form of the Rubbertuator[15] in the 1980s, there was renewed interest in modeling its behavior. Chou and Hannaford[16, 17] used an energy conservation approach to find the relationship between actuator geometric parameters, applied pressure, and output force. This yielded the now well-known result that the actuator reaches a locked configuration when the angle between the fibers reaches  $35.3^\circ$ . At this point, increasing the applied pressure stiffens the actuator, but no further deformation is possible. Chou and Hannaford also performed tension-pressure-displacement experiments

to investigate the behavior of the actuators and to examine the hysteresis in their response (due to Coulomb friction). This work was expanded upon in later studies such as Klute and Hannaford,[18] where the material properties of the bladder were included in the model. Over time, researchers developed more and more detailed models of McKibben actuators, accounting for end effects from the actuator terminations, the effects of the fibers stretching, and the effect of braids on maximum actuator contraction.[19, 20, 21] These models gave more accurate predictions of actuator behavior, particularly for predicting forces at higher extensions. The operation of the McKibben actuator and many of the models developed for it have been outlined in an article by Tondur and Lopez[22] and a review paper by Tondur.[23]

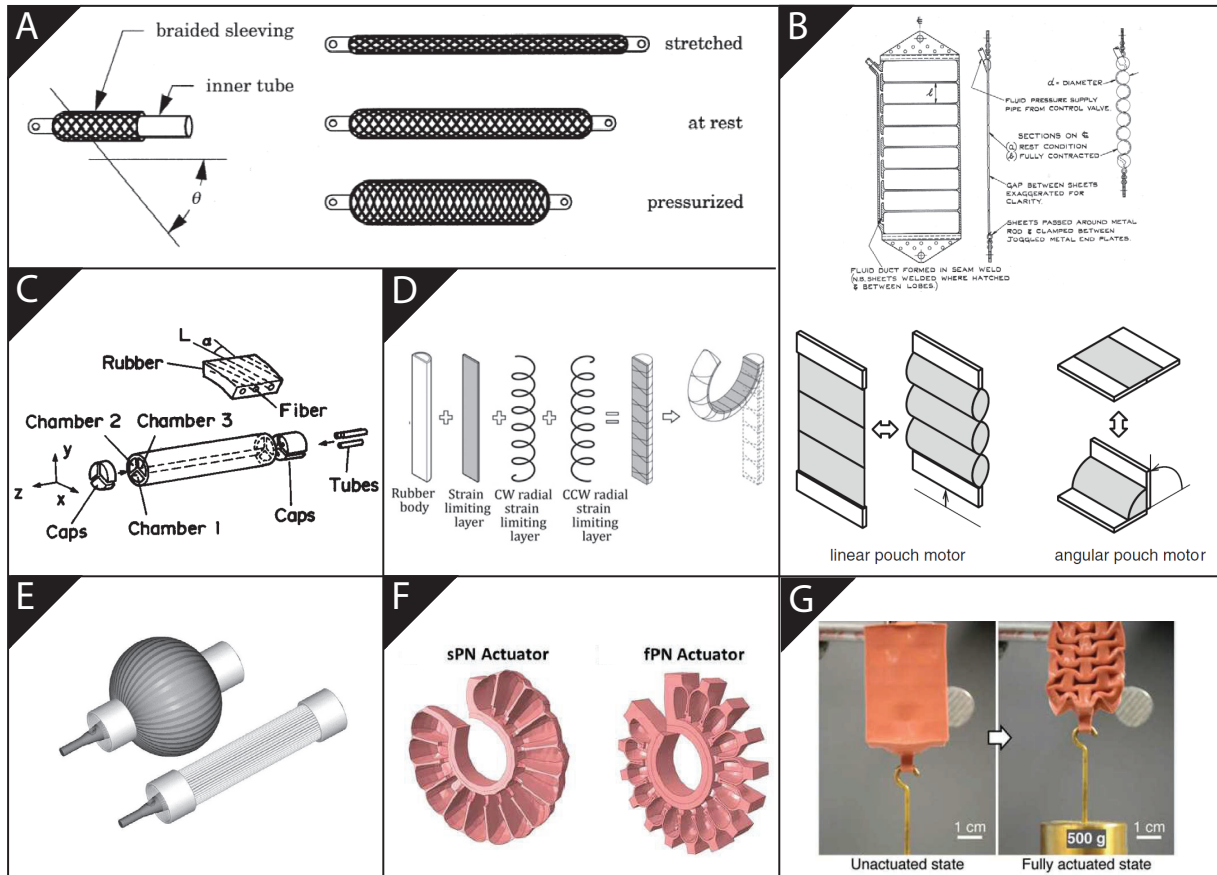


Figure 2.1: (A) Left: McKibben actuator, consisting of an inner tube surrounded by a braided mesh with braid angle  $\theta$ . Right: Actuator contracts when pressurized, and can be extended by applying a force on the ends.[24] (B) Top: Muscle motor actuator[25] Bottom: Pouch motors[26] (C) Flexible microactuator[27] (D) Fiber-reinforced bending actuator[28] (E) Pleated artificial muscle, in relaxed and pressurized configurations[24] (F) Left: original PneuNet actuator Right: fast PneuNet actuator[29] (G) vacuum-actuated muscle-inspired pneumatic structure[30]



While these models have given many insights into how to improve actuator design, modeling McKibben actuators is still an active area of study, as the optimal method of controlling these actuators is still under investigation. Despite all the work that has been done, the many complexities of these actuators, such as friction of fibers, interactions between the bladder and the braid, and nonlinear material behavior, mean that there is still no consensus on an accurate, reliable model for McKibben actuators; this illustrates how difficult a problem it is to model soft actuators.

## 2.2 Muscle motor actuators

Around the same time as the McKibben actuator was developed, muscle motor actuators were introduced by Mettam.[25] These consisted of a series of fabric pouches sewn in a rectangular shape, with a balloon placed in each pouch. More recently, this class of actuators, now known as pouch motors has been expanded to include both linear actuators and torsional actuators (see Figure 2.1B). These newer actuators are fabricated from polyethylene sheets, using heat to seal the edges of the pouches. For both muscle motors and pouch motors, simple geometric relationships and energy conservation principles are used to derive relationships between the applied pressure in the actuator, the contraction of the actuator, and the output force of the actuator. Since these relationships are derived without accounting for effects such as stretching of the material in the actuator, they are less accurate at higher pressures, particularly for the pouch motors, as the polyethylene is a relatively stretchable material. However, despite the model being less accurate, the pouch motors have an advantage over muscle motors in that they are much easier to fabricate. Furthermore, Niiyama et al introduced an automated design algorithm for pouch motors.[31] This algorithm can design a sheet which folds in a particular way when actuated. The user prescribes the required fold pattern, and the algorithm uses graph theory to output the appropriate placement of pouches and air channels to achieve these folds.

## 2.3 Flexible microactuators

Flexible microactuators (FMAs) were introduced by Suzumori et al in the late 1980s.[27, 9, 32] FMAs are fiber-reinforced elastomeric tubes, which have three internal chambers. These chambers can be inflated one by one, causing the actuator to bend in different directions, or they can be inflated simultaneously to get actuator extension (see Figure 2C). To gain insight into the behavior



of the FMAs, the authors performed a linear analysis of the deformation and force as functions of pressure. They verified the validity of their model for small deformation, but found that a fully nonlinear finite element analysis was required to capture larger deformations. To allow fabrication using stereo-lithography, Suzumori et al changed the FMA design. Instead of using fibers as the radial constraint, they introduced internal beams to restrict the radial expansion of the actuator[32]. Similar actuators were investigated by Elsayed et al,[33] who performed FEA on elastomeric actuators with restraining beams to find the optimal actuator design. They optimized actuator wall thickness and cross-section geometry to reduce actuation pressure, distribute stress evenly, and reduce radial ballooning.

## 2.4 Fiber-reinforced actuators

While fiber-reinforced actuators were first proposed by Suzumori et al in the form of FMAs, they have been further investigated by many other researchers. Hirai et al were the first to introduce methods to systematically design these actuators for specific purposes.[34] They considered the actuators to be elastic shells, with mechanical constraints in the form of fibers, and used constraint topology to analyze the motions that were possible for actuators with different constraints. This led to a qualitative description of the type of motions possible from these actuators (e.g. bending, extending, twisting). The actuators have a limitation in that, since they have only one internal chamber, each actuator can produce only one type of motion. In a later paper, Hirai et al circumvented this problem by combining single motion elastic tubes in groups, so that each group could produce different types of motions by inflating different combinations of the tubes.[35]

Recently, there has been increased interest in modeling fiber-reinforced actuators. Generalized fiber-reinforced actuators, consisting of a tube surrounded by two families of fibers, were patented by Bishop-Moser et al.[36] They modeled the kinematics and kinetostatics of these actuators, thus exploring the effect of fiber angle on the type of deformation (extension, expansion, twisting, or a combination of these motions) undergone by an actuator[37, 38] when it is pressurized. Bending fiber-reinforced actuators have also been explored in detail. There are three main ways in which bending can be achieved:

1. asymmetric inflation, as employed by Suzumori et al[27]

2. different fiber angles on opposite sides of the actuator.[39] Finite element analysis has been used to explore some design parameters for these actuators, such as actuator diameter and position of the fiber layer.[40]
3. non-uniform tube stiffness.[28, 41] The deformation response and force output of these actuators has been modeled analytically.

Finally, wrapped soft pneumatic artificial muscles (WSPAM) are presented in Memarian et al.[42] These actuators operate on the same principle as fiber-reinforced actuators, as they consist of an elastomeric tube surrounded by a relatively inextensible patterned sheet. They propose a linearized model of the system, relating the bend angle of the actuators to the internal applied pressure.

## 2.5 Pleated pneumatic artificial muscles

Daerden and Lefeber have outlined many variations on the McKibben actuator in their review paper.[24] One such variation is the pleated pneumatic artificial muscle (PAM).[43] The membrane of this actuator has pleats in the axial direction which unfold when the actuator is pressurized. This allows the actuator to deform while inducing minimal stress and strain in the membrane. Expressions for the deformation and force output for this actuator can be derived in a similar manner as for the McKibben actuators. The idea of reducing strain in soft actuators is gaining traction, with the development of inflatable textile actuators; both torsional and bending actuators have been developed.[44, 5] These actuators inflate to take on a shape which is pre-defined by the geometry of the material. As well as operating at reduced strains, they have an advantage in that they have a very small volume when not actuated (in contrast, for example, to elastomeric actuators, which are much bulkier).

## 2.6 PneuNets

A popular type of actuator, termed PneuNets, was developed by the Whitesides Research Group.[45] These actuators consist of multiple elastomeric chambers connected in series, with a layer of inextensible material on one side of the actuator. The difference in stiffness between opposite sides of the actuator causes it to bend when inflated. This type of actuator has been modeled by treating

the actuator as a rod and using Euler’s elastica theory, together with some experimental results, to predict the shape of the actuator under various pressure and end-loading conditions. However, even this very simple approach yields a very complicated relationship between the bending moment of the actuator and its curvature or shape.

Many variations on PneuNet actuators have been developed, such as fast PneuNets (fPN)[29] and soft pneumatic actuators (SPA).[46, 47] SPAs have been modeled using finite element analysis and these models have been used in a design algorithm to design actuators for specific functions.[48]

## 2.7 Vacuum-powered actuators

While the majority of soft pneumatic actuators are actuated using positive pressure, some researchers have explored the idea of using negative pressure for actuation. Wakimoto et al developed a bidirectional pneumatic bending actuator. This elastomeric actuator had an asymmetric structure (flat on one side, bellows on the opposite side) which caused it to bend in one direction under positive pressure, and in the opposite direction under negative pressure.[49] They used finite element analysis to explore three different designs for the actuator. More recently, Yang et al have developed an elastomeric actuator which experiences beam buckling under negative pressure and thus reduces its volume, producing a contraction motion.[30, 50] These actuators therefore produce a muscle-type motion when actuated, but in contrast to McKibben actuators, they undergo no radial expansion when actuated and run no risk of rupture due to over-pressurization.

## 2.8 Conclusions

Many types of pneumatic soft actuators have been developed, demonstrating the utility and versatility of this class of actuator. Many approaches have been taken to model these actuators, but the large deformations involved, the actuator compliance, and the nonlinearity of the materials makes modeling the deformation response and the interaction response a complex problem. Finite element analysis yields the most accurate results, but is very time-consuming, while analytical modeling requires careful choice of assumptions and approximations to get tractable but accurate results. The development of models to guide the design of soft actuators therefore remains a significant challenge.

### 3 Mechanical Programming of Soft Actuators by Varying Fiber Angle

F. Connolly, P. Polygerinos, C. J. Walsh and K. Bertoldi, *Soft Robotics*, **2(1)**, 26-32, 2015

#### 3.1 Introduction

In recent years, significant attention has been devoted to the study of soft, fluidic actuators, because of their compliance, easy fabrication, and ability to achieve complex motions with simple control inputs.[49, 45, 51, 52, 53, 54] These unique capabilities have led to a variety of innovative potential applications in the areas of medical devices,[55, 56] search and rescue devices,[4] and assistive robots.[57] One of the most well-known and widely used pneumatic soft actuators is the McKibben actuator,[14, 58, 17] which upon pressurization produces a simple axial contraction and radial expansion motion. This actuator has been studied in detail and has been shown to have many uses.[21, 59, 60] However, in order to increase the applicability of soft robots, it is desirable to have access to a library of actuators capable of producing a much wider range of motions. In an effort to increase functionality in soft actuators, multiple McKibben actuators have been combined to produce more complex twisting motions.[55, 61] Furthermore, bending motions have been achieved using PneuNets[45, 51, 52, 53] and flexible microactuators,[27] and a wider range of motions, including extension, twisting, and bending, has been demonstrated by using fillers (paper or fabric) in elastomer composites,[52] fiber-reinforced elastomers,[27] and combinations of elastomers with different stiffnesses.[62] However, in order to simplify and accelerate the design of soft robots, there is still a need to develop actuators that can be easily fabricated and designed and easily programmed to produce a wide range of motions, and that can be used as building blocks to realize more complex motions, such as locomotion and burrowing.

We looked to nature for inspiration for the realization of such actuators and noted that fiber-reinforced structures are ubiquitous. For example, nemertean and turbellarian worms have an outer layer of helically arranged collagen fibers to limit the elongation and contraction of the worms body,[63, 64] and the walls of arteries are strengthened with a helical arrangement of collagen fibrils.[65] Moreover, fiber-reinforced structures in nature often function as actuators. Examples

include the body of the earthworm,[66] the tube feet of starfish,[67] and soft muscular systems of the human body, such as the heart.[55] Furthermore, we notice that the nonlinear theory of anisotropic tubes[68, 69, 70, 71] and, more recently, simple kinematics models[72, 73] have shown that pressurized fiber-reinforced hollow cylinders are capable of many motions, including axial extension, radial expansion, and twisting.

In this chapter, we explore numerically and experimentally the response of fluidic-powered cylindrical elastomeric actuators, with fibers wound in a helical pattern around the outside of the actuator, as shown in Figure 3.1A and 3.1C. While previous work has demonstrated that this type of fiber-reinforced actuator is capable of many types of motions,[55, 56, 14, 58, 17, 21, 59, 60, 61, 27, 72, 73] here we study in detail the effect of fiber angle (the angle between the horizontal axis and the fiber) on actuator motion. Our results indicate that, by simply varying the fiber angle, we can program the actuators to achieve a particular change in length, change in radius, or twist about their axis (see Figure 3.1B) as a function of pressure. We also investigate, through the use of finite element models, how using multiple families of fibers (i.e., fibers arranged at different angles), can expand the actuator design space, leading to greater flexibility in the type of actuator we can create. We show that these systems can be efficiently designed using numerical simulations, which enable rapid exploration of the design space. Furthermore, by combining actuator segments in series, as shown in Figure 3.1D, for example, we can achieve combinations of motions tailored to specific tasks, such as peristaltic locomotion and burrowing.

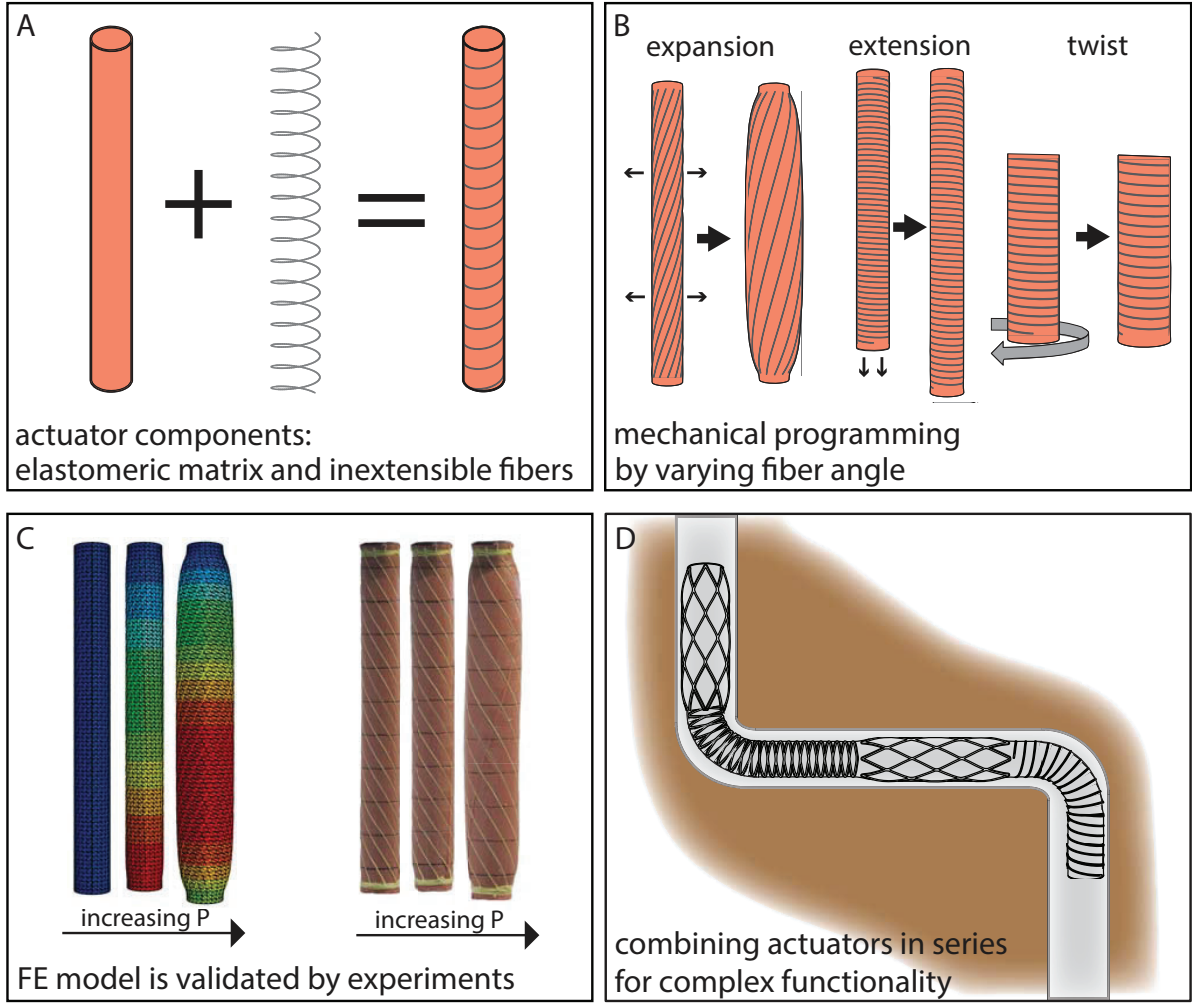


Figure 3.1: Fiber-reinforced soft actuators. (A) The actuators consist of an elastomeric matrix surrounded by a helical arrangement of fibers. (B) The actuators can expand, extend, or twist upon pressurization. (C) A combination of finite element modeling and experimental characterization is used to explore the motions that can be achieved. (D) Combining actuator segments in series, we can achieve combinations of motions tailored to specific tasks. For example, we can combine extending and expanding segments to create a robot capable of navigating through a pipeline.

### 3.2 Finite element analysis and model verification

To characterize the effect of fibers on the response of the actuators, we begin by studying them numerically using finite element analysis. Such an approach facilitates accurate modeling of the system, incorporating material properties and the effect of the fiber reinforcement. It also enables much more rapid exploration of the design space compared with fabricating and experimentally characterizing multiple actuators, and therefore can be effectively used to design actuators tailored

to specific tasks. We used the commercial finite element package Abaqus, version 6.12-1 (SIMULIA, Providence, RI), to run simulations for actuators with a range of different fiber angles, varying from  $0^\circ$  (circumferential fibers) to  $90^\circ$  (axial fibers) (see Section 3.4 for details of how the simulations were performed). During the simulations, we monitored (1) the change in the radius of the actuator ( $b/B$ ), (2) the change in length of the actuator ( $\lambda_z = l/L$ ), and (3) the amount by which the actuator twists about its longitudinal axis ( $\tau$ ) (see Section 3.4 for details on how to extract these quantities from the simulations).

We first focus on actuators with a single family of fibers (i.e., all fibers have the same orientation), and in Figure 3.2A we plot  $\lambda_z$ ,  $b/B$ , and  $\tau$  as a function of the applied pressure for fiber angles varying from  $\alpha = 0^\circ$  to  $\alpha = 90^\circ$ . As expected, for  $\alpha = 0^\circ$ , corresponding to circumferential fibers, the motion of the actuator is constrained only in the radial direction, and so we see in the plot of axial extension versus pressure that maximum axial extension occurs for this angle. As  $\alpha$  is increased from  $0^\circ$ , radial expansion increases and axial extension decreases until finally, at  $\alpha = 90^\circ$  (axial fibers), we have maximum radial expansion and no axial extension. We also see that for fiber angles in the  $50^\circ$  to  $90^\circ$  range, the axial stretch is nonmonotonic, as the length of the actuator first decreases and then increases as pressure increases. Finally, by plotting twist per unit length as a function of pressure, we note that at  $0^\circ$  and  $90^\circ$ , the fibers are arranged symmetrically, and so there is no twist about the axis. We also see the unintuitive result that twist peaks around  $30^\circ$ .

To verify the finite element results, we compared numerical predictions and experimental data for two actuators characterized by  $\alpha = -3^\circ$  and  $\alpha = 70^\circ$ . From the finite element analysis, we expect that these actuators will exhibit contrasting behavior upon pressurization. Upon completion of the fabrication (see Appendix A for details), we pressurized each actuator to  $62.05kPa$  and took pictures of the actuator during the loading process. By tracking markings on the actuator (see Figure 3.2B and 3.2C), we could analyze the change in radius

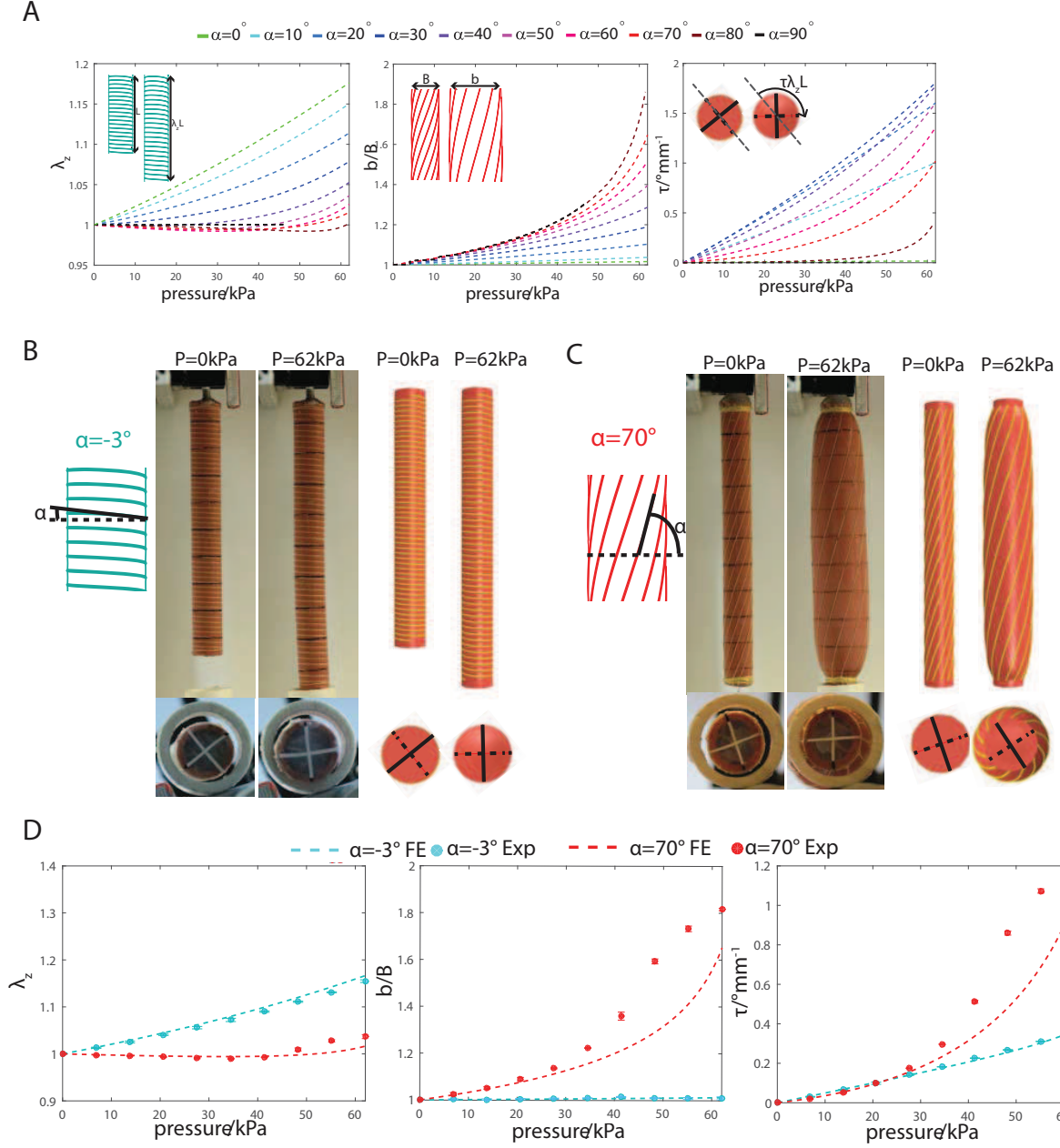


Figure 3.2: Actuators with one family of fibers. (A) Finite element method results showing extension ( $\lambda_z$ ), expansion ( $b/B$ ), and twist per unit length ( $\tau$ ) as a function of the applied pressure for a range of different fiber angles. Note that we define the positive fiber orientation to be in the clockwise direction. Positive fiber orientation induces twist in the counter-clockwise direction (negative twist). However, here we are interested in comparing the magnitude of the twist for different angles, and so we plot the magnitude of the twist (rather than magnitude and direction). (B) Photographs from experimental characterization (left) and snapshots from finite element simulation (right) for an actuator with fiber angle  $\alpha = -3^\circ$ . Both front views (top) and bottom views (bottom) are shown. (C) Photographs from experimental characterization (left) and snapshots from finite element simulation (right) for an actuator with fiber angle  $\alpha = 70^\circ$ . (D) Comparison between finite element simulations and experiments for two actuators with fiber angle  $\alpha = -3^\circ$  and  $\alpha = 70^\circ$ . Error bars show the standard deviation from the mean result obtained by pressurizing each actuator three times.



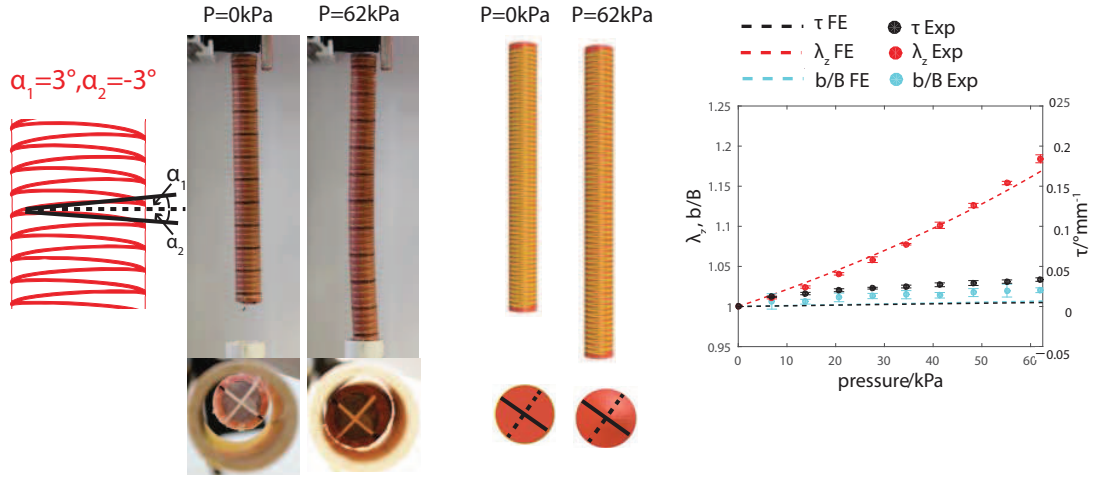
and length. To obtain values for the twist, we placed a camera underneath the actuator and used markings to track the center and four points on the circumference of the bottom of the actuator.

In the same way as for the finite element simulations, we plotted the axial stretch, circumferential stretch, and twist per unit length, as functions of pressure (see Section 3.4 for details). The results are reported in Figure 3.2D. In the case of  $\alpha = -3^\circ$ , we see excellent agreement between experimental and numerical results. For  $\alpha = 70^\circ$ , the match is very good at lower pressures, with some deviation at higher pressures due to the highly nonlinear response exhibited by the actuator. In particular, for  $\alpha = -3^\circ$  we see that the actuator twists about its axis and extends axially, with little change in the radial dimension. In contrast, for  $\alpha = 70^\circ$  the actuator twists, expands radially, and undergoes slight axial contraction in response to pressurization. Finally, we note that the discrepancies between the numerical and experimental results are likely due to imperfections in the experiments, and end effects that lead to nonuniform deformations. Having verified the finite element results, we can use the graphs in Figure 3.2A to design an actuator that maximizes or minimizes extension, expansion, or twist. Also, by combining the results from the three graphs, we can design actuators with specific characteristics, such as an actuator that maximizes twist while minimizing change in radius, or one that maximizes twist and extension.

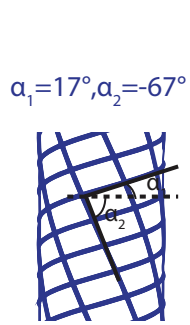
Although varying the fiber angle of an actuator yields a range of different motions, there are some motions that are more difficult to achieve than others. For example, a pure extending actuator requires a fiber angle of  $0^\circ$ , but achieving this in practice is difficult due to variations in the fabrication process. To overcome this issue, we can add a second family of fibers to the first one. This second family of fibers can be arranged at any angle, leading to a variety of different motions that can be achieved. However, note that if we arrange the two families of fibers symmetrically, there is no twist; the actuator purely extends or expands.

We demonstrate this by characterizing an actuator with fibers arranged at  $\alpha_1 = 3^\circ$  and  $\alpha_2 = -3^\circ$ . We see in Figure 3.3A that the behavior in the axial and radial directions is very

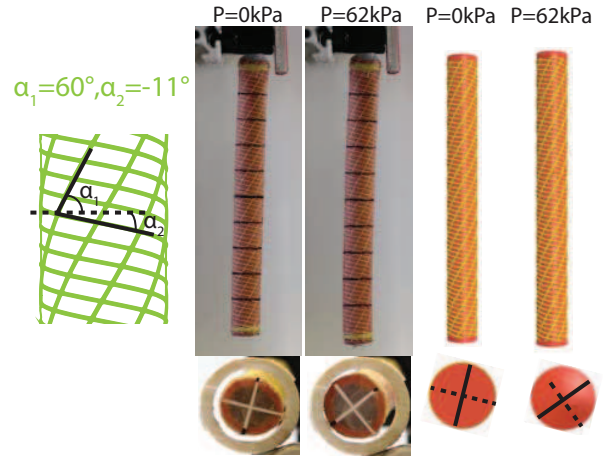
### A symmetric fibers



### B asymmetric fibers



### C asymmetric fibers



### D

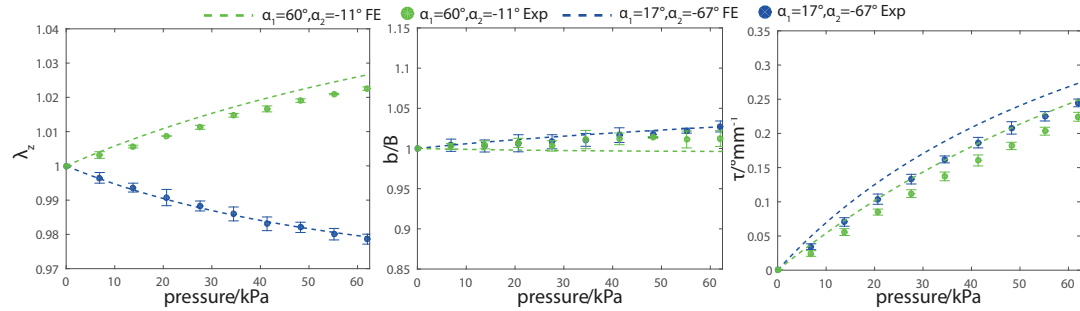


Figure 3.3: Actuators with two families of fibers. Error bars show standard deviation from mean result obtained by pressurizing each actuator three times. (A) Photographs (left), finite element analysis snapshots (center), and comparison between finite element and experimental results (right) for an actuator with fibers symmetrically arranged at  $\alpha_1 = 3^\circ$  and  $\alpha_2 = -3^\circ$ . (B) Photographs (left) and finite element analysis snapshots (right) for an actuator with fibers at  $\alpha_1 = 17^\circ$  and  $\alpha_2 = -67^\circ$ . (C) Photographs (left) and finite element analysis snapshots (right) for an actuator with fibers at  $\alpha_1 = 60^\circ$  and  $\alpha_2 = -11^\circ$ . (D) Comparison between finite element and experimental results for an actuator with fibers at  $\alpha_1 = 17^\circ$  and  $\alpha_2 = -67^\circ$  and an actuator with fibers at  $\alpha_1 = 60^\circ$  and  $\alpha_2 = -11^\circ$ .

similar to the case with only one family of fibers (axial extension and slight radial expansion), but now the new family of fibers cancels the twist.

As well as yielding an actuator that does not twist, adding a second family of fibers also expands the design space for this class of actuators. For instance, we can fabricate multiple actuators that have similar twist per unit length as a function of pressure, but different behavior in the axial and radial directions. We performed a range of finite element simulations and identified a pair of actuators that exhibit this behavior: an actuator with fibers at  $\alpha_1 = 17^\circ$  and  $\alpha_2 = -67^\circ$ , and one with fibers at  $\alpha_1 = 60^\circ$  and  $\alpha_2 = -11^\circ$ . In Figure 3.3B, we compare the response, both experimental and numerical, of these two actuators. We see that the two actuators have almost the same curve for twist as a function of pressure and neither sees much change in radius. However, one actuator extends upon pressurization, while the other contracts. So we see that adding an extra family of fibers expands the design space, giving us greater flexibility in the type of actuator we can create.

### 3.3 Locomotion through a tube

The actuators presented here have potential to be used in a wide variety of applications. For example, we can combine them to fabricate a device capable of propelling itself through a tube with a  $90^\circ$  bend in it and performing an orientation-specific peg insertion task at the end. To design such a device, we took inspiration from the peristaltic locomotion of the earthworm.[66] The earthworm uses longitudinal and circumferential muscles to contract the segments of its body sequentially, enabling it to move forward. Therefore, we assembled four actuators in series, as shown in Figure 3.4A, with segments 1, 2, and 3 responsible for propelling the device through the tube and segment 4 designed to twist the prongs into the holes.

More specifically, actuator segments 1 and 3 were required to expand and anchor the device in the tube, and so we chose to arrange the fibers symmetrically at  $70^\circ$  and  $-70^\circ$  to

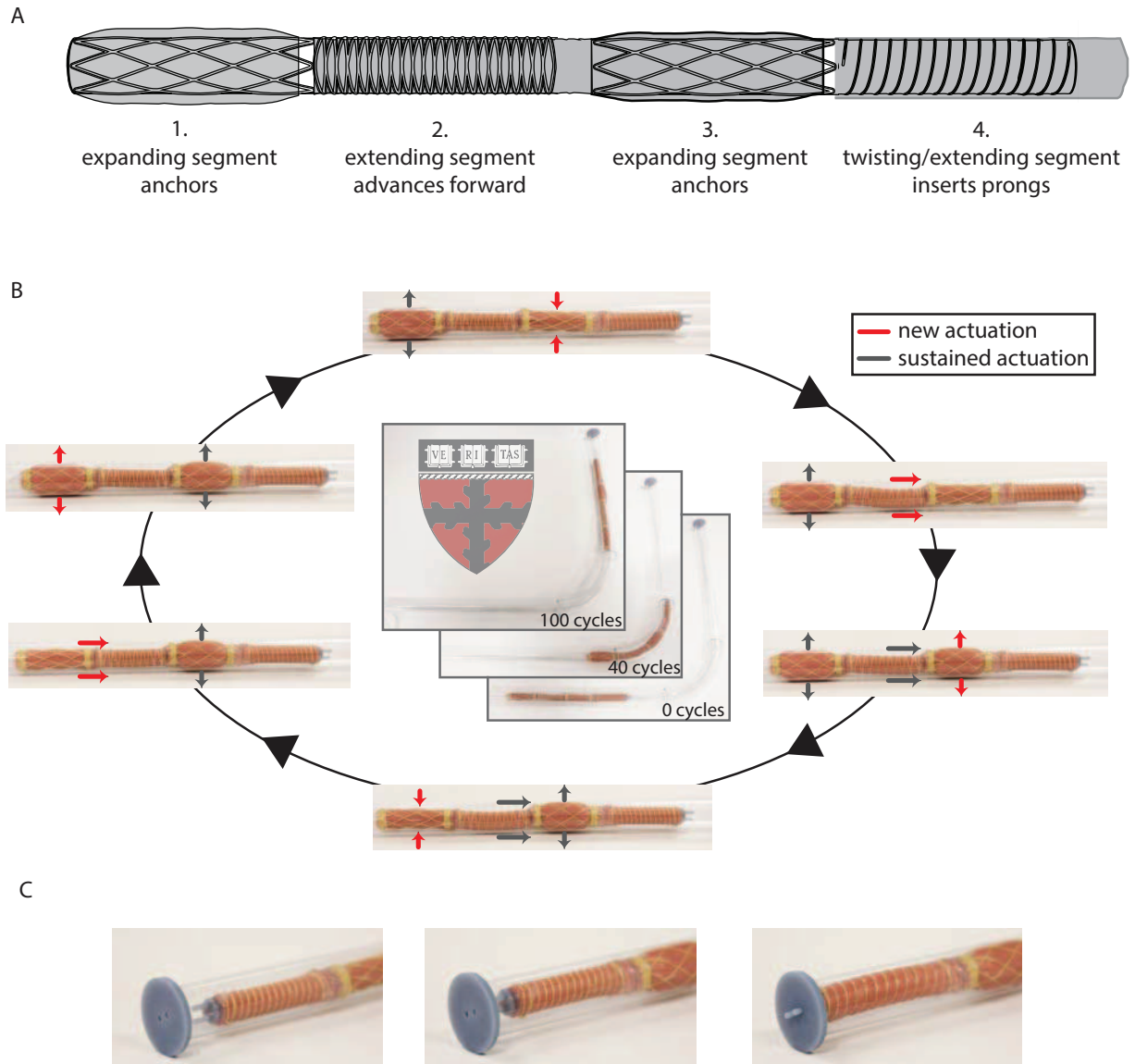


Figure 3.4: Device capable of propelling itself through a tube and performing an orientation-specific task. (A) Four actuator segments are combined in series to achieve forward locomotion and perform an orientation-specific task. (B) Segments 1, 2, and 3 are actuated in sequence to move the device through a bent tube. (C) As the device approaches the end of the tube, the prongs are not aligned with the holes. Segment 4 is then actuated, extending and twisting the prongs into the holes.

achieve a balance between maximum expansion and ease of fabrication. To choose the dimensions of the actuators, we took advantage of finite element analysis. Considering a tube with an inner diameter of  $13\text{mm}$ , we performed a range of finite element simulations and found that an actuator with an outer diameter of  $8\text{mm}$ , a wall thickness of  $1\text{mm}$ , and fibers symmetrically arranged at angles of  $70^\circ$  and  $-70^\circ$  would expand to give an outer diameter of  $14.5\text{mm}$  at a pressure of  $100\text{kPa}$ ,

and this would be sufficient to act as an anchor. In contrast to the anchoring segments, the function of segment 2 was to achieve extension and move the device forward, and so we arranged the fibers symmetrically at  $7^\circ$  and  $-7^\circ$ .

The actuation sequence required for forward locomotion is shown in Figure 3.4B. Each segment of the device is actuated independently. When we actuate segment 1, it expands and anchors the device in the tube. Segment 2 extends to move the device forward. Segment 3 expands to anchor the device in the forward position, and we can then depressurize segments 1 and 2. It is key to note that, since all of the segments are completely soft, the bend in the tube is easily negotiated (see Figure 3.4B center). This would be much more difficult to achieve if rigid components were used.

When the device reaches the end of the tube, we then want it to insert the two prongs at its front into two holes. Since the prongs are typically misaligned (see Figure 3.4C), we actuate segment 4, whose fibers are arranged asymmetrically, at an angle of  $10^\circ$ , to achieve a balance of extension and twisting. As shown in Figure 3.4C, the prongs easily twist into the holes and we can use segments 1, 2, and 3 to adjust the position of the device if necessary. Since the device has intrinsic passive compliance, even if the front segment is not exactly centered in the tube, the prongs still find their way into the holes.

We highlight the utility of knowledge gained from the simulations by mechanically programming multiple soft actuator segments and combining them in series to create a wormlike soft device that can navigate through a pipe and complete a simple insertion task. The ability to understand how tailoring of the fiber angle influences the pressurization response of the soft actuators enables rapid exploration of the design space for this class of soft actuators and the iteration of exciting soft robot concepts such as flexible and compliant endoscopes, pipe inspection devices, and assembly line robots, to name but a few.

## 3.4 Materials and Methods

### 3.4.1 Finite element analysis

All finite element simulations were performed using the commercial finite element software Abaqus (SIMULIA). The elastomer (Elastosil M4601 - Wacker Chemie AG) was modeled as an incompressible neo-Hookean material (See Appendix A for material properties). The Kevlar fibers were

modeled as a linearly elastic material using the manufacturers specifications: diameter  $0.1778mm$ , Youngs modulus  $31.067 \times 10^6 kPa$ , and Poissons ratio  $0.36$ . Each actuator had inner radius  $6.35mm$ , wall thickness  $2mm$ , and length  $165mm$ . The density of fiber distribution was approximately  $0.36mm$  of fiber per  $mm^2$  of elastomer. For the elastomer, 20-node quadratic brick elements, with reduced integration (Abaqus element type C3D20R), were used, and 3-node quadratic beam elements (Abaqus element type B32) were used for the fibers. The accuracy of the mesh was ascertained through a mesh refinement study and perfect bonding between the fibers and the elastomer was assumed (the fibers were connected to the elastomer by tie constraints). Each simulation required 16,000 elements and 30,000 nodes. Quasi-static nonlinear simulations were performed using Abaqus/Standard. One end of the actuator was held fixed, and a pressure load of  $62kPa$  was applied to the inner surface of the actuator. For two cases ( $\alpha = 80^\circ$  and  $\alpha = 90^\circ$ ), the quasi-static simulations were unstable at higher pressures. Therefore, dynamic simulations were performed for these actuators using Abaqus/Explicit and quasi-static conditions were ensured by monitoring the kinetic energy and introducing a small damping factor. The chamber of the actuator was modeled as a fluid-filled cavity, and thermal expansion was used to increase the volume of air inside the cavity. The resulting pressure in the cavity was output, as were the coordinates of the nodes on the outer surface of the actuator, as before.

### 3.4.2 Calculating radial stretch, axial stretch, and twist

To calculate the average radial stretch, axial stretch, and twist per unit length of the actuator as a function of the applied pressure, the coordinates of each node on the outer surface of the actuator were output and we focused on the nodes located on two diametrically opposite longitudinal lines, as shown in Figure 3.5A.

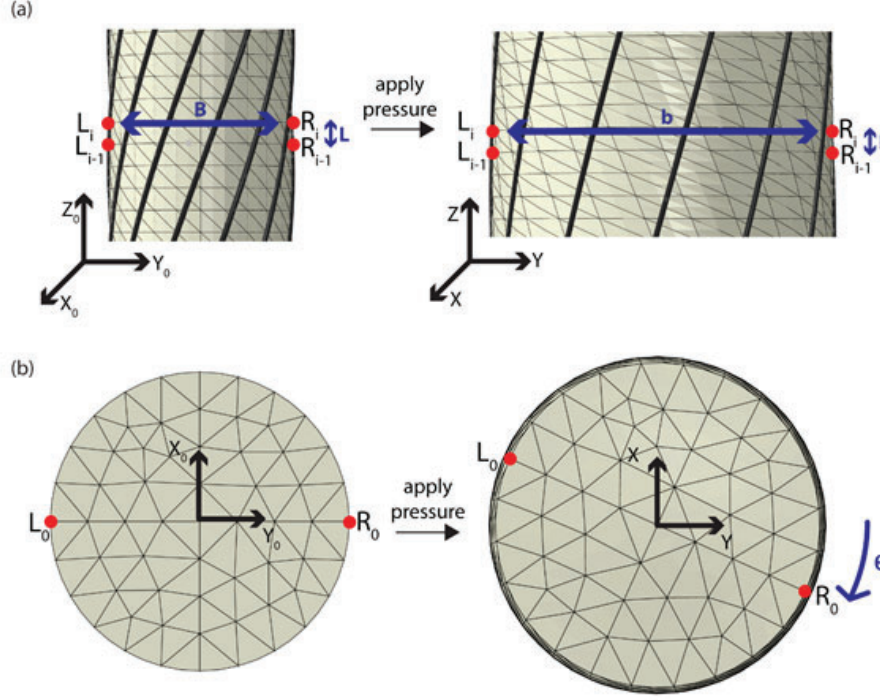


Figure 3.5: Extracting extension, expansion and twist from the FE simulations. (A) Pairs of diametrically opposite nodes are used to calculate the radial stretch. Pairs of nodes along the length of the actuator are used to calculate the axial stretch. (B) The coordinates of a node on the bottom face of the actuator are tracked to calculate the twist

If we denote with  $L_i$  and  $R_i$  a pair of nodes located on these two lines and characterized by the same initial longitudinal coordinate (i.e.,  $Z_0^{R_i} = Z_0^{L_i}$ ), then the stretch in the radial direction can be calculated as

$$(\lambda_\phi)_i = \frac{\sqrt{(X^{R_i} - X^{L_i})^2 + (Y^{R_i} - Y^{L_i})^2}}{\sqrt{(X_0^{R_i} - X_0^{L_i})^2 + (Y_0^{R_i} - Y_0^{L_i})^2}} \quad (3.1)$$

where  $(X_0^A, Y_0^A, Z_0^A)$  and  $(X^A, Y^A, Z^A)$  denote the coordinates of node  $A$  in the undeformed and deformed configuration, respectively. Moreover, the axial stretch for each pair of nodes can be calculated as

$$\lambda_{Z_i} = \frac{Z^{R_i} - Z^{R_{i-1}}}{Z_0^{R_i} - Z_0^{R_{i-1}}} \quad (3.2)$$

Finally, as shown in Figure 3.5B, the twist can be calculated as

$$\theta = \tan^{-1} \frac{X^{R_0} - X_0^{R_0}}{Y^{R_0} - Y_0^{R_0}} \quad (3.3)$$

Note that in calculating the average values for the actuator of the radial and axial stretch, only



the middle two-thirds of the actuator were considered, in order to minimize boundary effects (see Figures 3.6 and 3.7).

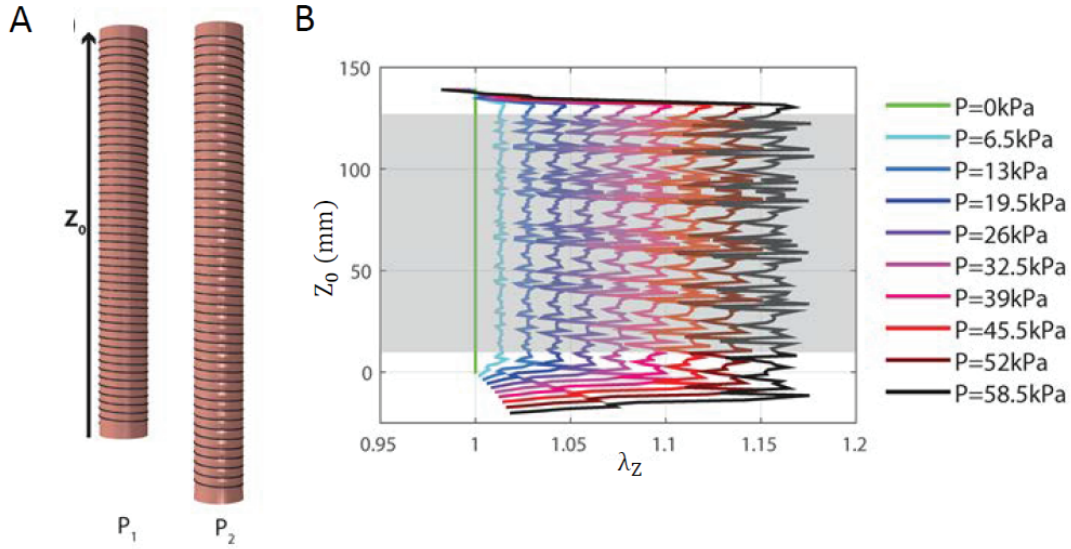


Figure 3.6: FEM simulations: Measuring change in length ( $\lambda_z$ ) (A) Snapshots of the actuator at  $P_1 = 0\text{kPa}$  and  $P_2 = 62\text{kPa}$ . (B) Axial stretch of the actuator at each pressure increment, plotted as a function of the longitudinal coordinate  $Z_0$ . Only the results shaded in grey were used to calculate the average values of the length, in order to minimize boundary effects.

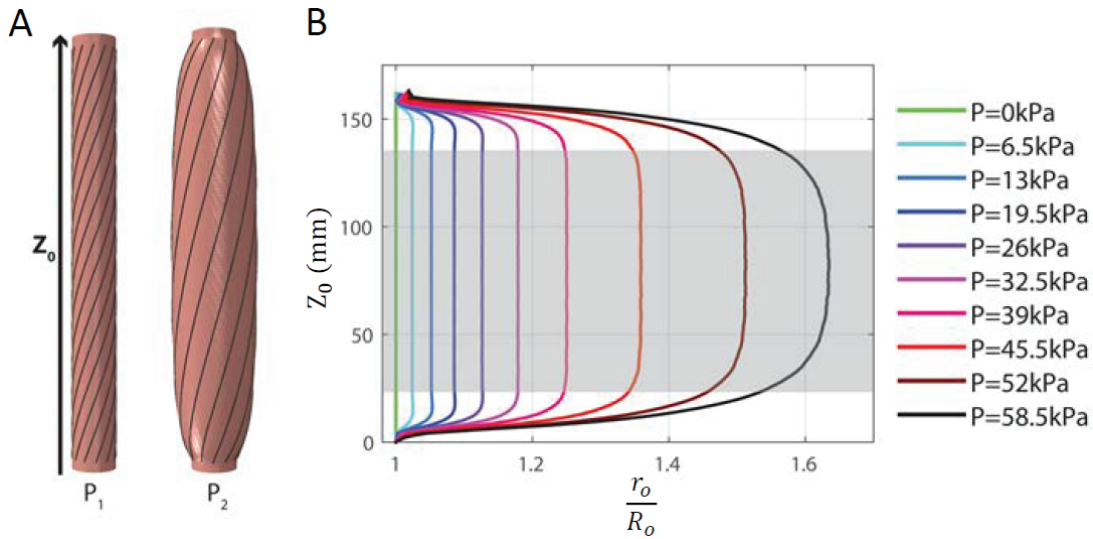


Figure 3.7: FEM simulations: Measuring change in radius ( $b/B$ ) (A) Snapshots of the actuator at  $P_1 = 0\text{kPa}$  and  $P_2 = 62\text{kPa}$ . (B) Radial stretch of the actuator at each pressure increment, plotted as a function of the longitudinal coordinate  $Z_0$ . Only the results shaded in grey were used to calculate the average values of the radius, in order to minimize boundary effects.



### 3.4.3 Experimental characterization

To characterize the deformation of the actuators, each actuator was pressurized to  $62.05\text{kPa}$ , in increments of  $6.89\text{kPa}$ , and the deformation was measured at each increment. Each actuator was pressurized and depressurized three times, and the results were averaged. To measure the extension and expansion of the actuator, a photograph was taken at each pressure increment with a Canon EOS Rebel T2i camera. Sample photographs are shown in Figures 3.8A and 3.9A.

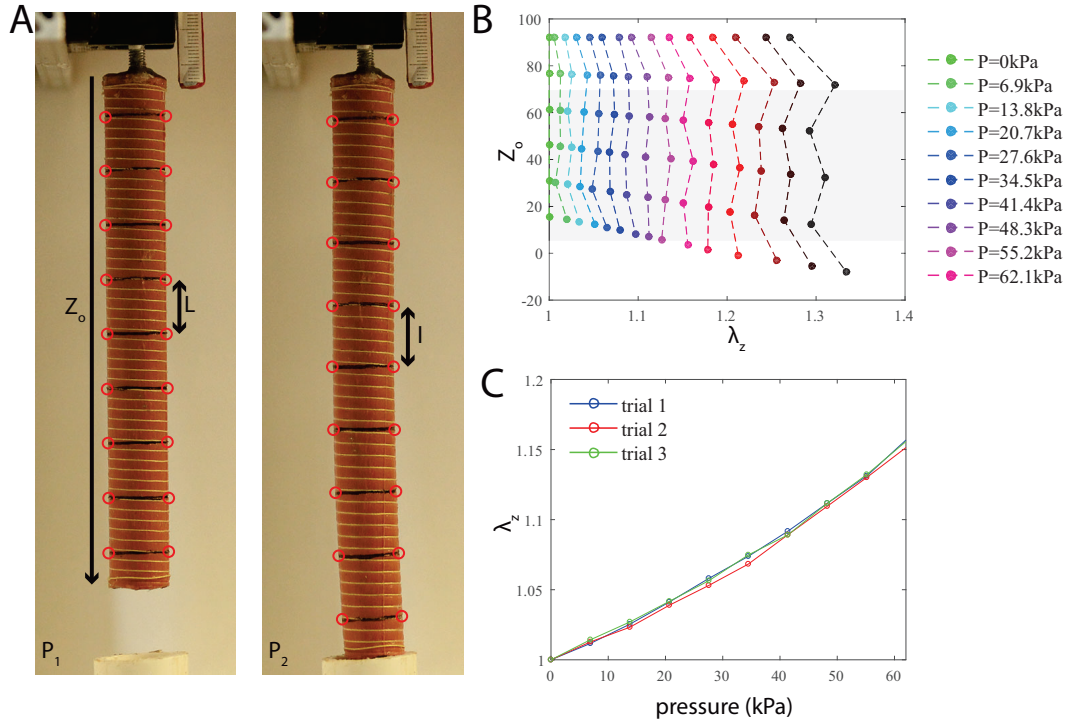


Figure 3.8: Experiments: measuring the change in length ( $\lambda_z$ ) of an actuator with fiber angle  $\alpha = -3^\circ$ . (A) Photographs of the actuator at  $P_1 = 0\text{kPa}$  and  $P_2 = 62.05\text{kPa}$ . An alignment feature (which did not interfere with the motion under investigation) was used at the bottom of the actuator. (B) Axial stretch of the actuator at each pressure increment, plotted as a function of the longitudinal coordinate. Only the results shaded in grey were used to calculate the average values of the length, in order to minimize boundary effects. (C) Average value of the axial stretch, plotted as a function of pressure

Black lines were marked on the actuator, and the coordinates of the edges of these lines were tracked using Matlab. The coordinates of the markers were used to calculate the radius and length at points along the actuator (using Equations 3.1 and 3.2) as shown in Figures 3.8B and 3.9B. The results were averaged to get the mean expansion and extension, as shown in Figures 3.8C and

3.9C. Results for the lines near the ends of the actuator were not included, in order to minimize boundary effects.

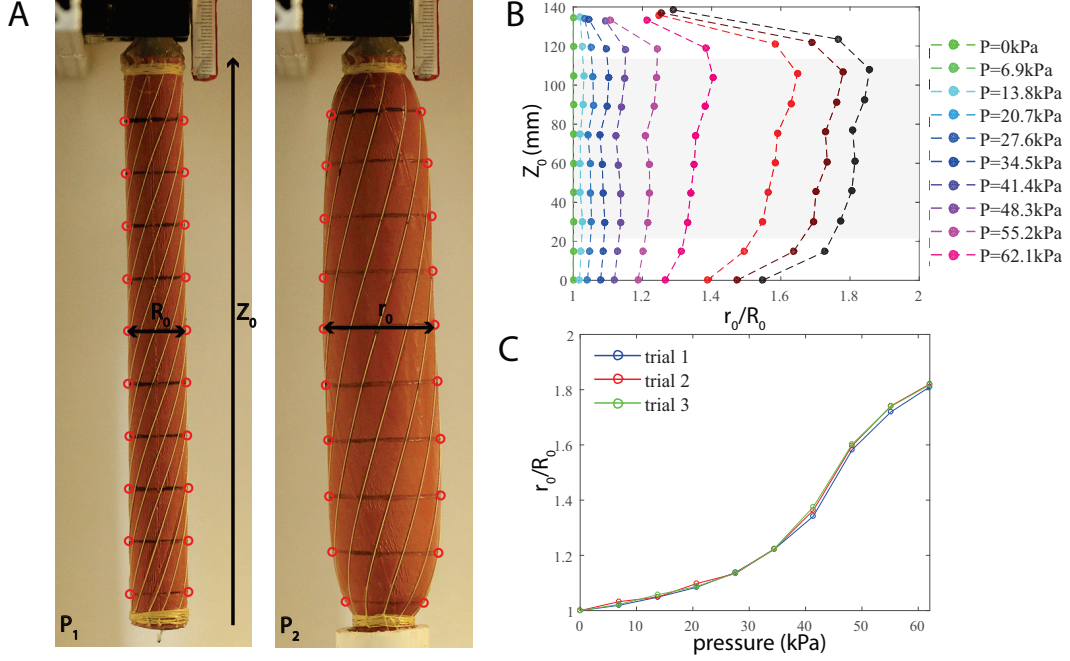


Figure 3.9: Experiments: Measuring the change in outer radius ( $b/B$ ) of an actuator with fiber angle  $\alpha = 70^\circ$ . (A) Photographs of the actuator at  $P_1 = 0 \text{ kPa}$  and  $P_2 = 62.05 \text{ kPa}$ . An alignment feature (which did not interfere with the motion under investigation) was used at the bottom of the actuator. (B) Radial stretch of the actuator at each pressure increment, plotted as a function of the longitudinal coordinate. Only the results shaded in grey were used to calculate the average values of the radius, in order to minimize boundary effects. (C) Average value of the radial stretch, plotted as a function of pressure.

To measure the twist, the camera was placed underneath the actuator. Lines were marked on the bottom of the actuator, and again, the actuator was pressurized in increments of  $6.89 \text{ kPa}$ , and a photograph was taken at each increment, as shown in Figure 3.10A. The twist was calculated by using a Matlab script to track the position of four points on the circumference of the actuator. The twist was calculated for each of these points and the results were averaged. The results are shown in Figure 3.10B and C. The twist was normalized by calculating twist per unit length, defined as

$$\tau = \frac{\theta}{\lambda_z L}.$$

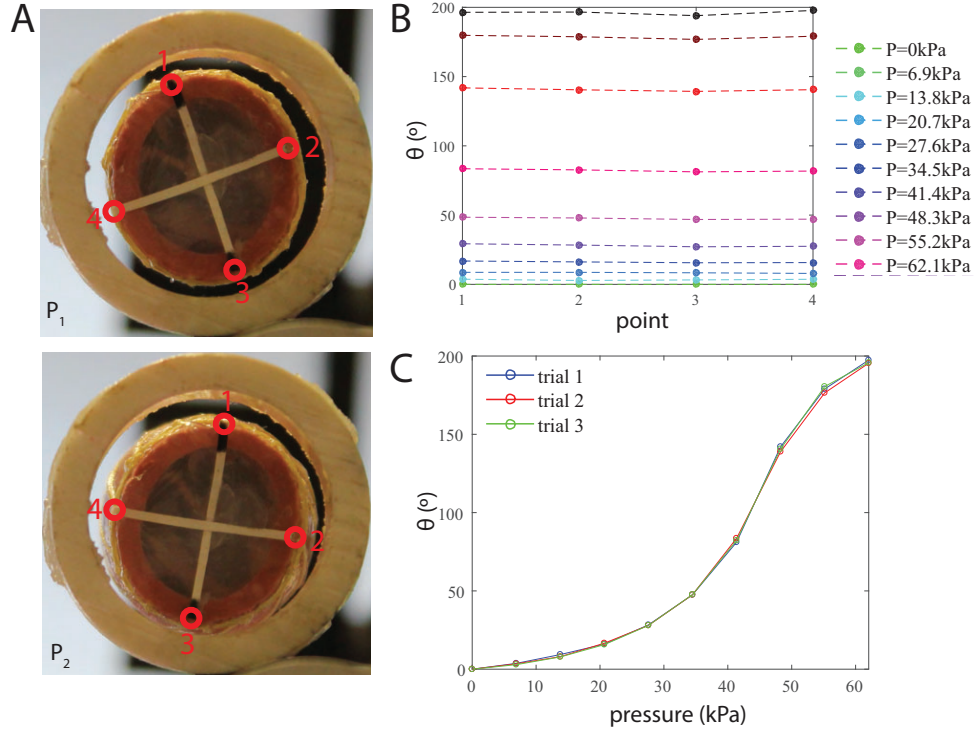


Figure 3.10: Experiments: Measuring the twist ( $\tau$ ) of an actuator with fiber angle  $\alpha = 70^\circ$ . (A) Photographs of the actuator at  $P_1 = 0 \text{ kPa}$  and  $P_2 = 27.58 \text{ kPa}$ . (B) Amount of twist at each point on the circumference of the actuator at different levels of applied pressure. (C) Average value of the twist, plotted as a function of pressure.

### 3.5 Conclusions

We have developed and experimentally validated a finite element model to predict the response to pressurization of fluidic-powered fiber-reinforced soft actuators. In particular we have shown in a quantitative manner how we can vary the fiber angle to tune the actuator response to achieve a wide range of motions as a function of input pressure. These tools can be used to guide the design of soft actuators by enabling rapid iteration of different concepts in simulation. Future challenges in this area will include optimization of the simulations to reduce computation time while still maintaining accuracy, inclusion of dynamic effects in the simulations, refinement of the fabrication procedure, and the development of analytical models for use in real-time controllers.

## 4 Automatic Design of Fiber-Reinforced Soft Actuators for Trajectory Matching

F. Connolly, C. J. Walsh and K. Bertoldi, PNAS, 114(1), 51-56, 2017

### 4.1 Introduction

In the field of robotics, it is essential to understand how to design a robot such that it can perform a particular motion for a target application. For example, this could be a robot arm that moves along a certain path or a wearable robot that assists with motion of a limb. For conventional rigid robots, methods have been developed to describe the forward kinematics (i.e. for given actuator inputs, what will the configuration of the robot be) and inverse kinematics (i.e. for a desired configuration of the robot, what should the actuator inputs be)[74, 75, 76, 77].

Recently, there has been significant progress in the field of soft robotics, with the development of many soft grippers[9, 51], locomotion robots[78, 4], and assistive devices[79]. While their inherent compliance, easy fabrication, and ability to achieve complex output motions from simple inputs have made soft robots very popular [80, 54], there is growing recognition that the development of methods for efficiently designing actuators for particular functions is essential to the advancement of the field. To this end, some research groups have begun focusing their efforts on modeling and characterizing soft actuators[34, 81, 82, 48, 28, 38, 37, 83, 84]. In particular, significant progress has been made on solving the forward kinematics problem[38, 37, 28, 83], and even on using dynamic modeling to perform motion planning[82]. However, the practical problem of designing a soft actuator to achieve a particular motion remains an issue. Finite element analysis has previously been used as a design tool to find the optimal geometric parameters for a soft pneumatic actuator, given some design criteria[48]. While this procedure yields some nice results, only basic motions (linear or bending) were studied, as the method is computationally intensive. An alternative approach is to use analytical modeling combined with optimization to determine the properties of a soft actuator that will achieve a particular motion for some target application.

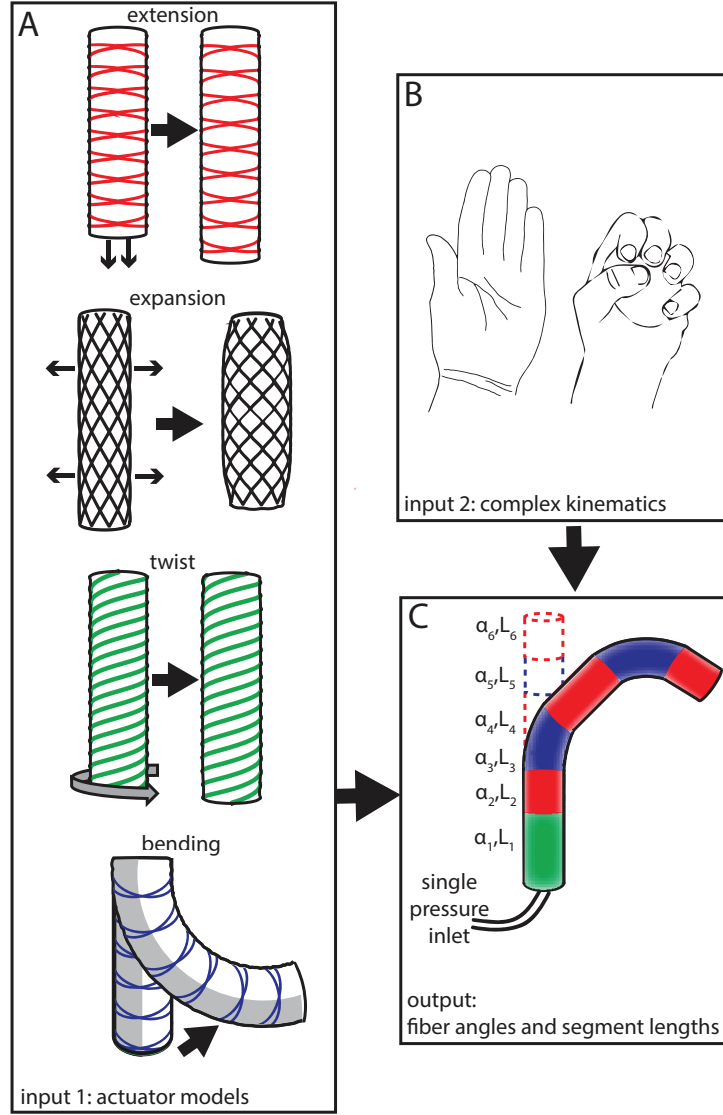


Figure 4.1: Designing an actuator that replicates a complex input motion. (A) Analytical models of actuator segments that can extend, expand, twist, or bend are the first input to the design tool. (B) The second input to the design tool is the kinematics of the desired motion. (C) The design tool outputs the optimal segment lengths and fiber angles for replicating the input motion.

Here, we focus on fiber-reinforced actuators [38, 83, 37, 84, 85], and given a particular trajectory, we find the optimal design parameters for an actuator which will replicate that trajectory upon pressurization. To achieve this goal, we first use a non-linear elasticity approach to derive analytical models which provide a relationship between the actuator design parameters (geometry and material properties) and the actuator deformation as a function of pressure for each motion type of interest (extending, expanding, twisting, and bending). Then, we use optimization to de-

termine properties for actuators which match the desired trajectory (Figure 4.1). While similar actuators were previously designed empirically[86, 56], here we propose a robust and efficient strategy to streamline the design process. Furthermore, this strategy is not limited to the specific cases presented here (namely the trajectories of the index finger and thumb), but rather could be applied to produce required trajectories in a variety of soft robotic systems, such as locomotion robots, assembly line robots, or devices for pipe inspection.

## 4.2 Analytical modeling of actuator segments

Our approach is based on assuming a desired actuator consists of multiple segments (mimicking the links and joints of the biological digit), where each different segment undergoes some combination of axial extension, radial expansion, twisting about its axis and bending upon pressurization. To realize actuators capable of replicating complex motions, we use segments consisting of a cylindrical elastomeric tube surrounded by fibers arranged in a helical pattern at a characteristic fiber angle  $\alpha$  (Figure 4.2A)[86, 36], as it has been shown that by varying the fiber angle and materials used, these can be easily tuned to achieve a wide range of motions[38, 83, 37, 84, 85]. When the elastomeric tube is of uniform stiffness, the segment undergoes some combination of axial extension, radial expansion and twisting about its axis upon pressurization [38, 37, 83]. In contrast, when the tube is composed of two elastomers of different stiffness, pressurization produces a bending motion[27, 87].

Previous work has explored the design space of fiber-reinforced actuators capable of extending, expanding and twisting using finite element analysis[84] and kinematics and kinetostatics modeling[38, 37, 83]. While these existing analytical models provide great insight into the behavior of fiber-reinforced actuators, they are restricted to exactly two sets of fibers (a set of fibers being fibers arranged at the same angle). Here we use a non-linear elasticity approach, which facilitates modeling actuators with an arbitrary number of sets of fibers. Rather than modeling the tube and the fibers individually, we treat them as a homogeneous anisotropic material [88, 89, 71]. More specifically, as the fibers are located on the outside of the tube and not dispersed throughout its thickness, we model the actuator as a hollow cylinder of isotropic incompressible hyperelastic material (corresponding to the elastomer), surrounded by a thin layer of anisotropic material (corresponding to the fiber reinforcement), and impose continuity of deformation between the two layers (Figure 4.2A). The isotropic core has initial inner radius  $R_i$  and outer radius  $R_m$ , while the outer

anisotropic layer has initial outer radius  $R_o$ . The anisotropic material has a preferred direction which is determined by the initial fiber orientation  $\mathbf{S} = (0, \cos \alpha, \sin \alpha)$ . We define a deformation gradient  $\mathbf{F}$ , from which we calculate the left Cauchy-Green deformation tensor  $\mathbf{B} = \mathbf{F}\mathbf{F}^T$ , the current fiber orientation  $\mathbf{s} = \mathbf{F}\mathbf{S}$ , and the tensor invariants  $I_1 = \text{tr}(\mathbf{B})$  and  $I_4 = \mathbf{s} \cdot \mathbf{s}$ .

The inner and outer layers require different strain energy expressions, so let  $W^{(in)}$  be the strain energy for the isotropic core, and  $W^{(out)}$  be the strain energy for the anisotropic outer layer. For the isotropic core, we choose a simple incompressible neo-Hookean model, so that  $W^{(in)} = \mu/2(I_1 - 3)$ ,  $\mu$  denoting the initial shear modulus. For the anisotropic layer, let  $W^{(out)}$  be the sum of two components,  $W^{(out)} = c_1 W^{(iso)} + c_2 W^{(aniso)}$ , where  $W^{(iso)} = \mu/2(I_1 - 3)$  is the contribution from the isotropic elastomeric matrix,  $W^{(aniso)}$  is the contribution from the fibers, and  $c_i$  are the corresponding volume fractions. To derive a suitable expression for  $W^{(aniso)}$ , we consider a small section of the helical fiber and model it as a rod subject to an axial load (Figure A.6). It is trivial to show that the strain energy density of the rod is (see Appendix A)

$$W^{(aniso)} = \frac{E(\sqrt{I_4} - 1)^2}{2}, \quad (4.1)$$

where  $E$  is its Young's modulus. By slightly modifying the strain energy, the above equations can easily be extended to account for more than one set of fibers. For example, to achieve a pure extending actuator, we might require two sets of fibers, with fiber orientations  $\mathbf{s}_1$  and  $\mathbf{s}_2$ . In this case, the strain energy density is

$$W^{(aniso)} = \frac{E(\sqrt{I_4} - 1)^2}{2} + \frac{E(\sqrt{I_6} - 1)^2}{2}, \quad (4.2)$$

where  $I_4 = \mathbf{s}_1 \cdot \mathbf{s}_1$  and  $I_6 = \mathbf{s}_2 \cdot \mathbf{s}_2$ .

We can then use the strain energies to calculate the Cauchy stresses, which take the form

$$\sigma^{(in)} = 2W_1^{(in)}\mathbf{B} - p\mathbf{I} \quad (4.3)$$

$$\sigma^{(out)} = 2W_1^{(out)}\mathbf{B} + 2W_4^{(out)}\mathbf{s}_1 \otimes \mathbf{s}_1 + 2W_6^{(out)}\mathbf{s}_2 \otimes \mathbf{s}_2 - p\mathbf{I} \quad (4.4)$$



where  $W_i = \frac{\partial W}{\partial I_i}$ ,  $\mathbf{I}$  is the identity matrix, and  $p$  is a hydrostatic pressure[90].

To further simplify the analytical modeling, we decouple bending from the other motions. In the following, we first introduce an analytical model describing an extending, expanding, twisting actuator, and then a model for a bending actuator.

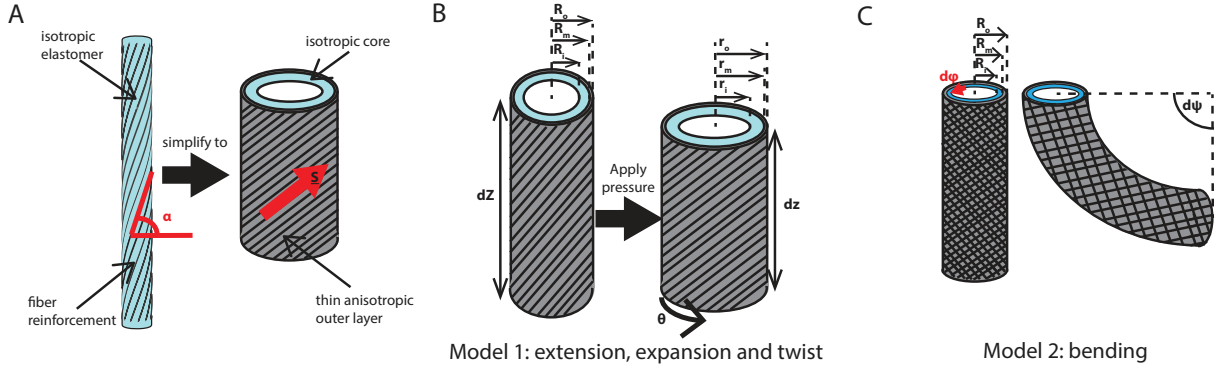


Figure 4.2: Modeling a fiber-reinforced actuator. (A) The actuator consists of an elastomeric tube surrounded by an arrangement of fibers. In the model, this system is simplified to an isotropic tube, with an outer layer of anisotropic (but homogeneous) material. (B) Parameters for the analytical model of an extending, expanding, twisting actuator. (C) Parameters for the analytical model of a bending actuator.

#### 4.2.1 Modeling extension, expansion, and twist

When the elastomeric part of the actuator is of uniform stiffness, we assume that the tube retains its cylindrical shape upon pressurization, and the radii become  $r_i$ ,  $r_m$ , and  $r_o$  in the pressurized configuration (Figure 4.2B). The possible extension, expansion, and twisting deformations are then described by (see Appendix A)

$$\mathbf{F} = \begin{pmatrix} \frac{R}{r\lambda_z} & 0 & 0 \\ 0 & \frac{r}{R} & r\tau\lambda_z \\ 0 & 0 & \lambda_z \end{pmatrix}, \quad (4.5)$$

where  $R, \Phi, Z$  and  $r, \phi, z$  are the radial, circumferential, and longitudinal coordinates in the reference and current configurations, respectively[89, 91]. Moreover,  $\lambda_z$  and  $\tau$  denote the axial stretch and the twist per unit length, respectively. To determine the current actuator configuration, we first apply the Cauchy equilibrium equations, obtaining

$$P = \int_{r_i}^{r_m} \frac{\sigma_{\phi\phi}^{(in)} - \sigma_{rr}^{(in)}}{r} dr + \int_{r_m}^{r_o} \frac{\sigma_{\phi\phi}^{(out)} - \sigma_{rr}^{(out)}}{r} dr \quad (4.6)$$



where  $P$  is the applied pressure. Assuming there are no external axial forces or external axial moments applied to the tube, the axial load,  $N$ , and axial moment,  $M$ , are given by

$$N = 2\pi \int_{r_i}^{r_m} \sigma_{zz}^{(in)} r dr + 2\pi \int_{r_m}^{r_o} \sigma_{zz}^{(out)} r dr = P\pi r_i^2 \quad (4.7)$$

and

$$M = 2\pi \int_{r_i}^{r_m} \sigma_{\phi z}^{(in)} r^2 dr + 2\pi \int_{r_m}^{r_o} \sigma_{\phi z}^{(out)} r^2 dr = 0. \quad (4.8)$$

Equations (4.6)-(4.8) with the Cauchy stress  $\sigma$  as given in Equations (4.3) and (4.4) and the deformation gradient of Equation (4.5) are then solved to find  $\lambda_z$ ,  $r_i$ , and  $\tau$  as functions of  $P$  (see Appendix A).

#### 4.2.2 Modeling bending

Since the exact solution for the finite bending of an elastic body is only possible under the assumption that the cross-sections of the cylinder remain planar upon pressurization - a condition that is severely violated by our actuator - we assume (i) that the radial expansion can be neglected (i.e.  $r/R = 1$ ) and (ii) vanishing stress in the radial direction (i.e.  $\sigma_{rr} = 0$ ). Note that these conditions are closely approximated when the actuator has fiber angle less than  $30^\circ$  and the actuator walls are thin [28]. Furthermore, since the actuators have a symmetric arrangement of fibers, no twisting takes place, so the deformation gradient reduces to (see Appendix A)

$$\mathbf{F} = \begin{pmatrix} \lambda_z(\phi)^{-1} & 0 & 0 \\ 0 & 1 & 0 \\ 0 & 0 & \lambda_z(\phi) \end{pmatrix}. \quad (4.9)$$

Since the actuator bends due to the moment created by the internal pressure acting on the actuator caps (Figure A.12), we equate this moment

$$M_{cap} = 2PR_i^2 \int_0^\pi \sin^2 \phi \text{abs}(R_i \cos \bar{\phi} - R_i \cos \phi) d\phi, \quad (4.10)$$

with the opposing moment due to the stress in the material

$$M_{mat} = \iint \lambda_z^{-1} \sigma_{zz}(R_i + \tau) (R_i \cos \bar{\phi} - (R_i + \tau) \cos \phi) d\phi d\tau, \quad (4.11)$$

where  $\bar{\phi}$  denotes the location of the neutral bending axis,  $d\tau$  is the differential wall thickness element, and  $d\phi$  is the circumferential angle element (Figure 4.2C).

Now solving  $M_{mat} = M_{cap}$  yields the relationship between input pressure and output bend angle:

$$P = \frac{\iint \lambda_z^{-1} \sigma_{zz}(R_i + \tau) (R_o \cos \bar{\phi} - (R_i + \tau) \cos \phi) d\phi d\tau}{2R_i^2 \int_0^\pi \sin^2 \phi \text{abs}(R_i \cos \bar{\phi} - R_i \cos \phi) d\phi} \quad (4.12)$$

where  $\sigma_{zz}$  can be obtained by substituting  $\mathbf{F}$  into Equations (4.3) and (4.4) (see Appendix A).

### 4.2.3 Comparing analytical and experimental results

To fabricate the extending, expanding, twisting actuators, we used the elastomer Smooth-Sil 950 (Smooth-On Inc,  $\mu_1 = 680kPa$ ), and for the bending actuators, we used both Smooth-Sil 950 and Dragon Skin 10 (Smooth-On Inc,  $\mu_2 = 85kPa$ ). The fiber reinforcement was Kevlar, with a Young's modulus  $E = 31067MPa$  and radius  $r = 0.0889mm$ . Each actuator had inner radius  $6.35mm$ , wall thickness  $2mm$  and length approximately  $160mm$ . The effective thickness of the fiber layer ( $8.89 \times 10^{-4}mm$ ) is a fitting parameter here, and was identified using the results in Figure A.8.

For the bending model, we used a Finite Element (FE) simulation (Figure A.13) to determine the location of the neutral axis ( $\bar{\phi} = 35^\circ$ ). Using FE analysis, we determined that our bending model was accurate for thin-walled actuators (Figure A.14). However, for thicker-walled actuators, the model yielded lower than expected bend angles at any given pressure. To solve this problem, we used one FE simulation (with fiber angle  $\alpha = \pm 5^\circ$ ) to determine an effective shear modulus  $\bar{\mu}$  ( $78kPa$ ) for the actuator (rather than using the experimentally measured shear moduli  $\mu_1$  and  $\mu_2$ ). We found that using this fitting parameter (from just one simulation), we could accurately predict the response for actuators with other fiber angles (see Appendix A). Note that since FE analysis generally provides more accurate results than our analytical bending model, an alternative solution would be to use FE simulations to build a database of simulation results for actuators with a range

of different fiber angles. However, this would be a more computationally expensive option, and so, while not ideal, it is preferable in our case to use just one FE simulation to identify the fitting parameters for the analytical bending model, rather than relying solely on FE.

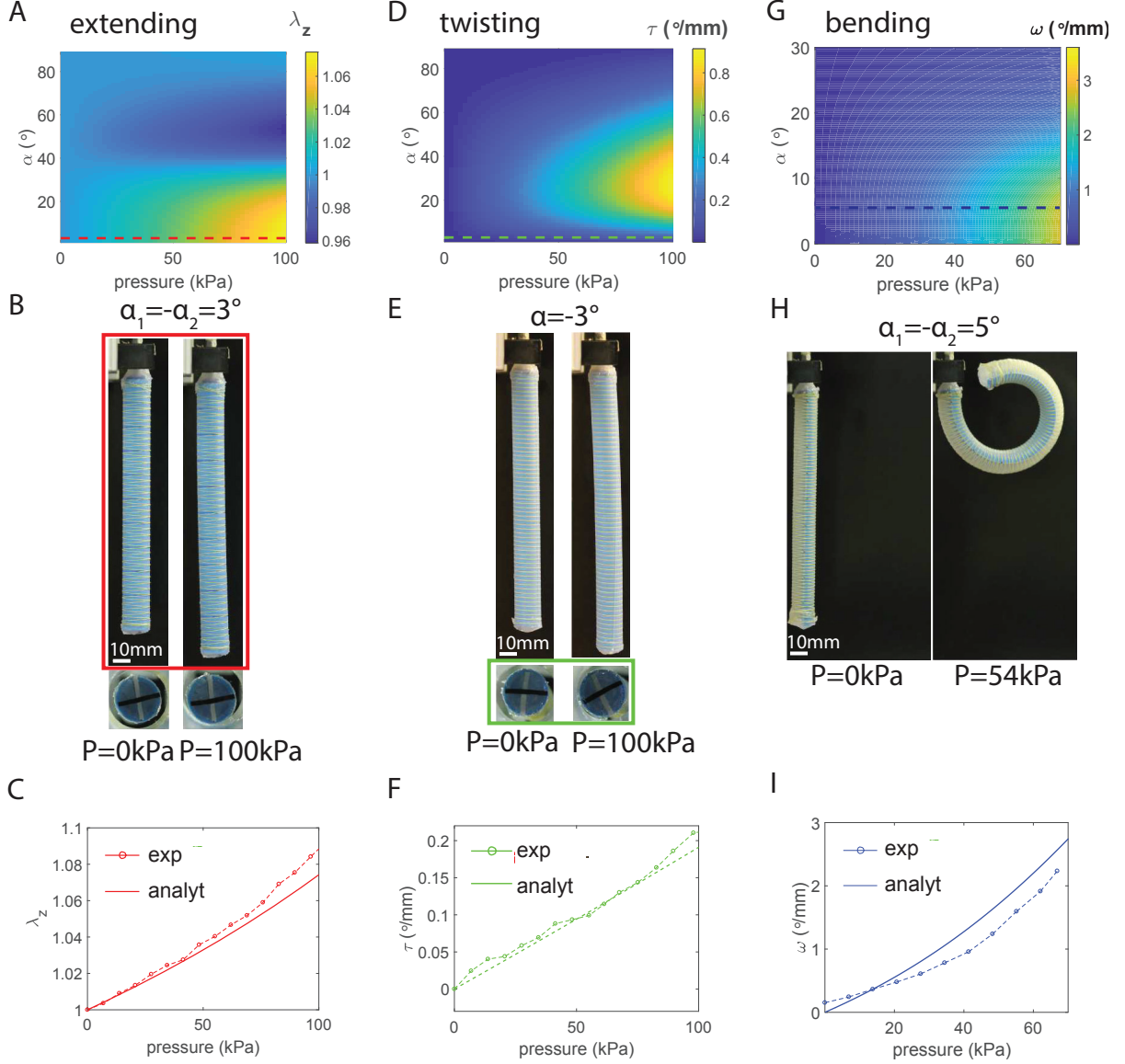


Figure 4.3: Analytical predictions and experimental results for extending, twisting, and bending actuators. (A) Heat map illustrating the axial extension ( $\lambda_z$ ) as a function of fiber angle and input pressure. (B) Front and bottom views of an extending actuator. (C) Comparison between analytical prediction and experimental results. (D) Heat map illustrating the twist per unit length ( $\tau$ ) as a function of fiber angle and input pressure. (E) Front and bottom views of a twisting actuator. (F) Comparison between analytical prediction and experimental results. (G) Heat map illustrating the bend per unit length ( $\omega$ ) as a function of fiber angle and input pressure. (H) Front view of a bending actuator. (I) Comparison between analytical prediction and experimental results.

We first consider extending actuators (with two sets of fibers, arranged symmetrically). Figure 4.3A shows how the amount of extension undergone (illustrated by the color) depends on the fiber angle of the actuator ( $y$ -axis), and the current actuation pressure ( $x$ -axis). We see that an actuator with fiber angle  $\alpha = 0^\circ$  yields the most extension, while in contrast, actuators with larger fiber angles undergo contraction. We fabricated and tested an actuator with fiber angles  $\alpha = \pm 3^\circ$  (highlighted in red in Figure 4.3A), and the results (Figure 4.3B and 4.3C) show good agreement between the model and the experiment.

Second, we consider twisting actuators, which have only one set of fibers. From Figure 4.3D, we can see that an actuator with fiber angle around  $30^\circ$  produces the maximum amount of twist per unit length. Figure 4.3E and 4.3F show that the analytical model accurately represents the twist per unit length undergone by an actuator with fiber angle  $\alpha = 3^\circ$ .

Finally, Figure 4.3G illustrates the bend angle per unit length as a function of fiber angle and actuation pressure. At any given pressure, for larger fiber angles, we see less bend per unit length. Comparing analytical and experimental results for a bending actuator with fiber angles  $\alpha = \pm 5^\circ$  (Figure 4.3H and 4.3I), we see a good match between the model and the experiment.

### 4.3 Replicating complex motions

In the preceding sections, we have presented two analytical models, which describe extending, expanding, twisting, and bending actuator motions. As well as using these models to fully explore the actuator design space, we can use them for more complex operations, such as designing a single-input, multi-segment customized actuator which follows a specific trajectory. In the following sections, we will demonstrate this methodology by determining the properties of multi-segment actuators that can replicate the motion of a finger and a thumb.

The target motion of the actuator was determined using electromagnetic trackers that were placed on the hand at the wrist, at each joint along the finger, and at the fingertip (a total of five sensors for the index finger and four for the thumb - Figure A.16)[56]. Time series data of the coordinates of each sensor in three dimensional space was recorded as the hand was opened and closed. Using this data, the configuration of the fingers and thumb during a grasping motion can be obtained. Adjacent sensors are connected by links, and we use the data to calculate the length of each link and the angles between the links at each time. Since the data is quite noisy, we

smooth it by applying a Savitzky-Golay filter. Furthermore, it will not be possible to produce an actuator which will match the finger trajectory exactly at every point, so instead we choose four configurations to match (these configurations are equally spaced along the trajectory - Figure A.17, A.18). Since the input data represents the motion of the *top* of the finger, the *top* of the actuator we design should mimic the input motion. (Alternatively, we could design an actuator which fits on top of the finger, for use in an assistive glove, for example. In this case, the *bottom* of the actuator would mimic the input motion. This is explored in Appendix A.)

The actuator will consist of multiple segments, each with a different length and fiber angle. We prescribe the number of segments, and the type of each segment (for replicating finger and thumb motion, expanding segments are not required, so each segment type is extend, bend, or twist). The radius, wall thickness, and material parameters are the same as in the previous section. Here, we use Dragon Skin 10 for the extending and twisting segments, and both Dragon Skin 10 and Smooth-Sil 950 for the bending segments. We set the maximum allowed pressure to  $80kPa$  (at higher pressures, the Matlab solver `fsolve` is unable to solve equations 4.6-4.8). Furthermore, to simplify the fabrication procedure, we impose a minimum fiber angle of  $5^\circ$ . Also, we prescribe a maximum allowed fiber angle of  $50^\circ$ , because above this angle, the radial expansion of the actuators becomes significant [84]. Note that for a finger, bending occurs at discrete joints, but for the actuator it will of course take place over some finite length. To approximate the motion of the finger as closely as possible, we want this length to be as short as possible, so we impose a maximum allowed bending segment length of  $30mm$  (see Appendix A). We then input all of this information, together with the models we developed in the previous sections, into a nonlinear least squares optimization algorithm in Matlab (`lsqnonlin`) (Figure 4.4). To find the design parameters for an actuator which will move through the given configurations (combinations of link lengths and bend angles) as it is pressurized, we minimize

$$\begin{aligned}
f = & c_1 \sum_{j=1}^N \sum_{i=1}^{n_{tw}} \left| \theta_i^{(j)} - \hat{\theta}_i^{(j)} \right|^2 + \sum_{j=1}^N \sum_{i=1}^{n_{ext}} \left| l_{ext,i}^{(j)} - \hat{l}_{ext,i}^{(j)} \right|^2 \\
& + c_2 \sum_{j=1}^N \sum_{i=1}^{n_{bend}} \left| P_i^{(j)} - \hat{P}^{(j)} \right|^2,
\end{aligned} \tag{4.13}$$

where  $n_{tw}$ ,  $n_{ext}$ , and  $n_{bend}$  are the total numbers of twisting, extending, and bending segments, respectively, and  $N$  is the number of goal configurations. The first term measures the difference between the required ( $\hat{\theta}$ ) and achieved ( $\theta$ ) twist angles, the second term the difference between the required ( $\hat{l}_{ext}$ ) and achieved ( $l_{ext}$ ) segment lengths, and the third term the difference between the pressures at which the required bend angles should be achieved ( $\hat{P}$ ), and the pressures at which the required bend angles are actually achieved with the current set of variables ( $P$ ). The parameters  $c_1 = 100$  and  $c_2 = 1000$  are weights, which balance the relative importance of the twisting, bending, and extending segments. If  $f$  is not sufficiently small, the variables are updated and the optimization loop repeats. When the minimum value of  $f$  is found, the optimization outputs (1) the fiber angle  $\alpha_i$  for each segment (2) the initial length of each of the bending and twisting segments and (3) the pressures  $\hat{P}^{(j)}$  at which the goal configurations will occur.

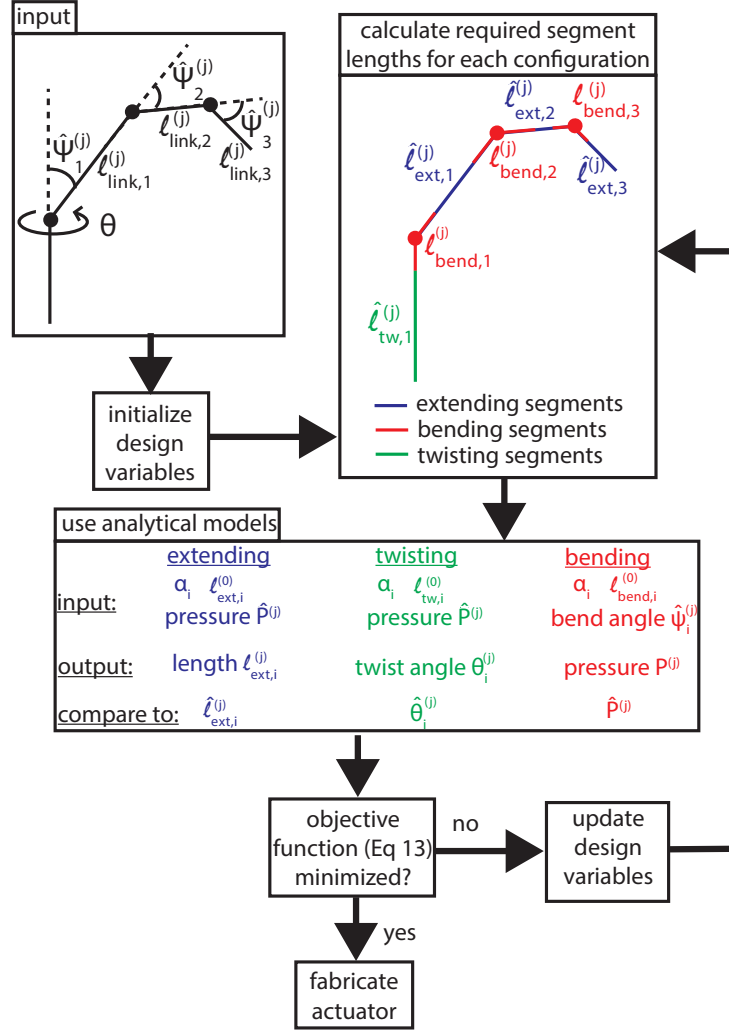


Figure 4.4: Optimization algorithm for actuator design

#### 4.3.1 Index finger motion

The fiber angles and lengths required to imitate the movement of the index finger are illustrated in Figure 4.5D. Segments 1, 3, and 6 are extending actuator segments of length  $70mm$ ,  $22mm$ , and  $15mm$ , with fiber angles of  $\pm 40^\circ$ ,  $\pm 50^\circ$ , and  $\pm 50^\circ$ , respectively. These segments undergo axial contraction when pressurized. Segments 2, 4 and 5 are bending segments of length  $22mm$ ,  $28mm$  and  $15mm$ , with fiber angles of  $\pm 6^\circ$ ,  $\pm 5^\circ$  and  $\pm 5^\circ$ , respectively.

We fabricate the actuator as detailed in Appendix A. To compare the actual performance of the actuator to the expected performance, we characterize it by taking pictures of the actuator at various different actuation pressures. We evaluate its motion by using Matlab to track points on

the actuator. We see good agreement between expected and actual motion (Figure 4.5C,E), with some discrepancies, which are most likely due to defects in the actuator fabrication (for example, segment lengths being up to 4mm shorter than expected, due to the fibers being wound around the actuator between segments-see Appendix A).

#### 4.3.2 Thumb motion

As a second example, we consider the design of an actuator which upon pressurization replicates the motion of a thumb. The motion of the thumb is more complex than that of the finger, since it moves out of plane. We capture this out of plane motion as a twisting motion. We calculate the amount of twist by fitting a plane to the twisting links at each time, and then finding the angle between the normal to this plane and the normal to the initial plane.

Figure 4.5I illustrates the fiber angles which are needed to reproduce the motion of the thumb, as predicted by the model. Segment 1 is a twisting segment of length 25mm, with fiber angle  $5^\circ$ , segments 2, 4, and 6 are bending segments of length 15mm, 30mm and 22mm, each with fiber angles  $\pm 5^\circ$ , and segments 3, 5, and 7 are extending segments of length 20mm, 8mm, and 17mm, with fiber angles  $\pm 41^\circ$ ,  $\pm 50^\circ$ , and  $\pm 47^\circ$ . To analyze the motion of this actuator, we placed two cameras at right angles to each other and took pictures of the actuator at various different actuation pressures. The images were combined to reproduce the three dimensional motion of the actuator (see Appendix A). Figure 4.5H,J compares the input thumb kinematics and the output actuator motion. We see reasonable agreement between the expected and achieved motions, with discrepancies in this case most likely due to inaccuracies in measuring the actuator motion (for example, misalignment of cameras), as well as defects in actuator fabrication (such as non-uniform wall thickness).



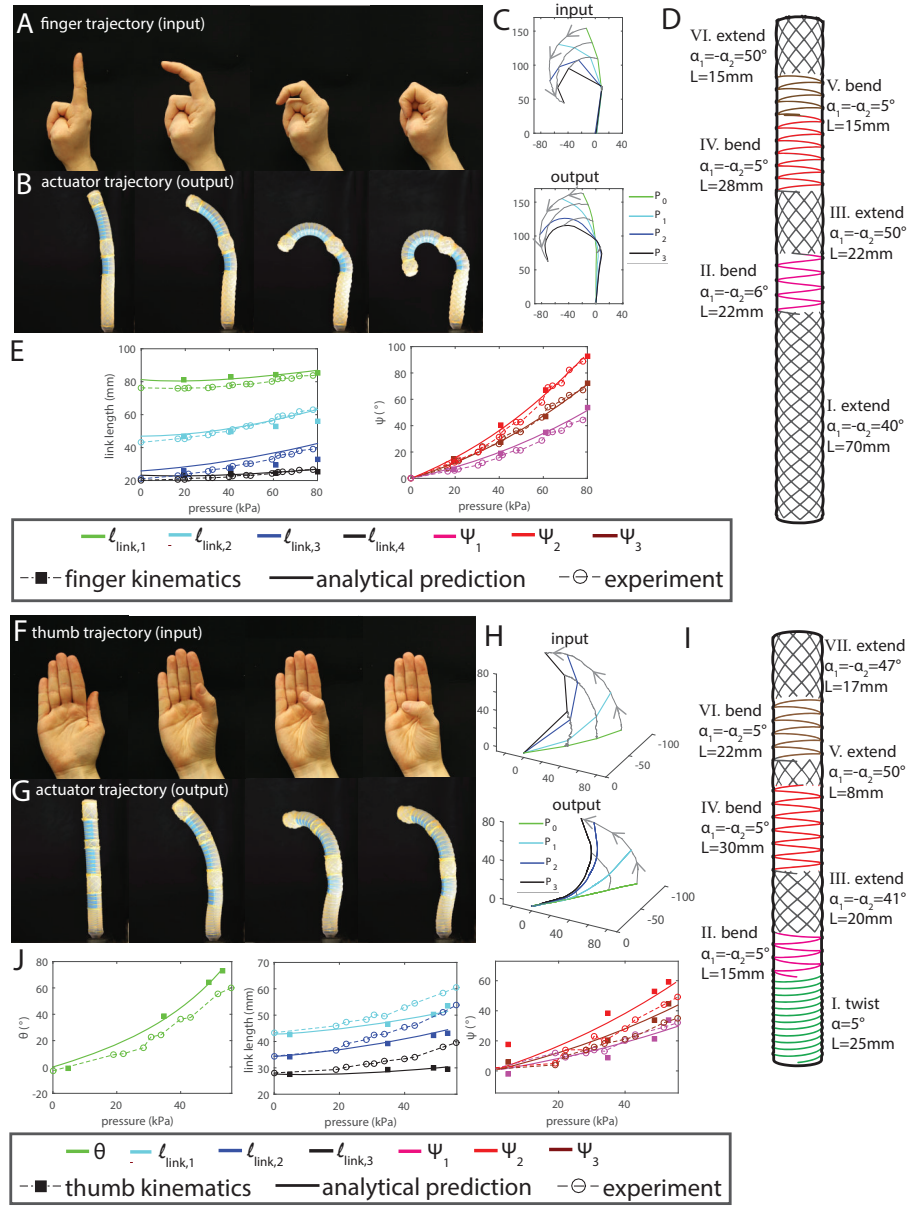


Figure 4.5: (A and B) Finger actuator: qualitative comparison of actuator motion and finger motion. (C) Comparison of input finger trajectory and output actuator trajectory. (D) Illustration of segment lengths and fiber angles. (E) Quantitative comparison of desired, expected, and achieved link lengths (left) and bend angles (right). (F and G) Thumb actuator: qualitative comparison of actuator motion and thumb motion. (H) Comparison of input thumb trajectory and output actuator trajectory. (I) Illustration of segment lengths and fiber angles. (J) Quantitative comparison of desired, expected, and achieved twist angles (left), link lengths (center), and bend angles (right).

## 4.4 Conclusions

Using analytical models for fiber-reinforced actuators which extend, expand, twist, and bend, we have devised a method of designing actuators customized for a particular function. Given the kinematics of the required motion, and the number and type of segments required, the algorithm outputs the appropriate length and fiber angle of each segment, thereby providing a recipe for how the actuator should be made. The procedure is somewhat limited in its current form as it requires the user to input the type of segments required, but future versions will eliminate the need for this, thus further automating the procedure. Future work will also focus on developing a model which combines bending with other motions, to increase the versatility of the algorithm. The design tool we have presented here has immense potential to streamline and accelerate the design of soft actuators for a particular task, eliminating much of the trial and error procedure which is currently used, and broadening the scope of fiber-reinforced soft actuators.

## 5 Sew-free Anisotropic Textile Composites for Rapid Design and Manufacturing of Soft Wearable Robots

F. Connolly, D. A. Wagner, C. J. Walsh, and K. Bertoldi

### 5.1 Introduction

Inflatable actuators made of compliant elastomeric materials have attracted growing interest in recent years[3, 80, 54] and enabled the design of soft wearable robots and assistive devices that can safely and effectively interact closely with humans.[92, 93, 28] However, one drawback of using elastomers is that their response is intrinsically isotropic. As such, to achieve the level of anisotropy required to realize actuators capable of the desired motions, either complex architecture[94, 45, 49] or carefully oriented fibers[27, 85] are embedded into the actuators, adding complexity to the system. Furthermore, while elastomeric soft actuators are very compliant, they can be too heavy and bulky for wearable robots and overly restrict the movement of joints even when the device is unpowered.

Textiles are promising materials to realize the next generation of soft wearable robots, as they are lightweight, conformable, stretchable, and intrinsically anisotropic. Because of their lightness, compliance, and low packing volume, textiles have already been utilized in a variety of inflatable structures, including airbags for car safety,[95] temporary shelters,[96, 97] and actuators which provide linear and rotary motions.[25, 44] However, these structures do not take advantage of the stretchability and anisotropy of the textiles and their inflated configuration is completely determined by their initial shape. Only very recently it has been shown that the intrinsic anisotropy and stretchability of textiles can be exploited to create bending actuators with very simple geometry.[98] This effort, however, represents only the first step towards textile-based wearable soft robots. The fabrication of the actuators via a cutting and sewing process not only is labor-intensive and time-consuming, but also introduces weak points into the textile where failure is more likely to occur during inflation. Moreover, since actuation is achieved by inflating a thermoplastic elastomer balloon inside the textile pocket, the response is often not repeatable due to inconsistencies in balloon insertion and movement of the balloon inside the pocket. In order to realistically bring the great potential of textiles to wearable soft robots, there is the need not only to identify new

approaches for quickly manufacturing actuators that perform reliably and repeatably, but also to develop mathematical models to guide their design.

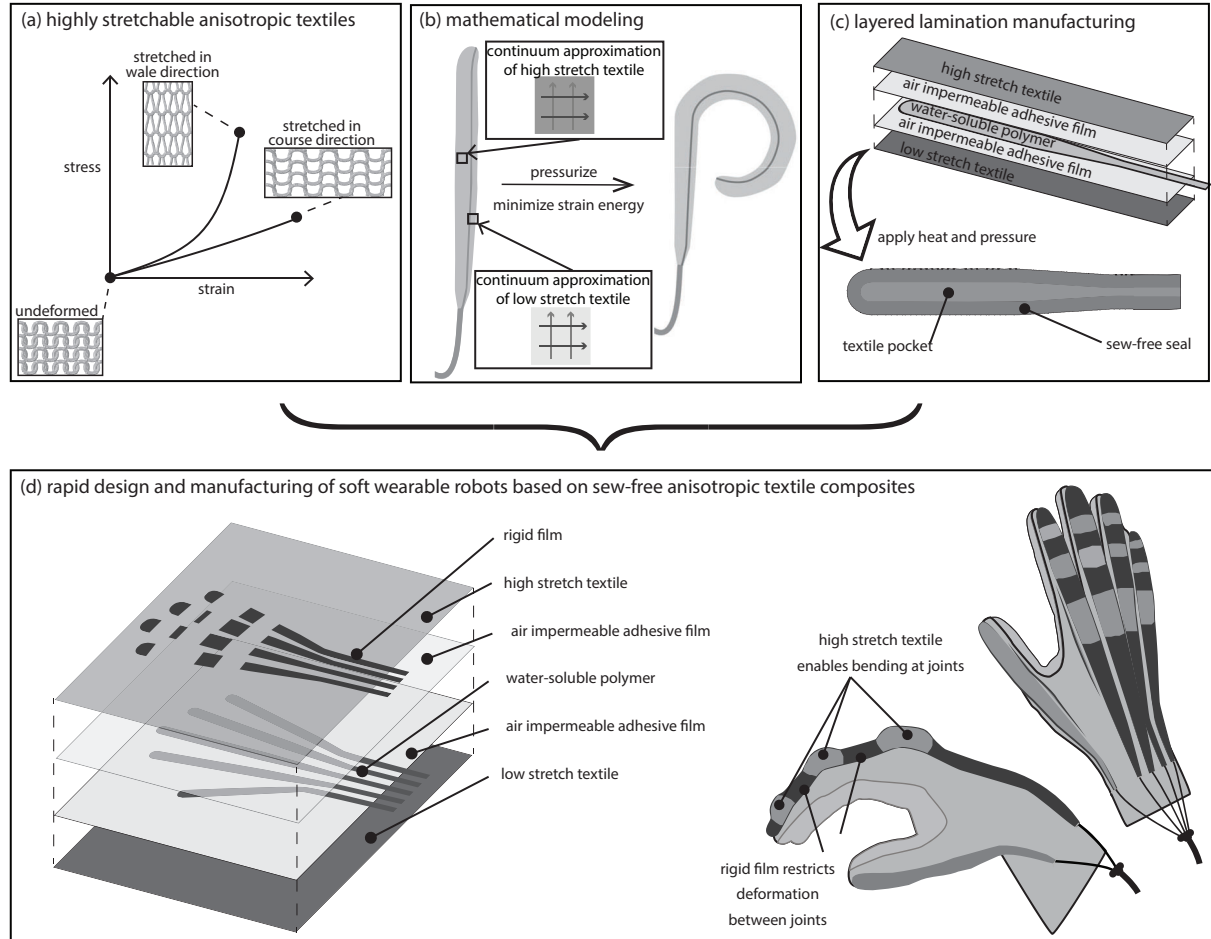


Figure 5.1: (a) Knitted textiles show highly anisotropic behavior under uniaxial tension. (b) By modeling textiles as homogeneous anisotropic continua, we can develop models of bending textile actuators. (c) Using lamination and layering, we can fabricate actuators quickly and easily. (d) Manufacturing and modeling approaches can easily be scaled to more complex designs.

Here, we combine experimental and analytical tools to realize textile-based actuators that can be integrated into a glove to assist impaired individuals in performing activities of daily living.[56, 99] Our bending actuators fully exploit the anisotropic properties of highly stretchable textiles (Figure 5.1a) and are rapidly designed by employing a mathematical model that enables us to identify the geometric parameters resulting in the desired motion (Figure 5.1b). Moreover, a new manufacturing approach, which involves laminating the textiles and using heat to bond them enables the rapid fabrication of different actuator designs (Figure 5.1c). With these new manufacturing and modeling

approaches, we design actuators with articulation which imitate the motion of a finger and can be integrated into an assistive glove (Figure 5.1d). Notably, our manufacturing and modeling strategies are not limited to the specific cases presented here, but could be applied to a range of assistive and wearable robots for both upper and lower extremities.

## 5.2 Textile selection and modeling

We start by noting that to produce the required bending motion while keeping the actuator as low-profile as possible, the top part of the actuator calls for a textile which stretches a lot in one direction and stretches minimally in the perpendicular direction, while for the bottom part we need a textile which stretches less in all directions. We also note that while the bottom textile should not stretch very much, it should still have some extensibility - this allows us to incorporate the actuator into wearable devices, which can stretch as a person moves. Furthermore, to enable pneumatic actuation we need to make the textiles impermeable to air. This can be achieved by coating the textiles with a thermoplastic polyurethane film (3918, Bemis Company, Inc.), which not only makes the textiles air impermeable, but also preserves their anisotropic properties and does not overly inhibit their extensibility (see Figure B.1).

Next, we use mechanical testing to identify commercially available textiles with the ideal mechanical properties. More specifically, we conduct uniaxial and equibiaxial tension tests on different textile-film composites. We find that a Raschel knit (24710, Darlington Fabrics) is particularly suited for the top part of the actuator, as its knit structure allows it to undergo high stretch in its wale direction, while restricting the stretch in the course direction (see Figure 5.2C). For the bottom, we choose a Tricot knit (26210, Darlington Fabrics), as it is significantly stiffer than the Raschel knit in both the course and wale directions (see Figure 5.2d). Finally, it is important to note that the mechanical response of the selected textiles can be nicely captured using a hyper-elastic anisotropic continuum model such as the Holzapfel-Gasser-Ogden model,[65] whose strain energy is given by

$$W = C(I_1 - 3) + \frac{k_1}{2k_2} \left( e^{k_2(I_4 - 1)^2} - 1 \right). \quad (5.1)$$

In the equation above,  $C, k_1, k_2$  are material parameters,  $I_1 = \text{tr}(\mathbf{F}\mathbf{F}^T)$  and  $I_4 = \mathbf{F}\mathbf{M} \cdot \mathbf{F}\mathbf{M}$ ,  $\mathbf{F}$  being the deformation gradient and  $\mathbf{M}$  denoting the stiffest direction of the textile in the undeformed

configuration. We find that the response of the top layer is best captured using  $C = 0.64$  MPa,  $k_1 = 0.12$  MPa and  $k_2 = 0.52$  (see Figure 2c), while for the bottom layer  $C = 0.99$  MPa,  $k_1 = 0.017$  MPa and  $k_2 = 1.1$  lead to the best match (see Figure 2d).

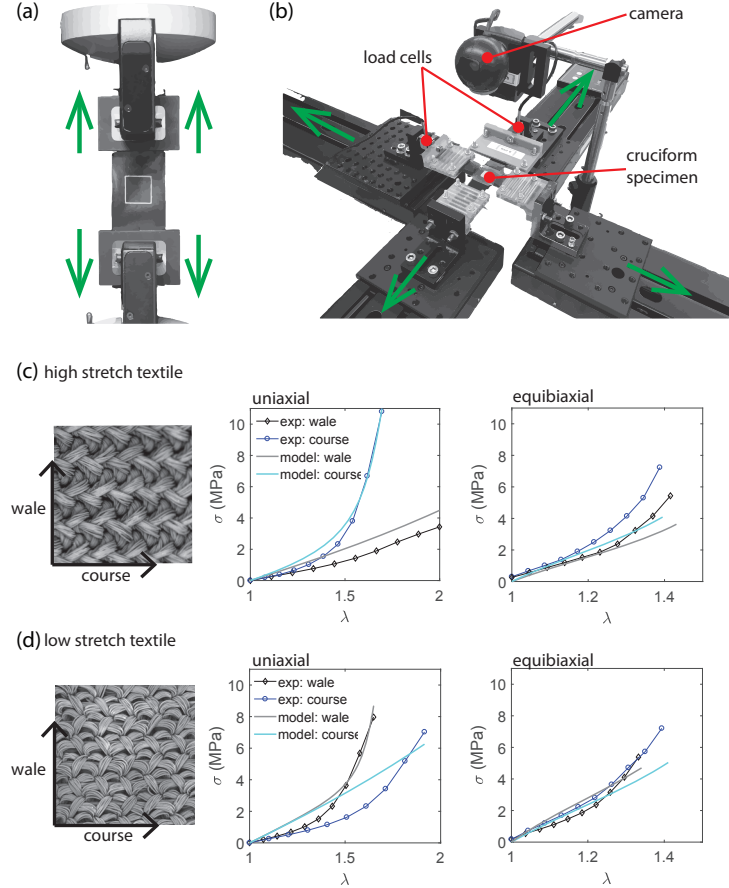


Figure 5.2: (a) Uniaxial tensile test setup (b) Biaxial tensile test setup (c) SEM image, experimental data, and best-fit model for high-stretch textile (d) SEM image, experimental data, and best-fit model for low-stretch textile

### 5.3 Actuator fabrication

Having identified two textile-film composites with ideal mechanical properties, we now combine them to make inflatable actuators. To this end, we take advantage of the fact that the film which we applied to the textiles to make them air-impermeable can bond to itself and use a heat press (Digital Knight DK20S) to put the two composite layers together, eliminating the need to sew a complex seam. To form an airtight textile pocket, we place between the two layers a water-soluble polymer (Sulky Ultra Solvy Stabilizer, a polyvinyl alcohol) which has been cut (using a Versa laser)

into the shape of the desired actuator chamber. The polymer does not adhere to the film during heating and, when the bonding process is complete, can simply be dissolved using water. The actuator is finished by inserting a tube and gluing it in place (see Appendix B for more details).

We start by fabricating bending actuators with a rectangular chamber of width  $W$  and length  $L$  (the chamber also has an additional taper towards the tubing and is rounded at the distal end - see Figure 5.3a). The actuators are initially flat (Figure 5.3a) and take on a cylindrical shape (with radius  $R_i = W/\pi$ ) as the inflation starts (i.e. for very small values of applied pressure - Figure 5.3b). However, as the pressure increases, the textiles get stretched and the actuators start to bend, taking on the shape of a toroidal segment (Figure 5.3c). To quantify the deformation of our actuators during inflation, we use a camera (Canon EOS Rebel T5i) and extract their outer edge (in the region of the chamber of initial length  $L$ ) from the recorded images via edge detection. By finding the circular arc which best fits this edge of length  $l_t$ , we can identify the radius of curvature of the actuator  $\rho$  and the bend angle  $\psi = l_t/\rho$ . Moreover, by tracking the white lines located at the two ends of the chamber (indicated by the red boxes in Figure 5.3d) via digital image processing we can monitor the radius of the actuator  $r_i$  (see Appendix B).

In Figure 5.3e we report the evolution of the bend angle per unit length ( $\psi/L$ ) and of the change in radius ( $r_i/R_i$ ) as a function of the applied pressure for three actuators all with length  $L = 110$  mm and width  $W = 10$  mm (green markers), 20 mm (blue markers), and 30 mm (black markers). We see that the actuator with  $W = 10$  mm bends the most and undergoes the most circumferential stretch overall. However, it requires higher pressure to reach this level of deformation. In contrast, widths  $W = 20$  mm and 30 mm result in similar bend angles and circumferential stretches up to 100 kPa, although the 20mm actuator deforms more overall.

## 5.4 Actuator modeling

The experimental results of Figure 5.3c indicate that the response of the actuators can be tuned by varying their geometry. To rapidly navigate the design space and identify actuator geometry leading to the desired response, we develop a mathematical model based on nonlinear elasticity. Previous models of pneumatic soft actuators often relied on finite element analysis, which gives accurate results, but is time-consuming.[100, 33, 48] Analytical models were developed as an alternative, but relied on the assumption of zero deformation in the radial direction[101, 28] - this assumption

is clearly violated by our textile-based actuators, necessitating a new modeling approach.

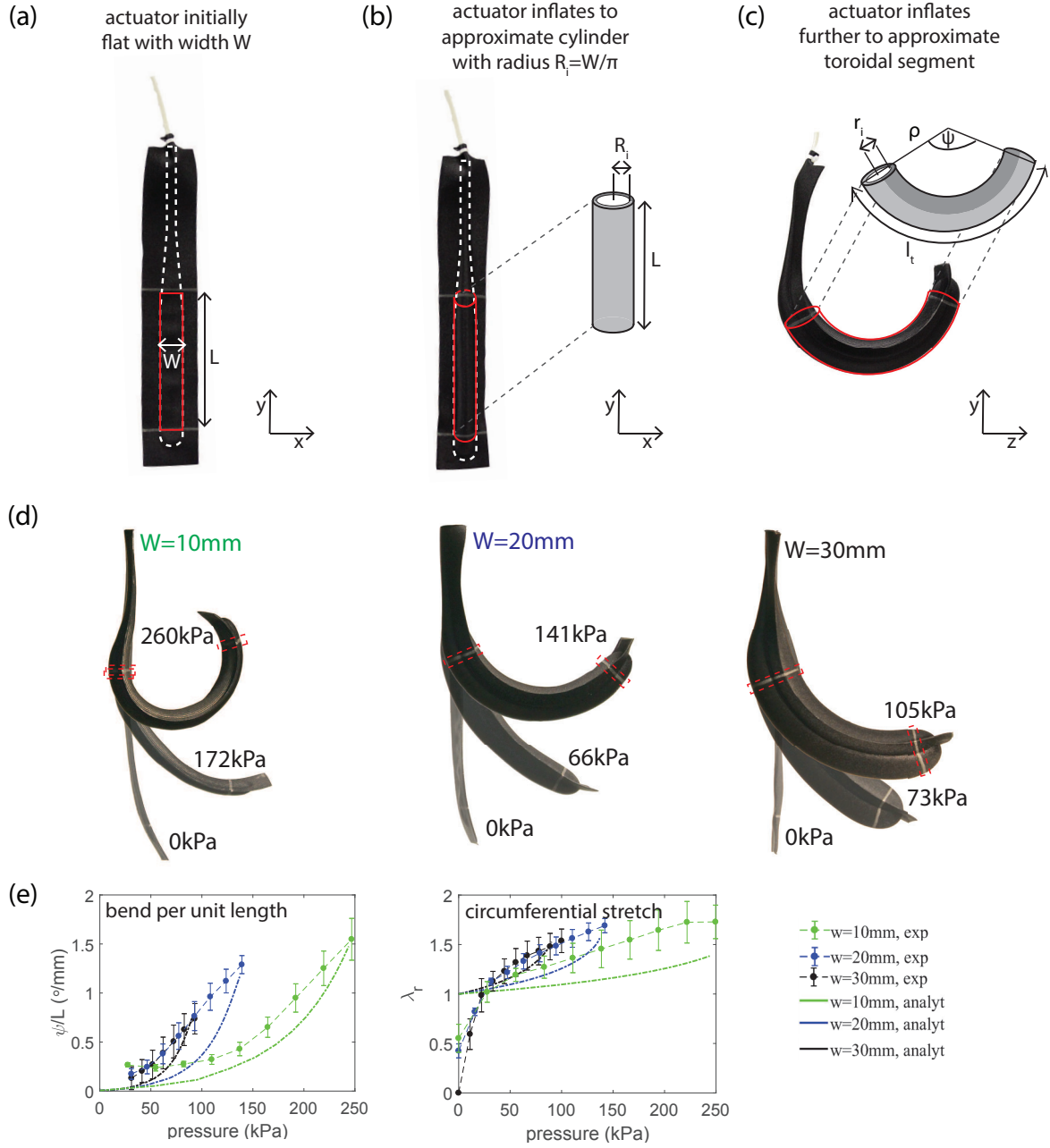


Figure 5.3: (a)-(c) Illustration of model parameters (d) Photographs of actuators with different widths at different actuation pressures. (e) Comparison of experimental results and model predictions of actuator deformation.

Taking inspiration from the volume maximization strategy recently proposed to model elastomeric fiber-reinforced actuators,[102] here we use strain energy minimization to predict the actu-



ator deformation (see Appendix B for more details). More specifically, guided by our experiments, we assume that the actuator starts from a cylindrical configuration with inner radius  $R_i = W/\pi$  and length  $L$ , and inflates to the shape of a toroidal segment with major radius  $\rho$ , minor radius  $r_i$ , and length  $l_t$  (neglecting the ends of the actuator). Since the actuator consists of two materials, which deform differently, the deformed actuator also has one more parameter  $k$ , which relates the extension in circumferential direction of the top layer to that of the bottom one. Finally, to simplify the model, we assume that all materials in the actuator are incompressible, an assumption which we validated using finite element analysis (see Appendix B). Under these assumptions, the strain energy  $U$  of the actuator can be written as:

$$U = \int_0^L \int_{-\frac{\pi}{2}}^{\frac{\pi}{2}} \int_{R_i}^{R_o} W^{(b)} R dR d\Theta dZ + \int_0^L \int_{\frac{\pi}{2}}^{\frac{3\pi}{2}} \int_{R_i}^{R_o} W^{(t)} R dR d\Theta dZ, \quad (5.2)$$

where  $W^{(b)}(\Theta)$  and  $W^{(t)}(\Theta)$  are the strain energy densities of the bottom and top textiles (given by Equation 5.1),  $R$ ,  $\Theta$  and  $Z$  are the radial, circumferential, and axial coordinates in the initial configuration,  $R_i$  and  $R_o$  are the initial inner and outer radii of the actuator, and  $L$  is the initial length of the actuator. Since the volume enclosed by a toroidal segment is

$$V = \pi r_i^2 \frac{l_t}{\rho + r_i} \rho, \quad (5.3)$$

given a supplied volume  $V_{supplied}$  inside the actuator, we then solve for  $(\rho, r_i, l_t, k)$  by minimizing the strain energy  $U$  (via the constrained nonlinear solver `fmincon` in Matlab) subject to the constraint  $V_{supplied} = V$ . Finally, we use the Cauchy equilibrium equations to relate the deformation to the internal pressure  $P$  (see Appendix B for details):

$$P = \frac{1}{2\pi} \int_{-\frac{\pi}{2}}^{\frac{\pi}{2}} \int_{r_i}^{r_o} \frac{\sigma_{\theta\theta}^{(b)}(\Theta) - \sigma_{rr}^{(b)}}{r} dr d\Theta + \frac{1}{2\pi} \int_{\frac{\pi}{2}}^{\frac{3\pi}{2}} \int_{r_i}^{r_o} \frac{\sigma_{\theta\theta}^{(t)}(\Theta) - \sigma_{rr}^{(t)}}{r} dr d\Theta, \quad (5.4)$$

where  $\sigma^{(\alpha)} = -p\mathbf{I} + \frac{1}{\det \mathbf{F}} \frac{\partial W^{(\alpha)}}{\partial \mathbf{F}} \mathbf{F}^T$  is the Cauchy stress ( $p$  is a hydrostatic stress,  $I$  is the identity matrix, and  $\alpha \in \{t, b\}$  refers to the top and bottom textiles). In Figure 5.3e, we compare the predictions of this model (continuous lines) to experimental results (markers) for the three

considered different geometries. We see a reasonably good match between model and experiment, with discrepancies most likely due to the constitutive models for the textiles not picking up all of the complexities of the textile behavior and to the assumption that the actuator cross-section is perfectly circular.

## 5.5 Application to assistive glove

Having identified tools for rapidly modeling and manufacturing textile actuators, we now demonstrate that these methods enable us to design articulated actuators for use in a glove which mimics finger motion and can be mounted on the outside of the hand to assist with grasping. To this end, we first note that the textile actuators presented in Figure 5.3 are not ideal for this application, since they have constant bending curvature, whereas fingers bend at discrete locations (i.e. at the joints). To produce actuators capable of matching the motion of the fingers, we require the portions of the actuator which will be located at the joints to bend upon inflation, while those in between should resist deformation. Notably, these alternating bending and straight segments can be realized with a single pocket (so that the actuator has only a single pressure input), by applying a stiff polyamide film (4220, Bemis Company, Inc.) to certain portions of the actuator to significantly increase its stiffness in those areas. Thus, such articulated actuators can be manufactured following the same procedure as before, simply adding an extra step where we laminate the actuators with the stiff film in certain areas (Figure 5.4b). However, identifying the actuator width and the lengths of the bending and straight segments is challenging, as there are a few requirements which must be fulfilled. More specifically, we want the actuator (i) to be as narrow as possible, to ensure it remains low-profile when inflated (but it must still be wide enough to enable easy fabrication); (ii) to achieve the target configuration at a low pressure, to ensure safe operation; (iii) to have bending segment lengths which are as short as possible (to fit over the joints). Assuming that there are no interactions between bending and straight segments, we can use our analytical model to identify actuators capable of achieving the target configuration while satisfying all these requirements. To this end, in Figure 5.4c we report the bend per unit length as a function of initial actuator width and applied pressure as predicted by our analytical model for a homogeneous bending segment. We see that at any given pressure, wider actuators yield greater bend per unit length ( $\psi/L$ ). Moreover, we find that for each actuator width, there is a critical pressure above which the model breaks

down due to a ballooning instability in the constitutive models (see white area in Figure 5.4c). Such instability clearly limits the maximum pressure at which we can operate.

To demonstrate the power of our modeling approach, we choose an everyday task – picking up a glass or bottle – and use the predictions of Figure 4c to design actuators that mimic the grasping motion used for that task. Given the average joint angles for grasping a cylindrical object of diameter 50.8 mm [103] and the average finger dimensions for a large-sized hand (see Figure 5.4a and Appendix B), we can identify the required configurations for each of the fingers (index, middle, ring, and little). Focusing on a middle finger with total length of 194 mm, we find that an actuator of width 11.5 mm with bending segments of length 27 mm, 25 mm, and 21 mm reaches the target configuration at a pressure of 240 kPa (Figure 5.4d), satisfying all of our requirements. In Figure 5.4e we show the fabricated actuator based on this design when inflated to a pressure of 240 kPa, with its target shape overlaid. We see that the actuator behaves as expected, with only a slight difference between the target configuration and the actual configuration. This difference is most likely due to the inaccuracies of the model (as outlined above) and also due to our assumption that the straight segments do not affect the deformation of the bending segments (we can see in Figure 4e that the radius of a bending segment has to decrease a lot at its edges in order to match the radius of the straight segments). However, the discrepancy between the target configuration and the actual configuration is not large enough that we would expect it to affect the functionality of the glove. The index, ring, and little finger actuators were designed similarly, and results can be seen in Appendix B.

Next, we show that the articulated actuators we have designed can be integrated into an assistive glove, using one actuator for each finger. For the index, middle, ring, and little fingers, we use the articulated actuator designs identified in the previous section. Since the thumb moves out of plane as it bends, the actuators presented here are not sufficient to replicate its motion. Our future work will investigate fabrication and modeling of sew-free actuators which both bend and twist and would be able to replicate thumb motion, but for the present work we use just a simple bending actuator in place of a thumb actuator.

To fabricate the assistive device, we use the same layered manufacturing approach as we used for the individual actuators. Since the geometry here is more complex, we use an alignment board and pins to ensure that the layers line up correctly (see Appendix B). As before, we start by laminating

both the high stretch and low stretch textiles. We then seal the laminated textiles together to create a glove-shaped device with five embedded air chambers. We add rigid film to the top and bottom of the device to create articulation for each of the fingers.

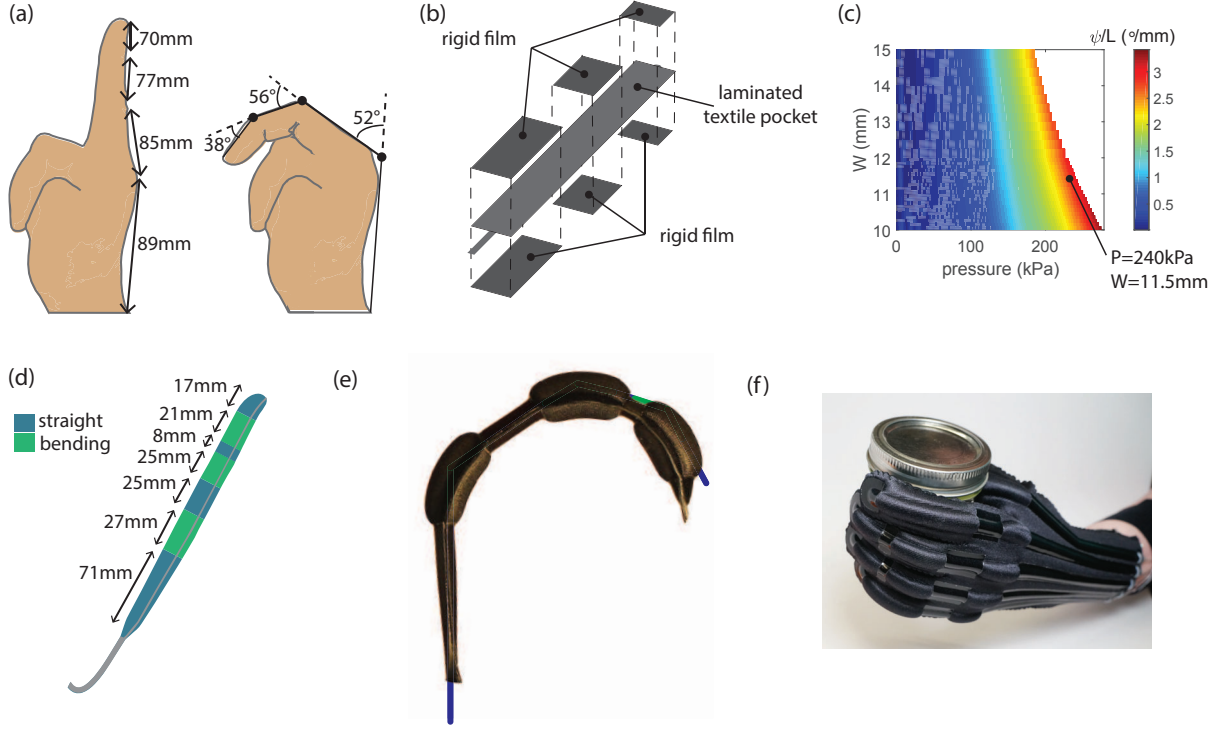


Figure 5.4: (a) Middle finger joint angles and lengths (b) Applying rigid film to the outside of the actuator yields the straight segments (c) Contour plot showing bend angle per unit length as a function of actuator width and applied pressure (d) Middle finger actuator design (e) Middle finger actuator at  $240\text{kPa}$ , overlaid with target configuration (f) Assistive glove pressurized to  $240\text{kPa}$

Lastly, we make the device wearable by sewing it onto a large-size glove (Shima Seiki USA). Pressurizing all five of the actuators to  $240\text{ kPa}$ , we see that the glove produces a grasping motion, enabling the wearer to grasp a jar (Figure 5.4f). The articulated actuators have been designed to mimic finger motion, so they distribute pressure evenly over the fingers, in contrast to simple bending actuators which have constant curvature and produce a motion which is further from the natural motion of the fingers. While the glove stiffens and applies forces to the wearer when it is actuated, the compliance and flexibility of its constitutive materials make it transparent when not actuated. Note that since the glove is fabricated all in one piece (as shown in Figure 5.1d), the middle finger is aligned with the warp direction of the textile, as in the model, but the index, ring, and little fingers are at a slight angle to the warp. We ran a finite element simulation to compare

the behavior of an actuator aligned with the warp to the behavior of one at an angle of  $10^\circ$  and found that their behavior was quite similar, and therefore this angle did not affect the functionality of the glove (see Appendix B).

## 5.6 Conclusions

In summary, we have presented methods for rapidly manufacturing and modeling textile actuators. In particular we have shown how to laminate highly stretchable textiles to make them air-impermeable and heat-sealable. We have mechanically characterized these textile-film composites and used the characterization results in an analytical model which predicts the behavior of the actuators. The manufacturing and modeling methods allow for the rapid iteration of actuator designs, as the modeling process tells us the effect of changing actuator geometry, while the manufacturing process allows us to quickly investigate the effect of using different materials (such as different textiles or films with different properties). Our manufacturing process can easily be scaled to produce devices with more complex geometries, giving these actuators potential to be used in a wide range of wearable and assistive devices. These devices could aid people who have suffered injuries which impair their ability to perform activities of daily life, or could be used in factories to reduce work-related musculoskeletal injuries.

## 6 Conclusions and Outlook

### 6.1 Accomplishments of this thesis

In this thesis, I identified methods of modeling soft fluid-powered actuators and used those models to guide the design of the actuators. More specifically, I developed analytical and finite element models of two types of actuators and used these models to design actuators for specific functions.

In particular, I have studied elastomeric fiber-reinforced actuators and have focused on the effect of fiber angle on the deformation undergone by an actuator. This effect was explored in detail through experimentally-verified finite element analysis (FEA) in Chapter 3. The FEA allowed us to model the actuator's deformation response as a function of pressure, accounting for the geometry of the actuator and the mechanical properties of the elastomer and the fibers. I then used the knowledge gained from these simulations to design a device which consisted of four actuators connected in series, each with their own pressure inlet. Pressurizing the actuators in a certain sequence caused this device to move through a tube and perform an orientation-specific task at the end of the tube. This demonstrated that the compliance of soft actuators can be used to simplify peg-insertion tasks and that knowing how an actuator will behave as a function of pressure allows us to choose an actuator design appropriate to a specific task.

Following on from this work, in Chapter 4, I developed experimentally-verified analytical models of the same fiber-reinforced elastomeric actuators. I used nonlinear elasticity theory to develop an analytical model of an actuator which extends, expands, and twists upon inflation, and to develop a second model of an actuator which bends upon inflation. Analytical modeling has an advantage over finite element analysis in that it is much less computationally expensive and therefore much faster. The computational speed was fast enough to enable the use of the analytical models in an optimization algorithm to design segmented actuators capable of replicating particular motions upon pressurization, specifically, the motion of a finger and a thumb. This algorithm takes the desired trajectory, number of segments, and the type of each segment as inputs, and outputs the lengths and fiber angles of each segment which produces the closest match to the desired trajectory. In future work, this algorithm could be upgraded to allow the user to input only a sequence of desired configurations of the actuator. The algorithm would then process the configurations and break them up into different types of motions (bend, extend, twist) and thus different types of

segments. Furthermore the algorithm could easily be extended to find the optimal materials to be used in the actuator, given a material library.

In Chapter 5, I mechanically characterized textile-film composites and showed how they could be used to fabricate soft actuators quickly and easily. I used an energy minimization approach to analytically predict the deformation of the actuators as a function of pressure and to show how this deformation is affected by the geometry of the actuators. These modeling and manufacturing approaches then enabled the design of a glove which mimics the motion of a hand grasping a bottle. In the future this could be developed into a device to assist people who have difficulty performing grasping motions required for activities of daily life.

## **6.2 Future work**

### **6.2.1 Forces and interactions**

The work described in this thesis deals with free deformation of actuators, and for the most part, does not consider interactions of the actuator with its environment. But in most applications, it is of course essential to consider how an actuator interacts with its surroundings. It is necessary to know the forces that the actuator will apply to objects it comes into contact with, and also to know how contact with an object will affect the deformation of the actuator (compared to the deformation of the actuator in free space). This problem is particularly challenging for soft robots because they are so compliant. This compliance is one of the main advantages of soft robots; it allows them to interact safely with people, as forces are spread out over a large surface area, and enables them to function more reliably in an unknown environment, as they can conform to their surroundings. At the same time, this compliance makes them extremely difficult to model. For example, if a soft robot interacts with a person, the compliant soft robot meets compliant human tissue, resulting in a complex interaction. Furthermore, the behavior of the actuator depends on the fluid which is used for actuation – for example, since air is much more compressible than water, an actuator filled with air will behave differently to an actuator filled with water upon contacting an object.

Appendix A considered the forces produced by a blocked extending/twisting actuator. If the extension of the actuator is fixed, the analytical model predicts the axial force produced by the

actuator. Similarly, if the actuator is not permitted to twist, the resulting torque can be predicted. These results were verified using finite element analysis and similar results were verified experimentally by Sedal et al.[104] However, this model does not account for buckling or how the actuator would interact with a compliant surface. Additionally, Wang et al modeled interaction forces produced at the tip of a bending actuator.[41] However, interactions along the length of the actuator were not considered. Future work should explore the area of interaction forces in more detail. For example, it would be valuable to study the bending torques that an actuator in an assistive glove applies to the joints of a finger and also to investigate how these forces are affected by the stiffness of the finger.

### 6.2.2 Dynamic effects

A significant limitation of the models presented in this thesis is that they neglect dynamic effects. It is always assumed that the actuators are inflated slowly enough that they exhibit a quasi-static response. In the experiments, I inflated the actuators slowly and waited for any dynamic effects to dissipate before taking any measurements; this makes it easier to model actuator behavior. However, in many applications fast actuation is essential, and therefore the models should be extended to include dynamic effects. One such dynamic effect is the behavior of the material under fast loading. For example, hyperelastic materials often exhibit viscoelasticity, as explored by Moseley et al.[48] Furthermore, the geometric design of an actuator can have a significant effect on its actuation speed, as demonstrated by Mosadegh et al.[29] Another important consideration is the dynamics of the fluid flowing into the actuator, since the speed at which the fluid flows in will affect the motion of the actuator. Considering fluid flow and the properties of the fluid can also determine the maximum possible actuation speed. Many models in the literature have neglected dynamic effects, due to their complexity.[105, 3, 106] Of the models which do consider dynamic effects, most are models of McKibben actuators and mostly consider dynamic effects due to friction in the system.[22, 23, 107]

Future work on modeling soft actuators should focus on

1. using material models which account for viscoelasticity. This would model the actuator motion more accurately as a function of time as well as inflation pressure, and would account



for the hysteresis which is seen in actuator behavior (the actuator behavior upon inflation is different to its behavior upon deflation)

2. modeling fluid flow into the actuator. All the actuators in this thesis were inflated using air, which is highly compressible. They could easily be actuated using an incompressible fluid such as water instead. Their behavior as a function of pressure would of course be the same, but the fluid flow would be easier to model.

Many insights can still be gained into actuator behavior by considering only quasi-static behavior. However, in order to develop accurate models which can be used for control, it is important to account for dynamic effects.

### **6.2.3 Control**

To develop controllers for soft actuators, fast and accurate models must be developed. Finite element analysis is a very valuable tool in the design process for soft actuators. It provides highly accurate predictions of how the soft actuators will behave under different loading conditions, and in addition to yielding numerical output for stress and strain, it also allows us to visualize the actuator deformation. Despite the fact that analytical models are generally less accurate than FEA, analytical modeling is much faster and therefore has potential to be used in controlling soft robots. Soft robots are more difficult to control than traditional rigid robots because of their unusual dynamics, their many degrees of freedom, and their compliance which results in complex interactions with their environment.[80, 3] By developing accurate analytical models, we can improve prospects for controlling soft robots precisely. As a first step, the quasi-static models presented in this work could be used in feed-forward control of soft actuators.

## A Supporting Information for Chapters 3 and 4

### A.1 Material characterization

Dogbone-shaped samples (ASTM standard) made out of the elastomers used to fabricate the actuators (Elastosil M4601 – Wacker Chemie, Smooth-Sil 950 and Dragon Skin 10 – Smooth-on Inc., PA, USA) were tested under uniaxial tension using a single-axis Instron (model 5566; Instron, Inc.) with a 100N load cell. The material behavior is reported in Figures A.1 and A.2. We used a least squares method to fit an incompressible Neo-Hookean model to the measured data, and found that the material response is best captured with an initial shear modulus  $\mu = 0.24\text{MPa}$  for Elastosil,  $\mu = 0.085\text{MPa}$  for Dragon Skin 10, and  $\mu = 0.68\text{MPa}$  for Smooth-Sil 950.

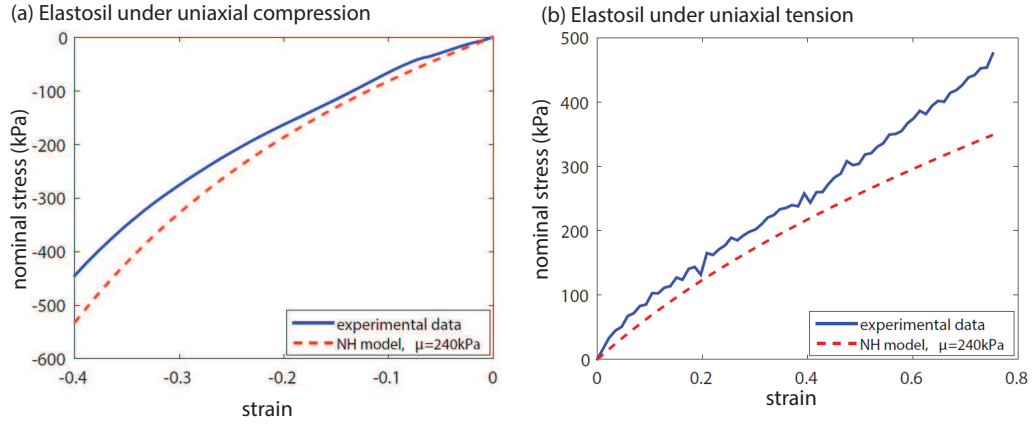


Figure A.1: Stress-strain curve for Elastosil under (a) uniaxial compression and (b) uniaxial tension. The blue line corresponds to the experimental data and the red line to the fit using the neo-Hookean model with an initial shear modulus,  $\mu = 240\text{kPa}$ .

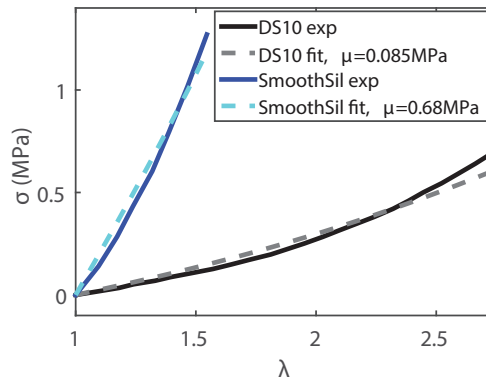


Figure A.2: Experimental stress-strain data and a best-fit neo-Hookean model for Dragonskin 10 and Smooth-Sil 950 under uniaxial tensile loading

## A.2 Actuator fabrication

In this section, we describe our methods for fabricating fiber-reinforced soft actuators. We first describe how to fabricate actuators which extend, expand, and twist, then actuators which bend, and finally, segmented actuators. We describe our procedure for molding the elastomeric tube, and for winding the fibers at a particular angle. We also describe the procedure for characterizing the elastomers used.

### A.2.1 Extending/Expanding/Twisting actuators

The actuator mold is designed in Solidworks and 3d printed using an Objet Connex 500 printer (Stratasys) (see Figure A.3A). The mold is assembled and held together firmly with clamps. Elastomer is poured into the mold (Figure A.3B), and degassed in a vacuum chamber for a couple of minutes. A cylindrical metal rod is inserted into the mold to create the core of the actuator. The rod slots into a round indentation at the bottom of the mold and a 3d printed cap holds the rod in place at the top of the mold (Figure A.3C). The elastomer is left overnight at room temperature to cure.

The next day, the plastic mold is removed. Kevlar fiber is wound in a helical pattern around the outside of the actuator (Figure A.3D). Ridges on the surface of the mold leave grooves on the actuator, which define the path for winding the fibers. In this way, we have precise control over the fiber angle. At each end of the actuator, the fiber is looped around a few times and tied. These knots are held in place by applying a small amount of Sil-Poxy (Smooth-On, Inc.). The actuator is then removed from the rod using isopropanol as a lubricant. The ends of the actuator are plugged with Sil-Poxy, and a vented screw is inserted at one end. The Sil-Poxy is allowed to cure for 24 hours.

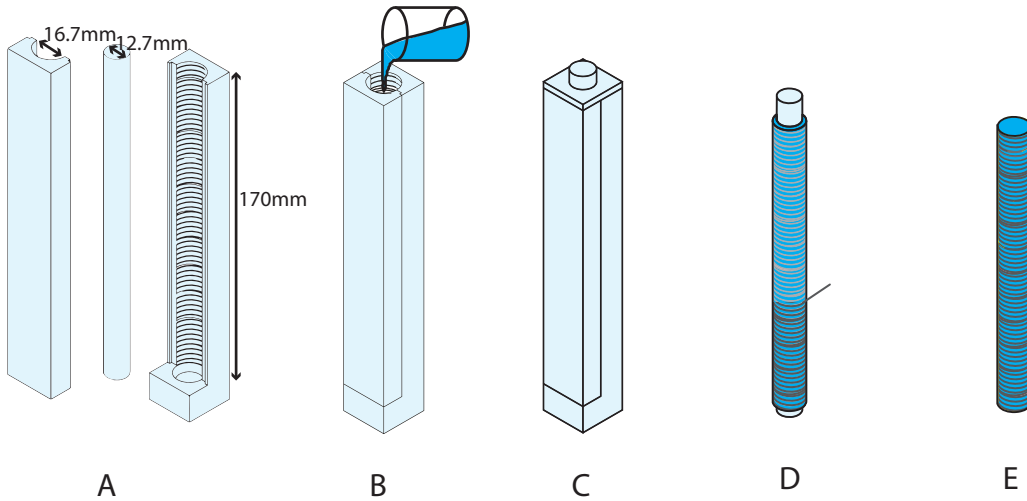


Figure A.3: Fabrication of an extending/expanding/twisting actuator. (A) A metal rod and 3d printed mold are used to mold the elastomer. (B) Elastomer is poured into the mold. (C) The rod is inserted into the mold and held in place with a 3d printed cap. (D) The mold is removed and Kevlar fiber is wound around the outside of the actuator. (E) The actuator is capped with Sil-Poxy.

### A.2.2 Bending actuators

The fabrication procedure for bending actuators is similar to the procedure for extending/expanding/twisting actuators. The only difference is that the cylindrical tube is composed of two different elastomers. To fabricate the first half of this tube, one side of the 3d printed mold is laid down flat, and Elastomer 1 is poured into the mold (Figure A.4A). The metal rod is placed on top of the elastomer, and slots into place at the top and bottom of the mold. This is left to cure overnight in a pressure chamber (curing at high pressure reduces the size of any air bubbles present in the elastomer). The next day, the edges of the elastomer are trimmed (without removing it from the mold) so that it forms a perfect half-cylinder. Elastomer 2 (of different stiffness to Elastomer 1) is poured on top of the metal rod (Figure A.4B), and the top half of the mold is quickly placed on top. The two halves of the mold are held together firmly with clamps. Again, this is left overnight in a pressure chamber to allow the second elastomer to cure (Figure A.4C). The remainder of the procedure is the same as for the extending/expanding/twisting actuators.

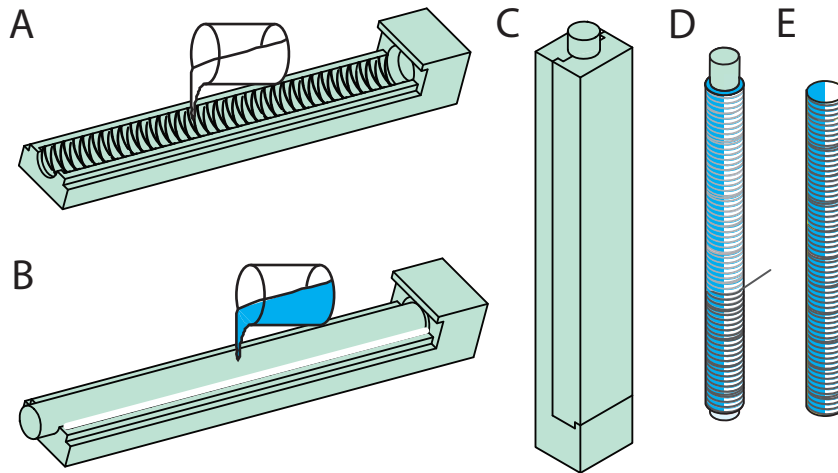


Figure A.4: Fabrication of a bending actuator (A) The first half of the mold is laid down flat and Elastomer 1 is poured in. (B) When Elastomer 1 has cured, Elastomer 2 is poured on top. (C) The second half of the mold is placed on top and Elastomer 2 is left to cure. (D) The mold is removed and Kevlar fiber is wound around the outside of the actuator. (E) The actuator is capped with Sil-Poxy.

### A.2.3 Segmented actuators

A segmented actuator consists of some bending actuator segments and some extending/twisting actuator segments. One half of the actuator is made entirely of Elastomer 1. The other half is made of Elastomer 1 if it is a twisting and/or extending segment, and Elastomer 2 (different stiffness) if it is a bending segment. Therefore, a segmented mold is used, as shown in Figure A.5A.

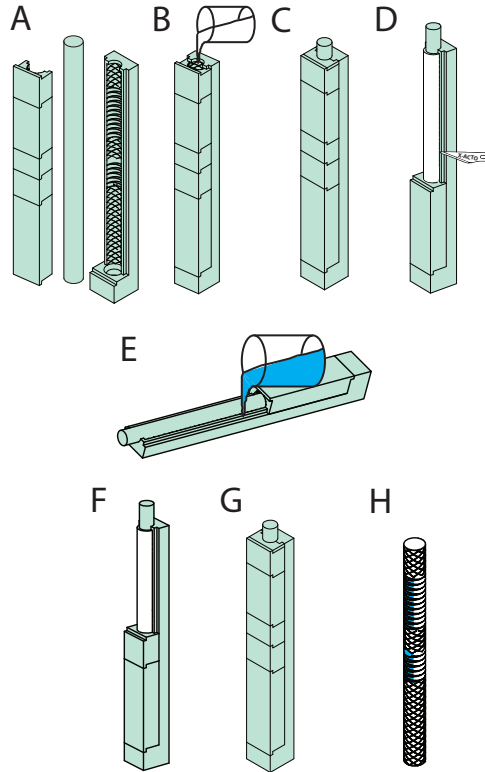


Figure A.5: Fabrication of a segmented actuator. (A) A metal rod and 3d printed mold are used to mold the elastomer. (B) First, Elastomer 1 is used to make the entire actuator. (C) Elastomer 1 is left to cure. (D)-(G) The elastomeric segments are fabricated one by one. (H) The mold is removed and the actuator is capped with Sil-Poxy.

First, the whole mold is assembled and held together with clamps, and the actuator is cast entirely from Elastomer 1 (Figure A.5B,C). Then one side of the mold (the segmented side) is removed. The segments are then fabricated one by one. As shown in Figure A.5D,E, the exposed elastomer is cut away, and the new elastomer is poured (Elastomer 1 or 2, depending on the type of segment). The elastomer is cut away segment by segment like this so that every time new elastomer is being poured, it is being poured on a freshly exposed surface. This improves the bond between the elastomers. To speed up the process, the elastomer is cured in the oven for 30 minutes at  $60^{\circ}\text{C}$

(rather than overnight at room temperature). When all of the segments have cured, the mold is removed, and fibers are wrapped around the outside of the actuator.

**Actuator segment lengths** In tables A.1-A.4 we report the intended initial lengths of each of the segments in the finger and thumb actuators (as prescribed by the optimization algorithm - see Section A.5) and compare them to the actual segment lengths in the actuators we fabricated. The discrepancies are due to small inconsistencies in the fabrication procedure, as well as the space taken up by the fibers wound around the actuator between segments.

| Index Finger Segments            |    |    |    |    |    |    |
|----------------------------------|----|----|----|----|----|----|
| segment                          | 1  | 2  | 3  | 4  | 5  | 6  |
| required initial length ( $mm$ ) | 70 | 22 | 22 | 28 | 15 | 15 |
| actual initial length ( $mm$ )   | 66 | 20 | 18 | 28 | 15 | 12 |
| % error                          | 6  | 9  | 18 | 0  | 0  | 20 |

Table A.1: Comparison of required segment length with achieved segment length for each segment of the finger actuator

| Index Finger Links               |    |    |      |      |
|----------------------------------|----|----|------|------|
| link                             | 1  | 2  | 3    | 4    |
| required initial length ( $mm$ ) | 81 | 47 | 21.5 | 22.5 |
| actual initial length ( $mm$ )   | 76 | 42 | 21.5 | 19.5 |
| % error                          | 6  | 11 | 0    | 13   |

Table A.2: Comparison of required link length with achieved link length for each link of the finger actuator

| Thumb Segments                   |    |    |    |    |    |    |    |
|----------------------------------|----|----|----|----|----|----|----|
| segment                          | 1  | 2  | 3  | 4  | 5  | 6  | 7  |
| required initial length ( $mm$ ) | 25 | 15 | 20 | 30 | 8  | 22 | 17 |
| actual initial length ( $mm$ )   | 25 | 16 | 18 | 27 | 7  | 22 | 17 |
| % error                          | 0  | 7  | 10 | 10 | 13 | 0  | 0  |

Table A.3: Comparison of required segment length with achieved segment length for each segment of the thumb actuator

| Thumb Links                      |      |      |    |
|----------------------------------|------|------|----|
| link                             | 1    | 2    | 3  |
| required initial length ( $mm$ ) | 42.5 | 34   | 28 |
| actual initial length ( $mm$ )   | 39.5 | 31.5 | 28 |
| % error                          | 7    | 7    | 0  |

Table A.4: Comparison of required link length with achieved link length for each link of the thumb actuator

### A.3 Finite element analysis

As well as performing experiments, we performed finite element simulations as additional verification for our analytical modeling. All finite element simulations were carried out using the commercial finite element software Abaqus (SIMULIA, Providence, RI). In each case, the elastomer was modeled as an incompressible neo-Hookean material. The Kevlar fibers were modeled as a linearly elastic material using the manufacturer’s specifications: diameter  $0.1778mm$ , Young’s modulus  $31.067 \times 10^6 kPa$  and Poisson’s ratio 0.36. For the elastomer, 20-node quadratic brick elements, with reduced integration (Abaqus element type C3D20R) were used, and 3-node quadratic beam elements (Abaqus element type B32) were used for the fibers. Perfect bonding between the fibers and the elastomer was assumed (the fibers were connected to the elastomer by tie constraints). Quasi-static non-linear simulations were performed using Abaqus/Standard. One end of the actuator was held fixed, and a pressure load was applied to the inner surface of the actuator.

Note that sample files for running Abaqus simulations can be found on [softroboticstoolkit.com](http://softroboticstoolkit.com).

### A.4 Analytical modeling

In this section, we present analytical models for fiber-reinforced actuators which extend, expand, twist, and bend. We use a non-linear elasticity approach to analytically model the response of the fiber-reinforced actuators free to deform under pressurization. Rather than modeling the tube and the fibers individually, we treat them as a homogeneous anisotropic material. More specifically, as the fibers are located on the outside of the tube and not dispersed throughout its thickness, we model the actuator as a hollow cylinder of isotropic incompressible hyperelastic material (corresponding to the elastomer), surrounded by a thin layer of anisotropic material (corresponding to the fiber



reinforcement), and impose continuity of deformation between the two layers (Figure 4.2A). The isotropic core has initial inner radius  $R_i$  and outer radius  $R_m$ , while the outer anisotropic layer has initial outer radius  $R_o$ . The anisotropic material has a preferred direction which is determined by the initial fiber orientation  $\mathbf{S} = (0, \cos \alpha, \sin \alpha)$ , where  $\alpha$  is the fiber angle.

In the following, we first construct the strain energy expressions for both the inner and outer layers. Then, to simplify the analytical modeling, we decouple bending from the other motions, so we first introduce a model for actuators which extend, expand, and twist upon pressurization, followed by a model for actuators which bend upon pressurization. In each case, we use experimental and finite element results to validate the analytical models.

#### A.4.1 Strain energy for the actuators

The inner and outer layers require different strain energy expressions, so let  $W^{(in)}$  be the strain energy for the isotropic core, and  $W^{(out)}$  be the strain energy for the anisotropic outer layer. For the isotropic core, we choose a simple incompressible neo-Hookean model, so that

$$W^{(in)} = \frac{\mu}{2}(I_1 - 3), \quad (\text{A.1})$$

$\mu$  denoting the initial shear modulus and  $I_1 = \text{tr}(\mathbf{F}\mathbf{F}^T)$ ,  $\mathbf{F}$  being the deformation gradient. For the anisotropic layer, let  $W^{(out)}$  be the sum of two components,

$$W^{(out)} = c_1 W^{(iso)} + c_2 W^{(aniso)}, \quad (\text{A.2})$$

where  $W^{(iso)} = \mu/2(I_1 - 3)$  is the contribution from the isotropic elastomeric matrix,  $W^{(aniso)}$  is the contribution from the fibers, and  $c_i$  are the corresponding volume fractions. To derive a suitable expression for  $W^{(aniso)}$ , we consider a helical fiber with cross-sectional area  $\hat{a}$ , initial orientation  $\mathbf{S} = (0, \cos \alpha, \sin \alpha)$ , and current orientation  $\mathbf{s} = \mathbf{F}\mathbf{S}$  subject to an axial load  $\bar{F}$  (Figure A.6A). We focus on a small segment of the helical fiber of length  $dl$  which undergoes a change in length  $dx$ . Assuming there is a linear relationship between the force  $\bar{F}$  and extension  $dx$  (as shown in Figure S5B), the strain energy for the segment,  $dW^{(fiber)}$ , is equal to the area underneath the

force-displacement curve,

$$dW^{(fiber)} = \frac{1}{2}\bar{F}dx. \quad (\text{A.3})$$

For the considered linear elastic fiber  $\bar{F}$  can be expressed as

$$\bar{F} = E\epsilon\hat{a} \quad (\text{A.4})$$

where  $\epsilon = dx/dl$  is the axial strain, and  $E$  is the Young's modulus. Substituting Equation (A.4) into Equation (A.3), we have

$$dW^{(fiber)} = \frac{1}{2}\epsilon E\hat{a}dx = \frac{1}{2}\epsilon^2 E\hat{a}dl, \quad (\text{A.5})$$

and integrating yields

$$W^{(fiber)} = \int_0^{L_f} \frac{1}{2}\epsilon^2 E\hat{a}dl = \frac{1}{2}\epsilon^2 E\hat{a}L_f, \quad (\text{A.6})$$

which is the energy of the helical fibers. Since  $I_4 = \mathbf{s} \cdot \mathbf{s}$  is the stretch of the fiber, we have  $\epsilon = \sqrt{I_4} - 1$ , and substituting this in Equation (A.6) yields

$$W^{(fiber)} = \frac{(\sqrt{I_4} - 1)^2 E\hat{a}L_f}{2} \quad (\text{A.7})$$

Dividing by the volume of the fiber yields the strain energy density

$$W^{(aniso)} = \frac{(\sqrt{I_4} - 1)^2 E}{2}. \quad (\text{A.8})$$

If an actuator has multiple sets of fibers (i.e. fibers arranged at different fiber angles), the strain energy can easily be modified to account for this. For example, suppose the actuator has two sets of fibers: one set at a fiber angle  $\alpha_1$  (i.e. with initial fiber orientation  $\mathbf{S}_1 = (0, \cos \alpha_1, \sin \alpha_1)$ , and current fiber orientation  $\mathbf{s}_1 = \mathbf{F}\mathbf{S}_1$ ), and one set at a fiber angle  $\alpha_2$  (i.e. with initial fiber orientation  $\mathbf{S}_2 = (0, \cos \alpha_2, \sin \alpha_2)$ , and current fiber orientation  $\mathbf{s}_2 = \mathbf{F}\mathbf{S}_2$ ). Then the strain energy is

$$W^{(aniso)} = \frac{(\sqrt{I_4} - 1)^2 E}{2} + \frac{(\sqrt{I_6} - 1)^2 E}{2}, \quad (\text{A.9})$$

where  $I_4 = \mathbf{s}_1 \cdot \mathbf{s}_1$  and  $I_6 = \mathbf{s}_2 \cdot \mathbf{s}_2$ . Similarly, for three sets of fibers, we have strain energy

$$W^{(aniso)} = \frac{(\sqrt{I_4} - 1)^2 E}{2} + \frac{(\sqrt{I_6} - 1)^2 E}{2} + \frac{(\sqrt{I_{10}} - 1)^2 E}{2}, \quad (\text{A.10})$$

where  $I_{10} = \mathbf{s}_3 \cdot \mathbf{s}_3$ .

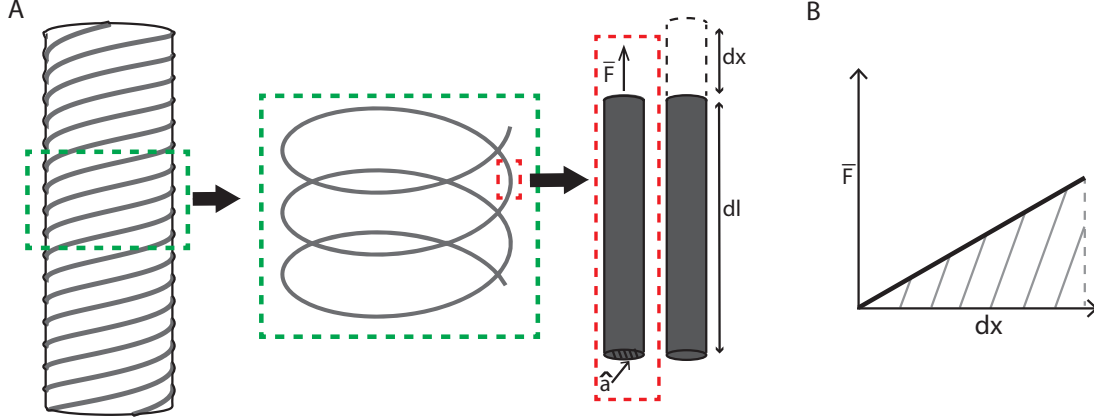


Figure A.6: (A) The helical fiber is modeled as a rod, of cross-sectional area  $\hat{a}$ , undergoing axial extension  $dx$  due to an axial load  $\bar{F}$ . (B) We assume the fiber extends linearly with applied force. The strain energy is then equal to the area underneath the force-displacement curve (the shaded area).

#### A.4.2 Modeling extension, expansion, and twist

When the elastomeric part of the actuator is of uniform stiffness, we assume that the tube retains its cylindrical shape upon pressurization, and the radii become  $r_i$ ,  $r_m$ , and  $r_o$  in the pressurized configuration (Figure 4.2B). The possible extension, expansion, and twisting deformations are then described by

$$\begin{aligned} r^2 - r_o^2 &= \lambda_z^{-1}(R^2 - R_o^2), \\ \theta &= \Theta + \tau \lambda_z Z, \\ z &= \lambda_z Z, \end{aligned} \quad (\text{A.11})$$

from which the deformation gradient can be obtained as

$$\mathbf{F} = \begin{pmatrix} \frac{\partial r}{\partial R} & \frac{1}{R} \frac{\partial r}{\partial \Theta} & \frac{\partial r}{\partial Z} \\ r \frac{\partial \theta}{\partial R} & \frac{r}{R} \frac{\partial \theta}{\partial \Theta} & r \frac{\partial \theta}{\partial Z} \\ \frac{\partial z}{\partial R} & \frac{1}{R} \frac{\partial z}{\partial \Theta} & \frac{\partial z}{\partial Z} \end{pmatrix} = \begin{pmatrix} \frac{R}{r \lambda_z} & 0 & 0 \\ 0 & \frac{r}{R} & r \tau \lambda_z \\ 0 & 0 & \lambda_z \end{pmatrix}$$

where  $R, \Phi, Z$  and  $r, \phi, z$  are the radial, circumferential, and longitudinal coordinates in the reference and current configurations, respectively [2,4]. Moreover,  $\lambda_z$  and  $\tau$  denote the axial stretch and the twist per unit length, respectively. The deformation gradient  $\mathbf{F}$  is used to calculate the left Cauchy-Green deformation tensor  $\mathbf{B} = \mathbf{F}\mathbf{F}^T$  and the current fiber orientation  $\mathbf{s} = \mathbf{F}\mathbf{S}$ , from which we obtain the tensor invariants  $I_1 = \text{tr}(\mathbf{B})$  and  $I_4 = \mathbf{s} \cdot \mathbf{s}$ . Finally, we can then use the strain energies of Equations A.1 and A.2 to calculate the Cauchy stresses, which take the form

$$\begin{aligned}\sigma^{(in)} &= 2W_1^{(in)}\mathbf{B} - p\mathbf{I} \\ \sigma^{(out)} &= 2W_1^{(out)}\mathbf{B} + 2W_4^{(out)}\mathbf{s}_1 \otimes \mathbf{s}_1 + 2W_6^{(out)}\mathbf{s}_2 \otimes \mathbf{s}_2 - p\mathbf{I}\end{aligned}\tag{A.12}$$

where  $W_i = \frac{\partial W}{\partial I_i}$ ,  $\mathbf{I}$  is the identity matrix, and  $p$  is a hydrostatic pressure.

To determine the current actuator configuration, we first apply the Cauchy equilibrium equations (i.e.  $\text{div}(\sigma) = 0$ ), yielding

$$\frac{d\sigma_{rr}}{dr} = \frac{\sigma_{\theta\theta} - \sigma_{rr}}{r},\tag{A.13}$$

which can then be integrated to yield

$$P = \int_{r_i}^{r_m} \frac{\sigma_{\theta\theta}^{(in)} - \sigma_{rr}^{(in)}}{r} dr + \int_{r_m}^{r_o} \frac{\sigma_{\theta\theta}^{(out)} - \sigma_{rr}^{(out)}}{r} dr,\tag{A.14}$$

where  $P$  is the pressure applied inside the tube. Assuming there are no external axial forces or external axial moments applied to the tube, the axial load  $N$  can be obtained as

$$N = 2\pi \int_{r_i}^{r_m} \sigma_{zz}^{(in)} r dr + 2\pi \int_{r_m}^{r_o} \sigma_{zz}^{(out)} r dr = P\pi r_i^2,\tag{A.15}$$

while the axial moment  $M$  is given by

$$M = 2\pi \int_{r_i}^{r_m} \sigma_{\theta z}^{(in)} r^2 dr + 2\pi \int_{r_m}^{r_o} \sigma_{\theta z}^{(out)} r^2 dr = 0.\tag{A.16}$$

Equation (A.15) can be manipulated as follows:

$$\begin{aligned}
N &= 2\pi \int_{r_i}^{r_m} \sigma_{zz}^{(in)} r dr + 2\pi \int_{r_m}^{r_o} \sigma_{zz}^{(out)} r dr \\
&= 2\pi \int_{r_i}^{r_m} (\sigma_{zz}^{(in)} - \sigma_{rr}^{(in)} + \sigma_{\theta\theta}^{(in)}) r dr + 2\pi \int_{r_m}^{r_o} (\sigma_{zz}^{(out)} - \sigma_{rr}^{(out)} + \sigma_{\theta\theta}^{(out)}) r dr \\
&= 2\pi \int_{r_i}^{r_m} (\sigma_{zz}^{(in)} - \sigma_{rr}^{(in)}) r dr + 2\pi \left[ \frac{\sigma_{rr}^{(in)} r^2}{2} \right]_{r_i}^{r_m} - 2\pi \int_{r_i}^{r_m} \frac{r^2}{2} \frac{d\sigma_{rr}^{(in)}}{dr} \\
&\quad + 2\pi \int_{r_m}^{r_o} (\sigma_{zz}^{(out)} - \sigma_{rr}^{(out)}) r dr + 2\pi \left[ \frac{\sigma_{rr}^{(out)} r^2}{2} \right]_{r_m}^{r_o} - 2\pi \int_{r_m}^{r_o} \frac{r^2}{2} \frac{d\sigma_{rr}^{(out)}}{dr} \\
&= 2\pi \int_{r_i}^{r_m} (\sigma_{zz}^{(in)} - \sigma_{rr}^{(in)}) r dr + P\pi r_i^2 - \pi \int_{r_i}^{r_m} r^2 \frac{\sigma_{\theta\theta}^{(in)} - \sigma_{rr}^{(in)}}{r} dr \\
&\quad + 2\pi \int_{r_m}^{r_o} (\sigma_{zz}^{(out)} - \sigma_{rr}^{(out)}) r dr - \pi \int_{r_m}^{r_o} r^2 \frac{\sigma_{\theta\theta}^{(out)} - \sigma_{rr}^{(out)}}{r} dr \\
&= \pi \int_{r_i}^{r_m} (2\sigma_{zz}^{(in)} - \sigma_{rr}^{(in)} - \sigma_{\theta\theta}^{(in)}) r dr + P\pi r_i^2 + \pi \int_{r_m}^{r_o} (2\sigma_{zz}^{(out)} - \sigma_{rr}^{(out)} - \sigma_{\theta\theta}^{(out)}) r dr
\end{aligned} \tag{A.17}$$

Combining Equations (A.15) and (A.17), we have

$$N = \pi \int_{r_i}^{r_m} (2\sigma_{zz}^{(in)} - \sigma_{rr}^{(in)} - \sigma_{\theta\theta}^{(in)}) r dr + P\pi r_i^2 + \pi \int_{r_m}^{r_o} (2\sigma_{zz}^{(out)} - \sigma_{rr}^{(out)} - \sigma_{\theta\theta}^{(out)}) r dr = P\pi r_i^2 \tag{A.18}$$

Now canceling the  $P\pi r_i^2$  on the left side of the equation with the  $P\pi r_i^2$  term on the right side of the equation, we can write the *reduced axial load* (that is, the axial load due to forces other than the applied pressure)[71]

$$N_{ral} = \pi \int_{r_i}^{r_m} (2\sigma_{zz}^{(in)} - \sigma_{rr}^{(in)} - \sigma_{\theta\theta}^{(in)}) r dr + \pi \int_{r_m}^{r_o} (2\sigma_{zz}^{(out)} - \sigma_{rr}^{(out)} - \sigma_{\theta\theta}^{(out)}) r dr = 0. \tag{A.19}$$

Finally, defining  $\lambda_\theta = \frac{r}{R}$  and  $\gamma = r\tau$ , and using the identities [89]

$$\begin{aligned}
\sigma_{\theta\theta} - \sigma_{rr} &= \lambda_\theta \frac{\partial W}{\partial \lambda_\theta} + \gamma \frac{\partial W}{\partial \gamma} \\
\sigma_{\theta\theta} + \sigma_{zz} - 2\sigma_{rr} &= \lambda_\theta \frac{\partial W}{\partial \lambda_\theta} + \lambda_z \frac{\partial W}{\partial \lambda_z} \\
\sigma_{\theta z} &= \frac{\partial W}{\partial \gamma},
\end{aligned} \tag{A.20}$$

we can write the equilibrium equations in terms of the strain energy:

$$P = \int_{r_i}^{r_m} \lambda_z \frac{\partial W^{(in)}}{\partial \lambda_z} + \gamma \frac{\partial W^{(in)}}{\partial \gamma} \frac{dr}{r} + \int_{r_m}^{r_o} \lambda_z \frac{\partial W^{(out)}}{\partial \lambda_z} + \gamma \frac{\partial W^{(out)}}{\partial \gamma} \frac{dr}{r} \quad (\text{A.21})$$

$$N_{ral} = \pi \int_{r_i}^{r_m} 2\lambda_z \frac{\partial W^{(in)}}{\partial \lambda_z} - \lambda_\theta \frac{\partial W^{(in)}}{\partial \lambda_\theta} - 3\gamma \frac{\partial W^{(in)}}{\partial \gamma} r dr + \pi \int_{r_m}^{r_o} 2\lambda_z \frac{\partial W^{(out)}}{\partial \lambda_z} - \lambda_\theta \frac{\partial W^{(out)}}{\partial \lambda_\theta} - 3\gamma \frac{\partial W^{(out)}}{\partial \gamma} r dr = 0 \quad (\text{A.22})$$

$$M = 2\pi \int_{r_i}^{r_m} \frac{\partial W^{(in)}}{\partial \gamma} r^2 dr + 2\pi \int_{r_m}^{r_o} \frac{\partial W^{(out)}}{\partial \gamma} r^2 dr = 0 \quad (\text{A.23})$$

**Taylor Expansion** Since Equations (A.21)-(A.23) are quite complex and it is computationally intensive to solve them numerically, for thin-walled actuators we simplify the calculations by Taylor expanding the equations.

We define  $\varepsilon_1 = \frac{R_m - R_i}{R_i}$  and  $\varepsilon_2 = \frac{R_o - R_m}{R_m}$ , and Taylor expand Equations (A.21)-(A.23). Our goal was to retain the minimum number of terms required to give an accurate solution. We found that retaining first order terms in  $\varepsilon_2$  was sufficient, but for  $\varepsilon_1$ , we had to retain terms to third order, since  $\varepsilon_1 \gg \varepsilon_2$ . This gave us the following system of equations:

$$\begin{aligned} P = & \frac{R_i}{r_i \lambda_z} \frac{\partial W_1}{\partial \lambda_\theta} \varepsilon_1 + \frac{R_m}{r_m \lambda_z} \frac{\partial W_2}{\partial \lambda_\theta} \varepsilon_2 + \frac{1}{2r_i^3 \lambda_z^2} \left[ -R_i^3 \frac{\partial W_1}{\partial \lambda_\theta} + r_i(R_i^2 - r_i^2 \lambda_z) \frac{\partial^2 W_1}{\partial \lambda_\theta^2} \right] \varepsilon_1^2 \\ & + \frac{1}{6r_i^5 R_i \lambda_z^3} \left[ (3R_i^6 - r_i^2 R_i^4 \lambda_z) \frac{\partial W_1}{\partial \lambda_\theta} - r_i(R_i^2 - r_i^2 \lambda_z) \left( (3R_i^3 + 2r_i^2 R_i \lambda_z) \frac{\partial^2 W_1}{\partial \lambda_\theta^2} + r_i(-R_i^2 + r_i^2 \lambda_z) \frac{\partial^3 W_1}{\partial \lambda_\theta^3} \right) \right] \varepsilon_1^3 \\ & + \mathcal{O}(\varepsilon_1^4) + \mathcal{O}(\varepsilon_2^2) \quad (\text{A.24}) \end{aligned}$$

$$\begin{aligned} N_{ral} = & \frac{R_i \pi}{\lambda_z} \left[ 2R_i \lambda_z \frac{\partial W_1}{\partial \lambda_z} - r_i \frac{\partial W_1}{\partial \lambda_\theta} \right] \varepsilon_1 + \frac{B\pi}{\lambda_z} \left[ 2R_m \lambda_z \frac{\partial W_2}{\partial \lambda_z} - r_m \frac{\partial W_2}{\partial \lambda_\theta} \right] \varepsilon_2 \\ & + \frac{\pi}{2r_i \lambda_z^2} \left[ 2r_i R_i^2 \lambda_z^2 \frac{\partial W_1}{\partial \lambda_z} - R_i^3 \frac{\partial W_1}{\partial \lambda_\theta} + (R_i^2 - r_i^2 \lambda_z) \left( 2R_i \lambda_z \frac{\partial^2 W_1}{\partial \lambda_\theta \partial \lambda_z} - r_i \frac{\partial^2 W_1}{\partial \lambda_\theta^2} \right) \right] \varepsilon_1^2 \\ & + \frac{\pi(-R_i^2 + r_i^2 \lambda_z)}{6r_i^3 R_i \lambda_z^3} \left[ -R_i^4 \frac{\partial W_1}{\partial \lambda_\theta} + 2R_i^4 \lambda_z \frac{\partial^2 W_1}{\partial \lambda_\theta \partial \lambda_z} + r_i \left( (R_i^3 - 2r_i^2 R_i \lambda_z) \frac{\partial^2 W_1}{\partial \lambda_\theta^2} - (R_i^2 - r_i^2 \lambda_z) (2R_i \lambda_z \frac{\partial^3 W_1}{\partial \lambda_\theta^2 \partial \lambda_z} - r_i \frac{\partial^3 W_1}{\partial \lambda_\theta^3}) \right) \right] \\ & + \mathcal{O}(\varepsilon_1^4) + \mathcal{O}(\varepsilon_2^2) \quad (\text{A.25}) \end{aligned}$$

$$\begin{aligned}
M = & \frac{2r_i R_i^2 \pi}{\lambda_z} \frac{\partial W_1}{\partial \gamma} \varepsilon_1 + \frac{2r_m R_m^2 \pi}{\lambda_z} \frac{\partial W_2}{\partial \gamma} \varepsilon_2 + \frac{R_i \pi}{r_i \lambda_z^2} \left[ (R_i^3 + r_i^2 R_i \lambda_z) \frac{\partial W_1}{\partial \gamma} + r_i (R_i^2 - r_i^2 \lambda_z) \frac{\partial^2 W_1}{\partial \lambda_\theta \partial \gamma} \right] \varepsilon_1^2 + \\
& \frac{\pi}{3r_i^3 L z^3} \left[ -(R_i^6 - 3r_i^2 R_i^4 \lambda_z) \frac{\partial W_1}{\partial \gamma} + r_i (R_i^2 - r_i^2 \lambda_z) \left( R_i^3 \frac{\partial^2 W_1}{\partial \lambda_\theta \partial \gamma} + r_i (R_i^2 - r_i^2 \lambda_z) \frac{\partial^3 W_1}{\partial \lambda_\theta^2 \partial \gamma} \right) \right] \varepsilon_1^3 \\
& + \mathcal{O}(\varepsilon_1^4) + \mathcal{O}(\varepsilon_2^2) \quad (\text{A.26})
\end{aligned}$$

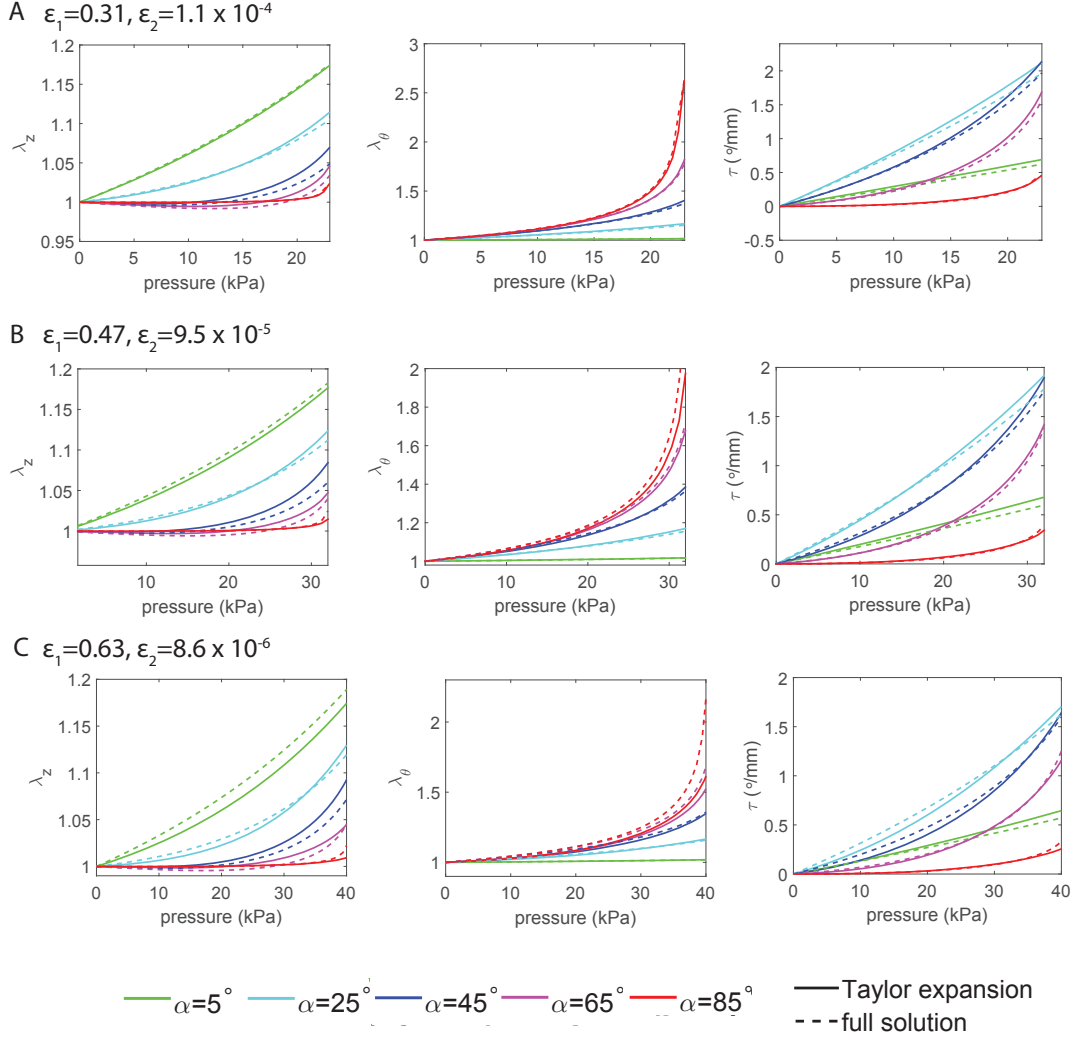


Figure A.7: Comparison of solution using full system of equations (Equations (19)-(21)) with solution using Taylor expanded equations (Equations (22)-(24)). (A) Results for an actuator with ratios  $\varepsilon_1 = 0.31$  and  $\varepsilon_2 = 1.1 \times 10^{-4}$ . (B) Results for an actuator with ratios  $\varepsilon_1 = 0.47$  and  $\varepsilon_2 = 9.5 \times 10^{-5}$ . In each of these cases, we see that the Taylor expansion provides a close approximation to the full solution. However, for a thicker-walled actuator, the Taylor expansion becomes less accurate. This is shown in (C), where we have ratios  $\varepsilon_1 = 0.63$  and  $\varepsilon_2 = 8.6 \times 10^{-6}$ , and observe that the Taylor expansion deviates significantly from the full solution.

As shown in Figure A.7, this expansion is valid for  $\varepsilon_1 \leq 0.47$  (Figure A.7A,B). However, as  $\varepsilon_1$

increases, the Taylor expansion becomes less accurate. This is shown in Figure A.7C, where we have  $\epsilon_1 = 0.63$ , and observe that the Taylor expansion deviates significantly from the full solution.

**Verification of the Model** To verify the analytical model for actuators which extend, expand, and twist, we fabricated some actuators from Dragon Skin 10 and from Smooth-Sil 950. In Figure A.8, we compare the analytical prediction to the experimental results for two actuators ( $\alpha = 3^\circ$  and  $\alpha = 70^\circ$ ) for each material. Each actuator had inner radius  $R_i = 6.35\text{mm}$ , wall thickness  $R_o - R_i = 2\text{mm}$ , and length  $L = 160\text{mm}$ . The number of fibers was  $n = \text{round}(13 \sin \alpha)$ , and the fibers had radius  $r = 0.0889\text{mm}$  and Young's modulus  $E = 31067\text{MPa}$ . We found that the response of the actuators was best captured choosing the fitting parameter  $R_o - R_m = 8.89 \times 10^{-4}\text{mm}$ , so that  $\epsilon_1 = 0.31$  and  $\epsilon_2 = 1.1 \times 10^{-4}$ . For this choice of  $R_m$  the volume fractions were  $c_1 = \frac{\pi(R_o^2 - R_m^2)L}{\pi(R_o^2 - R_m^2)L + n \times \pi r^2 \times \frac{L}{\sin \alpha}}$  and  $c_2 = \frac{n \times \pi r^2 \times \frac{L}{\sin \alpha}}{\pi(R_o^2 - R_m^2)L + n \times \pi r^2 \times \frac{L}{\sin \alpha}}$ . In each case shown in Figure A.8, we see good agreement between the analytical prediction and the experimental results. Some deviations in Figure A.8A are most likely due to inaccuracies in the fabrication procedure. We also see some deviations at higher pressures in Figure A.8B due to the highly nonlinear response of the actuators.

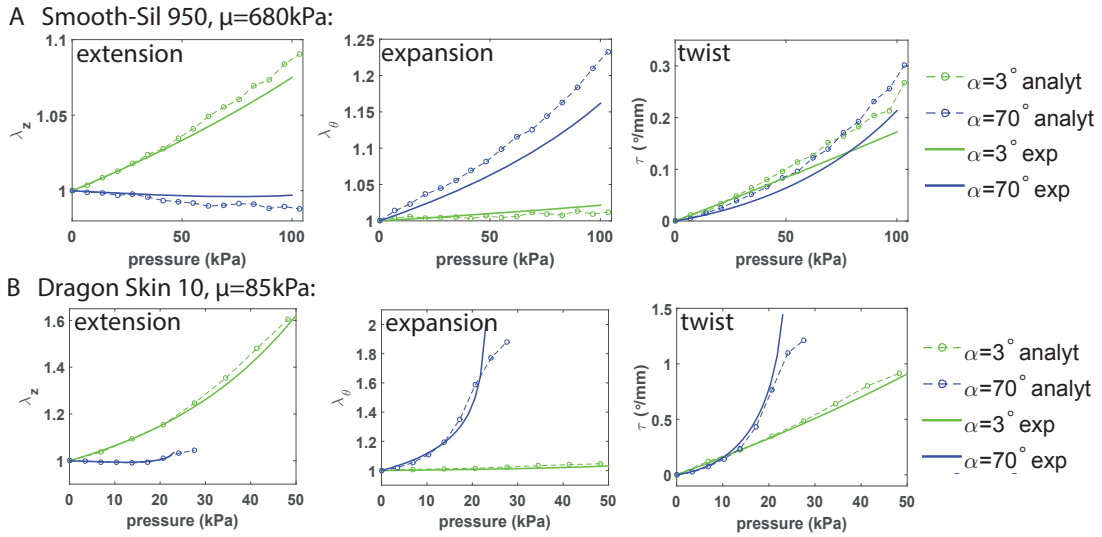


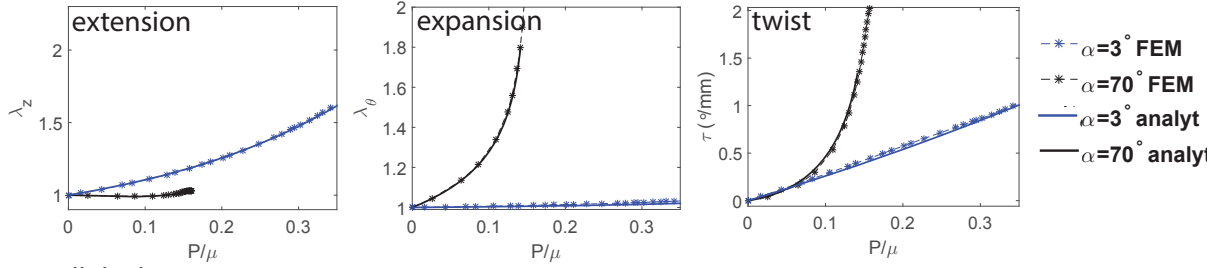
Figure A.8: Comparison of experimental results and analytical predictions for (A) Smooth-Sil 950 and (B) Dragon Skin 10. For each material, two actuators are shown: one with fiber angle  $\alpha = 3^\circ$  and one with fiber angle  $\alpha = 70^\circ$ . Axial stretch  $\lambda_z$  (left), radial stretch  $\lambda_\theta$  (center), and twist per unit length  $\tau$  (right) are shown in each case.

We used finite element analysis to verify that the model is valid for actuators with different wall thicknesses (see Figure A.9). Each actuator had inner radius  $R_i = 6.35\text{mm}$ , and length



$L = 160\text{mm}$ . Wall thicknesses were either  $R_o - R_i = 1\text{mm}$  or  $R_o - R_i = 3\text{mm}$  and materials were either Dragon Skin 10 or Smooth-Sil 950, as shown in Figure A.9. Also in this case we chose  $R_o - R_m = 8.89 \times 10^{-4}\text{mm}$ , so that  $\epsilon_1 = 0.16$  and  $\epsilon_2 = 1.2 \times 10^{-4}$  for the thinner actuator and  $\epsilon_1 = 0.47$  and  $\epsilon_2 = 9.5 \times 10^{-5}$  for the thicker one. In each case, we see excellent agreement between the analytical predictions and the finite element results.

**A wall thickness 1mm:**



**B wall thickness 3mm:**

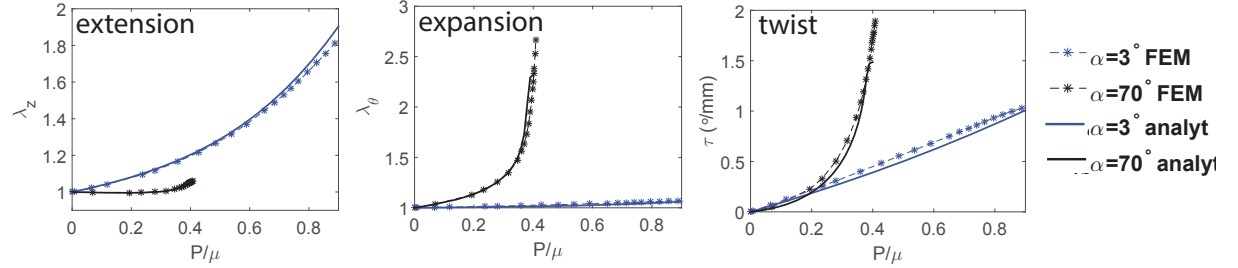


Figure A.9: Verification of extend/expand/twist model for Dragonskin 10, for wall thicknesses of 1mm and 3mm. For each wall thickness, two actuators are shown: one with fiber angle  $\alpha = 3^\circ$  and one with fiber angle  $\alpha = 70^\circ$ . Axial stretch  $\lambda_z$  (left), radial stretch  $\lambda_\theta$  (center), and twist per unit length  $\tau$  (right) are shown in each case.

**Predicting Forces and Torques** We can also use the analytical model to predict the force output for an actuator. If we constrain the actuator so it cannot extend axially, as shown in Figure A.10A, then we can output the axial force produced by the actuator. We also output the expansion and twist, as before. These results are shown in Figure A.10B-D, and we see good agreement between analytical and finite element models. Minor discrepancies are most likely due to non-uniform deformation of the actuator in the finite element simulations.

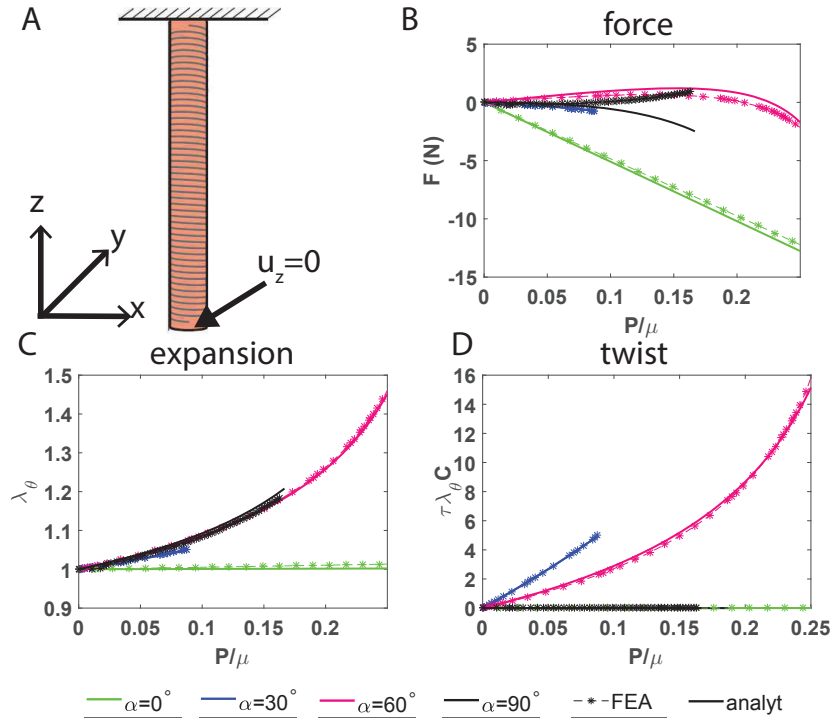


Figure A.10: (A) Schematic of an actuator which is constrained so it cannot extend axially. (B)-(D) Comparison of analytical and finite element predictions of the actuator deformation and axial force produced as functions of the normalized pressure.

Similarly, we can apply a boundary condition which does not allow rotation of the actuator, and then the model can be used to output the torque produced at the end of the actuator (as well as the extension and expansion, as before). These results are shown in Figure A.11, and here we see excellent agreement between analytical and finite element models.

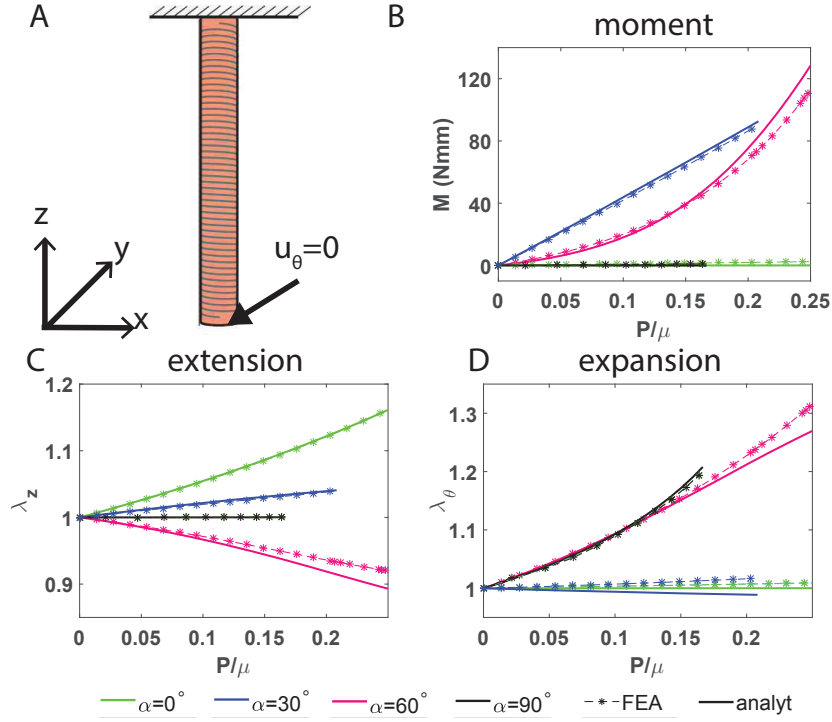


Figure A.11: (A) Schematic of an actuator which is constrained so it cannot rotate. (B)-(D) Comparison of analytical and finite element predictions of the actuator deformation and moment produced as functions of the normalized pressure.

#### A.4.3 Modeling bending

Since the exact solution for the finite bending of an elastic body is only possible under the assumption that the cross-sections of the cylinder remain planar upon pressurization - a condition that is severely violated by our actuator - we assume (i) that the radial expansion can be neglected (i.e.  $r/R = 1$ ) and (ii) vanishing stress in the radial direction (i.e.  $\sigma_{rr} = 0$ ). Furthermore, since the actuators have a symmetric arrangement of fibers, no twisting takes place, so the deformation

gradient reduces to

$$\mathbf{F} = \begin{pmatrix} \lambda_z(\phi)^{-1} & 0 & 0 \\ 0 & 1 & 0 \\ 0 & 0 & \lambda_z(\phi) \end{pmatrix}. \quad (\text{A.27})$$

Since the actuator bends due to the moment created by the internal pressure acting on the actuator caps,  $M_{cap}$ , the relationship between input pressure and bend angle can be found by equating  $M_{cap}$  to the opposing moment due to the stress in the material,  $M_{mat}$ .

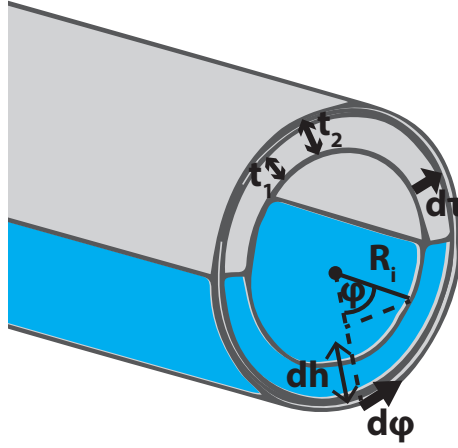


Figure A.12: Cross section of the actuator, with inner radius  $R_i$ . The thickness of the inner layer is  $t_1$ , and total wall thickness is  $t_2$ . The differential angle element is  $d\phi$ , differential wall thickness element is  $d\tau$ , and differential height is  $dh$ .

**Calculating  $M_{cap}$**  To calculate the moment ( $M_{cap}$ ) due to air pressure acting on the internal cap of the actuator, we start by noting that the force due to the air pressure acting on an infinitesimal area of the actuator cap  $dA = 2R_i \sin \phi dh$  is

$$df = P dA = P 2R_i \sin \phi dh, \quad (\text{A.28})$$

where  $P$  is the internal pressure in the actuator, and  $d\phi$  and  $dh$  are the differential angle and height respectively, as shown in Figure A.12. By re-writing  $h$  in terms of  $\phi$  as

$$h = R_i - R_i \cos \phi \Rightarrow dh = R_i \sin \phi d\phi, \quad (\text{A.29})$$

we can eliminate  $h$  from Equation (A.28)

$$df = P 2R_i^2 \sin^2 \phi d\phi. \quad (\text{A.30})$$

The moment acting on the cap is then

$$\begin{aligned} M_{cap} &= \int_0^{2R_i} df \times \text{distance from neutral axis} \\ &= 2PR_i^2 \int_0^\pi \sin^2 \phi \text{abs} [R_i \cos \bar{\phi} - R_i \cos \phi] d\phi, \end{aligned} \quad (\text{A.31})$$

where  $\bar{\phi}$  indicates the position of the neutral axis.

**Calculating  $M_{mat}$**  The moment due to the stress in the material,  $M_{mat}$ , is

$$\begin{aligned} M_{mat} &= 2 \int_0^{t_1} \int_{\frac{\pi}{2}}^\pi \lambda_z(\phi)^{-1} \sigma_{zz}^{(in,1)}(R_i + \tau) (R_i \cos \bar{\phi} - (R_i + \tau) \cos \phi) d\phi d\tau \\ &\quad + 2 \int_{t_1}^{t_2} \int_{\frac{\pi}{2}}^\pi \lambda_z(\phi)^{-1} \sigma_{zz}^{(out,1)}(R_i + \tau) (R_i \cos \bar{\phi} - (R_i + \tau) \cos \phi) d\phi d\tau \\ &\quad + 2 \int_0^{t_1} \int_0^{\frac{\pi}{2}} \lambda_z(\phi)^{-1} \sigma_{zz}^{(in,2)}(R_i + \tau) (R_i \cos \bar{\phi} - (R_i + \tau) \cos \phi) d\phi d\tau \\ &\quad + 2 \int_{t_1}^{t_2} \int_0^{\frac{\pi}{2}} \lambda_z(\phi)^{-1} \sigma_{zz}^{(out,2)}(R_i + \tau) (R_i \cos \bar{\phi} - (R_i + \tau) \cos \phi) d\phi d\tau \end{aligned} \quad (\text{A.32})$$

where  $\sigma_{zz}^{(in,i)}$  is the axial stress in the inner isotropic layer with shear modulus  $\mu_i$ :

$$\sigma_{zz}^{(in,i)} = \lambda_z^2 \mu_i - \frac{\mu_i}{\lambda_z^2} \quad (\text{A.33})$$

and  $\sigma_{zz}^{(out,i)}$  is the axial stress in the outer anisotropic layer with shear modulus  $\mu_i$ :

$$\begin{aligned} \sigma_{zz}^{(out,i)} &= \lambda_z^2 \mu_i - \frac{\mu_i}{\lambda_z^2} + \frac{2}{\sqrt{I_4}} \left[ (-1 + \sqrt{I_4}) \lambda_z^2 \rho_1 \sin^2[\alpha] \right] \\ &\quad + \frac{2}{\sqrt{I_6}} \left[ (-1 + \sqrt{I_6}) \lambda_z^2 \rho_2 \sin^2[\alpha] \right] \end{aligned} \quad (\text{A.34})$$

The parameter  $t_1$  is the thickness of the inner isotropic layer ( $R_m - R_i$ ),  $t_2$  is the total wall thickness of the actuator ( $R_o - R_i$ ), and  $d\tau$  is the differential thickness of the actuator (Figure S9).

**Obtaining the relationship between input pressure and bend angle** Now solving  $M_{mat} = M_{cap}$  yields the relationship between input pressure and output bend angle:

$$\begin{aligned}
P = & \frac{\int_0^{t_1} \int_{\frac{\pi}{2}}^{\pi} \lambda_z^{-1} \sigma_{zz}^{(in,1)} (R_i + \tau) (R_i \cos \bar{\phi} - (R_i + \tau) \cos \phi) d\phi d\tau}{2R_i^2 \int_0^{\pi} \sin^2 \phi \text{abs} (R_i \cos \bar{\phi} - R_i \cos \phi) d\phi} \\
& + \frac{\int_{t_1}^{t_2} \int_{\frac{\pi}{2}}^{\pi} \lambda_z^{-1} \sigma_{zz}^{(out,1)} (R_i + \tau) (R_i \cos \bar{\phi} - (R_i + \tau) \cos \phi) d\phi d\tau}{2R_i^2 \int_0^{\pi} \sin^2 \phi \text{abs} (R_i \cos \bar{\phi} - R_i \cos \phi) d\phi} \\
& + \frac{\int_0^{t_1} \int_0^{\frac{\pi}{2}} \lambda_z^{-1} \sigma_{zz}^{(in,2)} (R_i + \tau) (R_i \cos \bar{\phi} - (R_i + \tau) \cos \phi) d\phi d\tau}{2R_i^2 \int_0^{\pi} \sin^2 \phi \text{abs} (R_i \cos \bar{\phi} - R_i \cos \phi) d\phi} \\
& + \frac{\int_{t_1}^{t_2} \int_0^{\frac{\pi}{2}} \lambda_z^{-1} \sigma_{zz}^{(out,2)} (R_i + \tau) (R_i \cos \bar{\phi} - (R_i + \tau) \cos \phi) d\phi d\tau}{2R_i^2 \int_0^{\pi} \sin^2 \phi \text{abs} (R_i \cos \bar{\phi} - R_i \cos \phi) d\phi}
\end{aligned} \tag{A.35}$$

**Locating the neutral bending axis** In the bending model, the parameter  $\bar{\phi}$  is the circumferential angle where the neutral bending axis is located. This parameter was determined using an FE simulation for an actuator with fiber angle  $\pm 5^\circ$ ,  $R_i = 6.35mm$ ,  $R_o = 8.35mm$ , and  $L = 160mm$ . We found the neutral bending axis occurs at  $\bar{\phi} = 35^\circ$ , as shown in Figure A.13A, where we plot the axial stretch along the line corresponding to  $\bar{\phi} = 35^\circ$ , and compare it to the maximum axial stretch (which occurs at  $\phi = 180^\circ$ ). To demonstrate that  $\bar{\phi}$  does not depend on the fiber angle, we also extracted the axial stretch at  $35^\circ$  for actuators with fiber angles  $\pm 15^\circ$  and  $\pm 25^\circ$  (Figure A.13B).

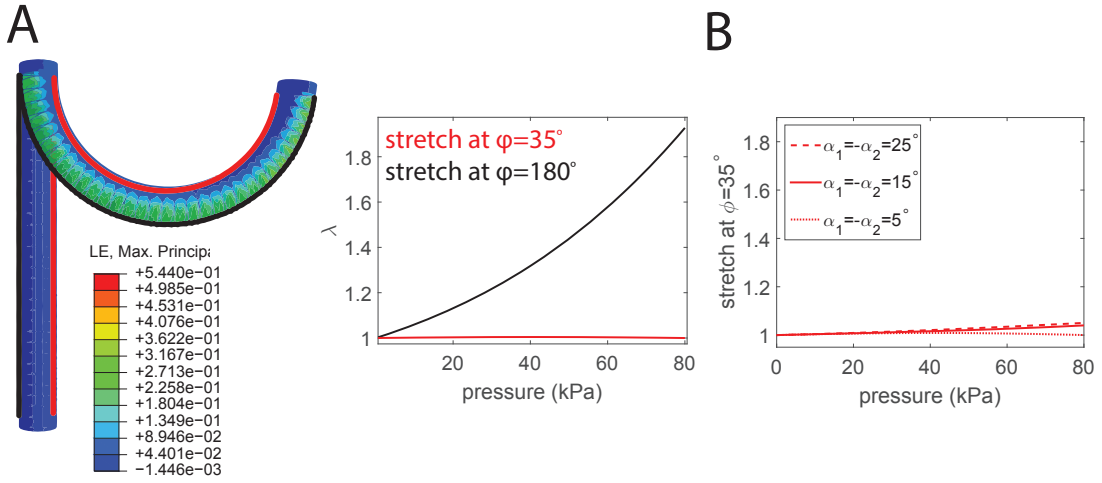


Figure A.13: (A) FEA results for a bending actuator with fiber angle  $\alpha = \pm 5^\circ$ , at  $P = 0kPa$  and  $P = 40kPa$ . The material line at  $\phi = 180^\circ$  is highlighted in black, and the line at  $\phi = 35^\circ$  is highlighted in red. The graph shows the corresponding axial stretches. We see that at  $\phi = 35^\circ$ , the actuator does not change in length. (B) Comparison of axial stretch at  $\phi = 35^\circ$  for bending actuators with fiber angles  $\alpha = \pm 5^\circ$ ,  $\alpha = \pm 15^\circ$  and  $\alpha = \pm 25^\circ$ . In each case, the stretch is almost unity, showing that we can use the line at  $\bar{\phi} = 35^\circ$  as the neutral axis.

**Verification of Bending Model** To verify the analytical bending model, we performed FE simulations and compared the results to the analytical predictions, as shown in Figure A.14. In each case (A-D), we used one FE simulation ( $\alpha = \pm 5^\circ$ ) to find the location of the neutral axis  $\bar{\phi}$ . For case A, the thickness of the outer layer,  $R_o - R_m$ , was a fitting parameter found using the extend/expand/twist model. For the other cases, this value was reduced in proportion to the wall thickness to outer radius ratio (e.g. in case B, the ratio was reduced to 0.66 of its initial value, so we also reduced the thickness of the outer layer by this amount).

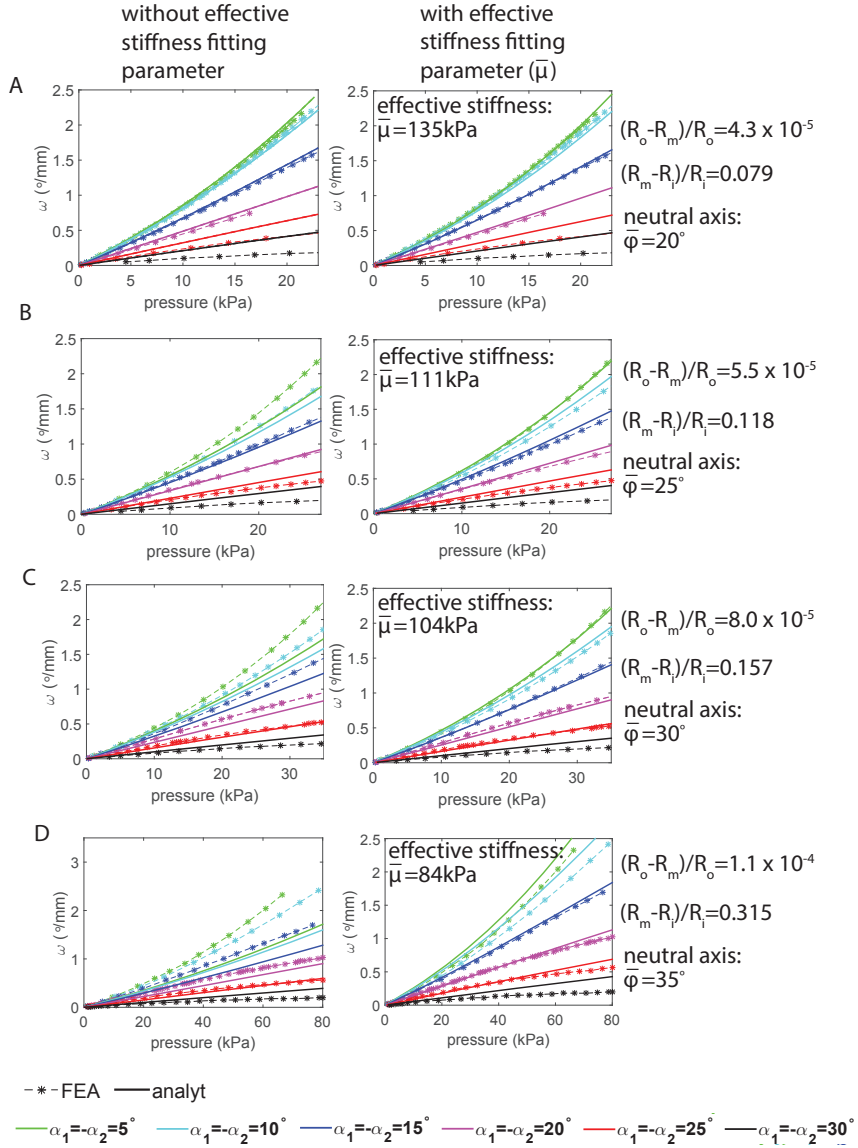


Figure A.14: Comparing analytical results to FEA results for various different wall thickness to radius ratios. The column on the left shows results obtained from the model using the experimentally measured moduli, while the column on the right shows results obtained using an effective modulus  $\bar{\mu}$  (fitted using an FE simulation). As the wall thickness to radius ratio decreases (going from A to D), the analytical model becomes much more accurate. In case D, we see that the ratio is small enough that there is no need to use an effective stiffness, as it gives the same results as using the experimentally measured moduli (i.e. for case D, the graphs in the left and right columns are the same).

When deriving the bending model, we assumed that the actuator walls were thin. As a result, for thicker walled actuators, the model yields lower than expected bend angles at any given pressure, because the actuators are too stiff. This can be seen in the left column of Figure A.14, which compares analytical and FE results for actuators with various different ratios of wall thickness to



outer radius. We see that as the thickness to radius ratio decreases, the model gives more accurate results.

In order to use the model for actuators with higher thickness to radius ratios, we use an effective shear modulus in the model, rather than using the experimentally measured moduli. This is illustrated in the right column of Figure A.14. One FE simulation ( $\alpha = \pm 5^\circ$ ) is used to find the effective shear modulus. Using this fitting parameter (from just one simulation), we can quite accurately predict the deformation for other fiber angles. As the ratio decreases, we see that there is no need to use this fitting parameter, since in case D, it gives almost identical results to when the experimentally measured shear moduli are used.

To experimentally verify the bending model, we fabricated and tested bending actuators with fiber angles ranging from  $\pm 5^\circ$  to  $\pm 30^\circ$ . The actuators had inner radius  $R_i = 6.35mm$ , wall thickness  $R_o - R_i = 2mm$ , and length  $L = 160mm$ . Using  $R_m = 8.89 \times 10^{-4}mm$  and effective shear modulus  $\bar{\mu} = 78kPa$ , we found good agreement between the analytical model and the experimental results (Figure S12).

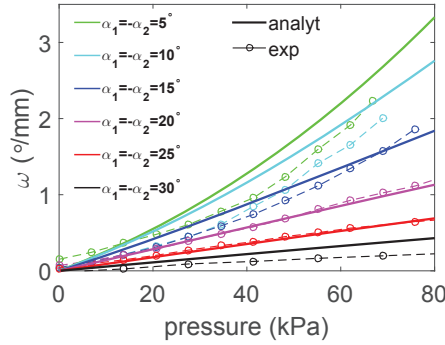


Figure A.15: Comparison of experimental results and analytical predictions of bend angle per unit length for actuators with fiber angles ranging from  $\pm 5^\circ$  to  $\pm 30^\circ$

## A.5 Replicating finger motion

In this section, we describe the procedure for gathering and processing the data describing the kinematics of the fingers. We then describe the steps in the optimization algorithm which is used to determine the optimal design parameters for an actuator which, upon pressurization, will replicate the motion of the fingers. We use the optimization algorithm to design actuators which replicate the motion of the index finger and the thumb, and verify the results using finite element analysis. Fi-

nally, we outline the experimental procedure for determining the motion of an actuator in 3d space. Note that the Matlab scripts corresponding to this section can be found on [softroboticstoolkit.com](http://softroboticstoolkit.com).

### A.5.1 Processing the input data

We use electromagnetic (EM) trackers to record the coordinates of the index finger and thumb as they bend. The location of the EM trackers on the hand is illustrated in Figure A.16A. The lengths of each of the links and the angles between the links are plotted as a function of time in Figure A.17 (index finger) and Figure A.18 (thumb).

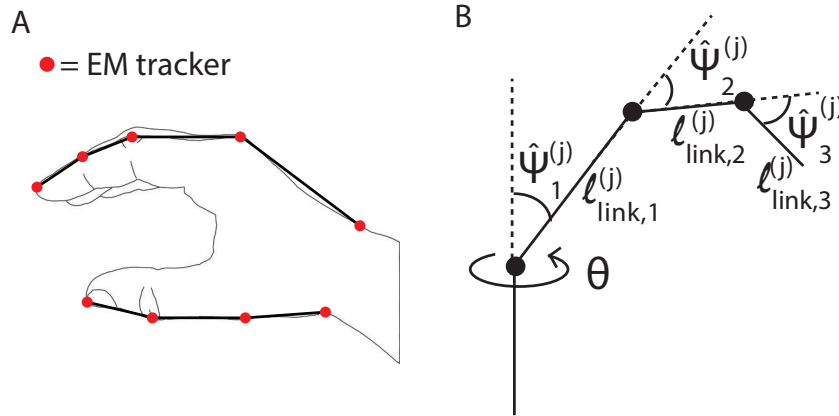


Figure A.16: (A) Location of the EM trackers on the index finger and thumb (B) The link lengths  $l_{link,i}$  are the lengths between the joints of the finger, while the bend angles  $\hat{\psi}_i$  are the angles between adjacent links, as illustrated above.

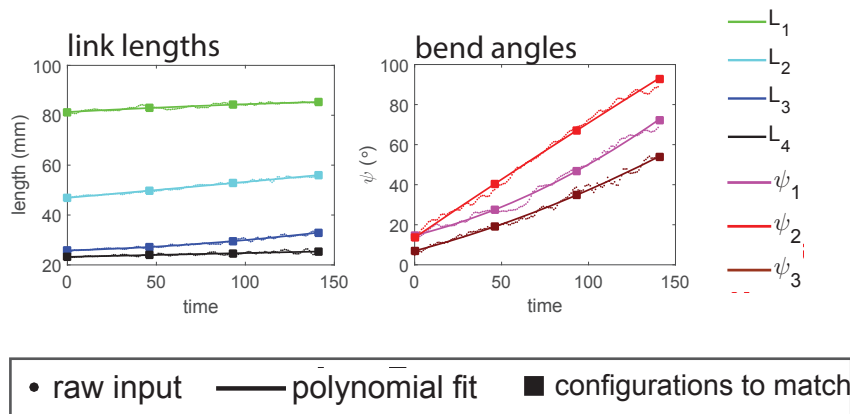


Figure A.17: Index finger EM tracker data: The dots represent the raw input. This is smoothed using a Savitzky-Golay filter in Matlab, and the smoothed data are plotted as solid lines. Solid squares denote the four configurations which are selected to be replicated.

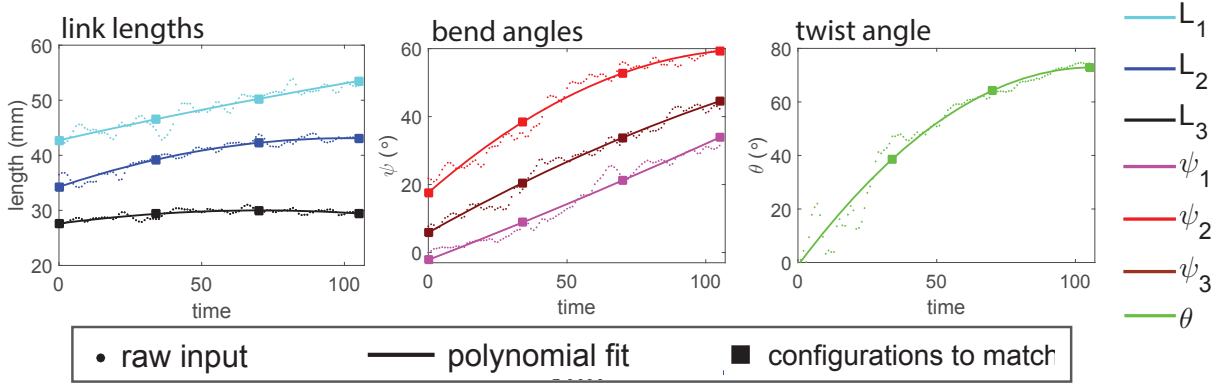


Figure A.18: Thumb EM tracker data: The dots represent the raw input. This is smoothed using a Savitzky-Golay filter in Matlab, and the smoothed data are plotted as solid lines. Solid squares denote the four configurations which are selected to be replicated.

### A.5.2 Optimization

We want the optimization to output (1) the fiber angle  $\alpha_i$  for each segment (2) the initial length  $l_{bend,i}^{(0)}$  of each of the bending segments and (3) the pressures  $P^{(j)}$  at which the input configurations will occur i.e. we want to find the values of the variables  $\alpha_i$ ,  $l_{bend,i}^{(0)}$  and  $P^{(j)}$  which will achieve the desired link lengths and bend angles. For the initial values of the variables, we choose pressures equally spaced between the minimum pressure ( $0kPa$ ) and maximum pressure ( $80kPa$ ), and since we want the bend and twist segment lengths to be as short as possible, we set  $\alpha_i$  and  $l_{bend,i}^{(0)}$  to their minimum allowed values  $\alpha_i = \alpha_{min} = 5^\circ$ ,  $l_{bend,i}^{(0)} = L_{min} = 10mm$ .

The maximum allowed bend segment length was chosen by doing some preliminary calculations: The maximum bend angle required for the index finger was  $93^\circ$ , and the bend angle per unit length for an actuator with fiber angle  $5^\circ$  at the maximum allowed pressure  $P_{max} = 80kPa$  is  $3.3^\circ/mm$ . Dividing the maximum required bend angle by the maximum possible bend per unit length gave a segment length of  $28mm$ . This was rounded up to give a maximum allowed segment length of  $30mm$ . The main steps in the optimization are as follows:

#### Step 1

- Given the fiber angle  $\alpha$  for each segment and bending and twisting segment lengths, calculate the initial lengths of the extending segments, as shown in Figure 4 (for example,  $\hat{l}_{ext,2}^{(0)} = l_{link,2}^{(0)} - \frac{l_{bend,2}^{(0)}}{2} - \frac{l_{bend,4}^{(0)}}{2}$ ).

- Calculate the extension of the bending segments in each configuration (for example,  $l_{bend,2}^{(j)} = l_{bend,2}^{(0)} + R_i \psi_2^{(j)} (\cos \bar{\phi} + 1)$ , where  $R_i$  is the inner radius of the actuator).
- Use the bend segment lengths in each configuration and the overall link lengths in each configuration to calculate the required length of each of the extending segments in each configuration (for example,  $\hat{l}_{ext,2}^{(j)} = l_{link,2}^{(j)} - \frac{l_{bend,2}^{(j)}}{2} - \frac{l_{bend,4}^{(j)}}{2}$ ).

### Step 2

- For each extending (or twisting) segment, given the fiber angle  $\alpha_i$ , use the analytical model to solve for the segment length  $\hat{l}$  (or twist  $\hat{\theta}$ ) at each pressure  $P^{(j)}$ .
- The bending model is an inverse model (given a bend angle, it outputs the pressure at which that bend angle is achieved). So, for each bending segment, given the fiber angle  $\alpha_i$ , use the analytical model to find the pressures  $\hat{P}^{(j)}$  at which the required bend angles  $\psi$  are achieved.

**Step 3** The function to be minimized is

$$\begin{aligned}
 f = & c_1 \sum_{j=1}^N \sum_{i=1}^{n_{tw}} \left| \theta_i^{(j)} - \hat{\theta}_i^{(j)} \right|^2 + \sum_{j=1}^N \sum_{i=1}^{n_{ext}} \left| l_{ext,i}^{(j)} - \hat{l}_{ext,i}^{(j)} \right|^2 \\
 & + c_2 \sum_{j=1}^N \sum_{i=1}^{n_{bend}} \left| P_i^{(j)} - \hat{P}^{(j)} \right|^2,
 \end{aligned} \tag{A.36}$$

where  $n_{tw}$ ,  $n_{ext}$  and  $n_{bend}$  are the total number of twisting, extending, and bending segments, respectively, and  $N$  is the number of goal configurations. If  $f$  is not sufficiently small,  $x$  is updated and the steps are repeated. When the minimum value of  $f$  is found, the fiber angles, segment lengths, and pressures are output.

### A.5.3 Glove

In Chapter 4, we used the optimization algorithm to design an actuator where the *top* of the actuator mimics the input motion. Here, we use the algorithm to design an actuator where the *bottom* of the actuator mimics the input motion. This could be used to design an actuator for use in an assistive glove, for example.[28] We follow the same procedure as before. The twist and bend

angles to be matched are the same as in Chapter 4, but now the link lengths should be matched by the bottom edge of the actuator.

**Index finger** For the index finger, the optimization determined that the actuator should have extending segments 1, 3, and 6, with lengths 70mm, 21mm, and 16mm respectively, and fiber angles  $\pm 33^\circ$ ,  $\pm 15^\circ$ , and  $\pm 27^\circ$  respectively, and bending segments 2, 4, and 5 with lengths 23mm, 28mm, and 15mm respectively, and fiber angles  $\pm 8.1^\circ$ ,  $\pm 5^\circ$ , and  $\pm 5^\circ$  respectively. We used FEA to investigate the response of an actuator with this design, and we see in Figure A.19 that the FE results are in good agreement with the analytical prediction.

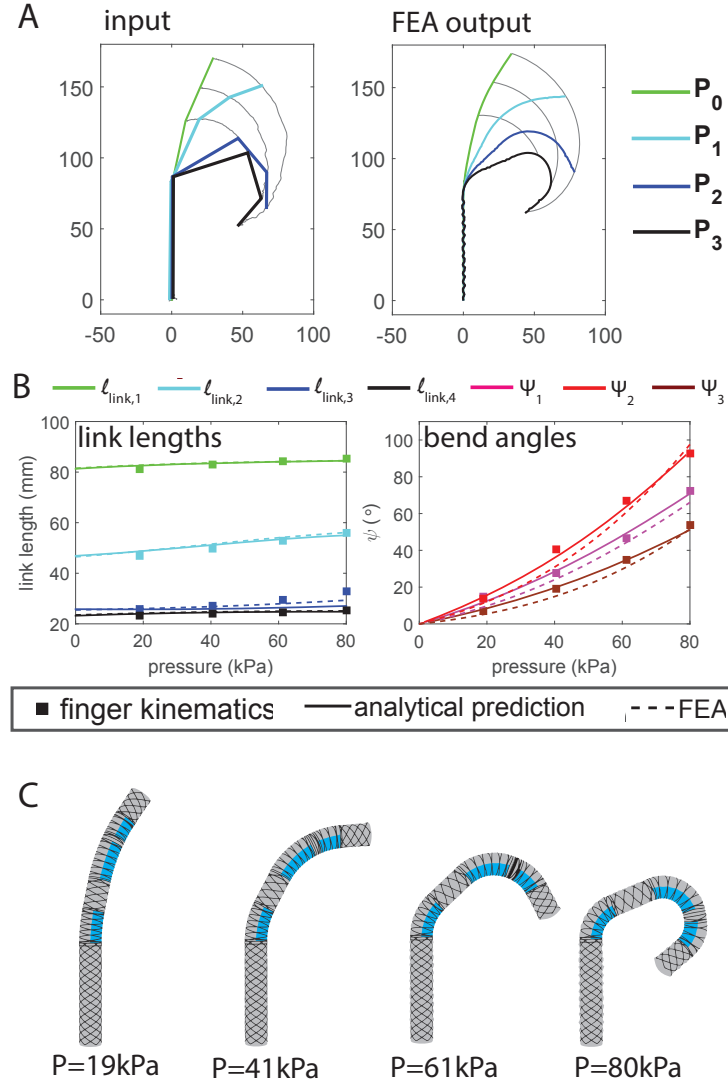


Figure A.19: (A) Desired input configurations (left) and achieved FEA output configurations (right) (B) Comparing the input configurations, analytical prediction, and FEA output for each link length and bend angle (C) FEA results for each of the four configurations

**Thumb** As a second example, we consider the motion of the thumb. This time the optimization determines that the actuator should have a twisting segment 1 with length 24mm and fiber angle  $5^\circ$ , extending segments 3, 5, and 7, with lengths 21mm, 9mm, and 17mm respectively and fiber angles  $\pm 8^\circ$ ,  $\pm 5^\circ$ , and  $\pm 25^\circ$  respectively, and bending segments 2, 4, and 6, with lengths 14mm, 30mm, and 21mm respectively, each with fiber angle  $\pm 5^\circ$ . Again, we use FEA to analyze the result, and Figure A.20 shows that the FE results and the analytical prediction match closely.

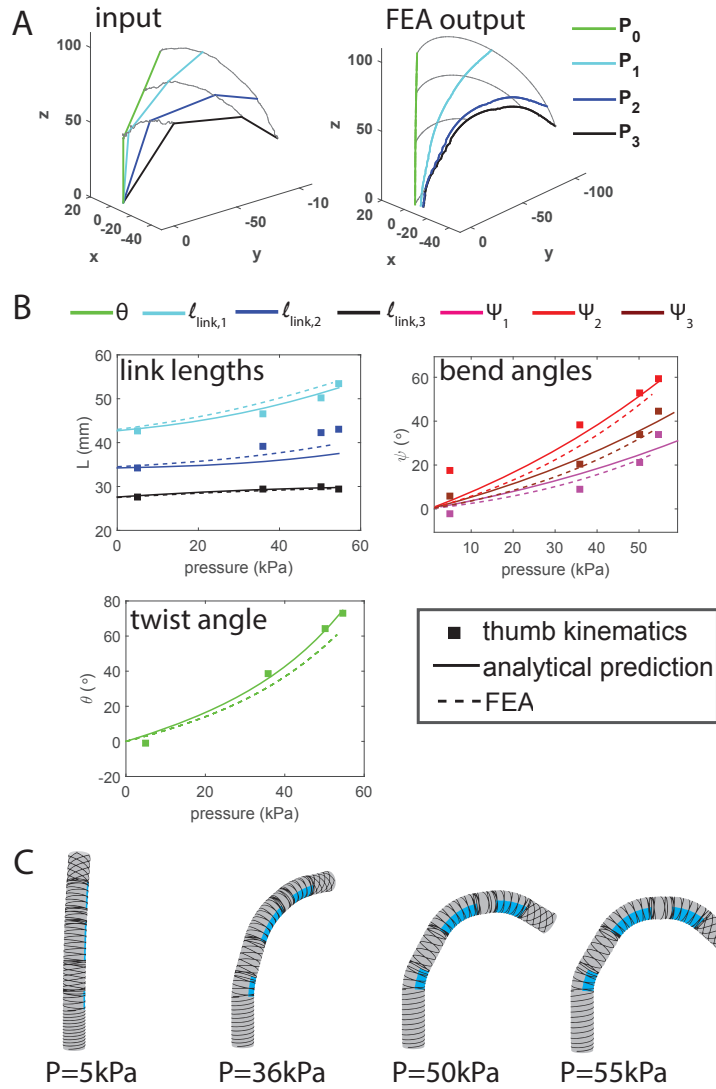


Figure A.20: (A) Desired input configurations (left) and achieved FEA output configurations (right) (B) Comparing the input configurations, analytical prediction, and FEA output for each link length and bend angle, and for the twist angle (C) FEA results for each of the four configurations

#### A.5.4 Thumb actuator: reconstructing 3d motion

Here we describe our procedure for recording the motion of the thumb actuator. Since the thumb actuator moves out of plane, tracking its motion is slightly more complex than in the case of the finger actuator. In previous cases, we took a photograph of the actuator at each pressure increment. Now, at each pressure increment, we take photographs of the actuator from two perspectives, using cameras positioned at right angles to one another (Figure A.21A,C). We post-process the photographs by using Matlab to track the left and right edges of the actuator in each picture. We then find the center line of the actuator by calculating the average of the left and right sides (Figure A.21B,D). Finally, we interpolate the center line, so that the front view and the side view are sampled at identical  $z$  values. We can then combine the  $x - z$  data and the  $y - z$  data to find the  $x - y - z$  data (Figure A.21E).



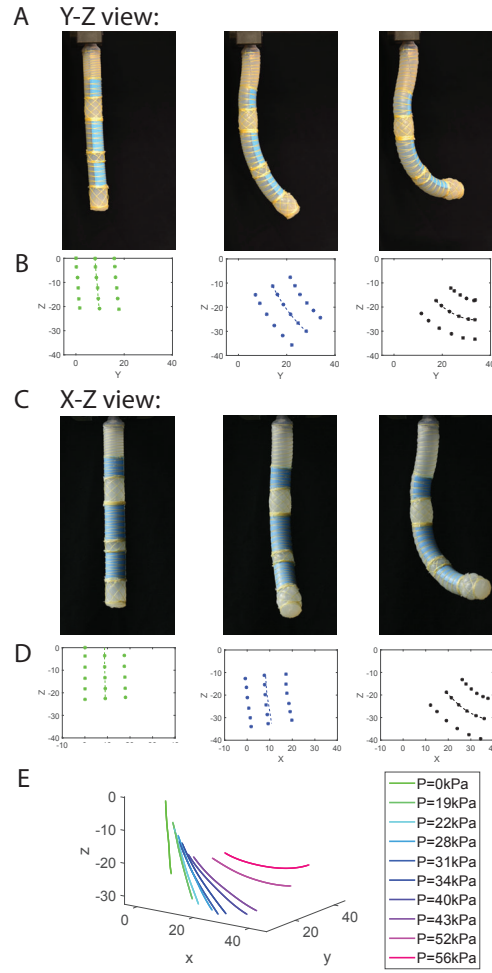


Figure A.21: Reconstructing the motion of segment 6 of the thumb actuator: (A) Front view of the actuator at 3 different actuation pressures (B) Points on either side of the actuator are tracked in Matlab, and used to find the center line (C) Side view of the actuator at 3 different actuation pressures (D) Points on either side of the actuator are tracked in Matlab, and used to find the center line (E)  $X$ - $Y$  and  $Y$ - $Z$  values are combined to find the configurations in  $X$ - $Y$ - $Z$

## B Supporting Information for Chapter 5

### B.1 Textile Characterization and Modeling

In this section we first describe our experimental procedures for characterizing textile behavior and present the collected results. Then, we describe the procedure for identifying an appropriate continuum constitutive model for the textiles.

#### B.1.1 Mechanical testing

To characterize the mechanical properties of the textiles, we conducted uniaxial and biaxial tension tests.

**Uniaxial tensile testing.** The uniaxial tensile tests were conducted on a single-axis Instron (model 5566; Instron, Inc.) using pneumatic grips and a 10kN load cell. All specimens were rectangular with width  $W = 50$  mm, length 200 mm and thickness  $T = 0.6$  mm. A gauge length of  $L = 75$  mm was used, and the specimens were tested by stretching them along the wale direction (a wale being a column of loops knitted by a single needle) and the course direction (perpendicular to the wale) – see Figure B.1a.

Three different sets of specimens of the high stretch textile (24710, Darlington Fabrics) and the low stretch textile (26210, Darlington Fabrics) were considered: (i) uncoated (Figure B.1b,c), (ii) coated with the air-impermeable film (3918, Bemis Company, Inc - Figure B.1d,e), and (iii) coated with the rigid film (4220, Bemis Company, Inc - Figure B.1f,g).

In Figure B.1b-g, we report the experimental stress-stretch curves. Note that the stretch  $\lambda$  is calculated from the extension ( $\Delta u$ ) applied by the Instron as

$$\lambda = \frac{L + \Delta u}{L}, \quad (\text{B.1})$$

while the Cauchy stress  $\sigma$  is obtained from the force  $F$  measured by the Instron as

$$\sigma = \frac{F}{wt}, \quad (\text{B.2})$$

where  $L$  is the initial gauge length of the sample and  $w = \lambda^{-\frac{1}{2}}W$  and  $t = \lambda^{-\frac{1}{2}}T$  are its current

width and thickness (assuming that the material is incompressible – see Section C.1.2).

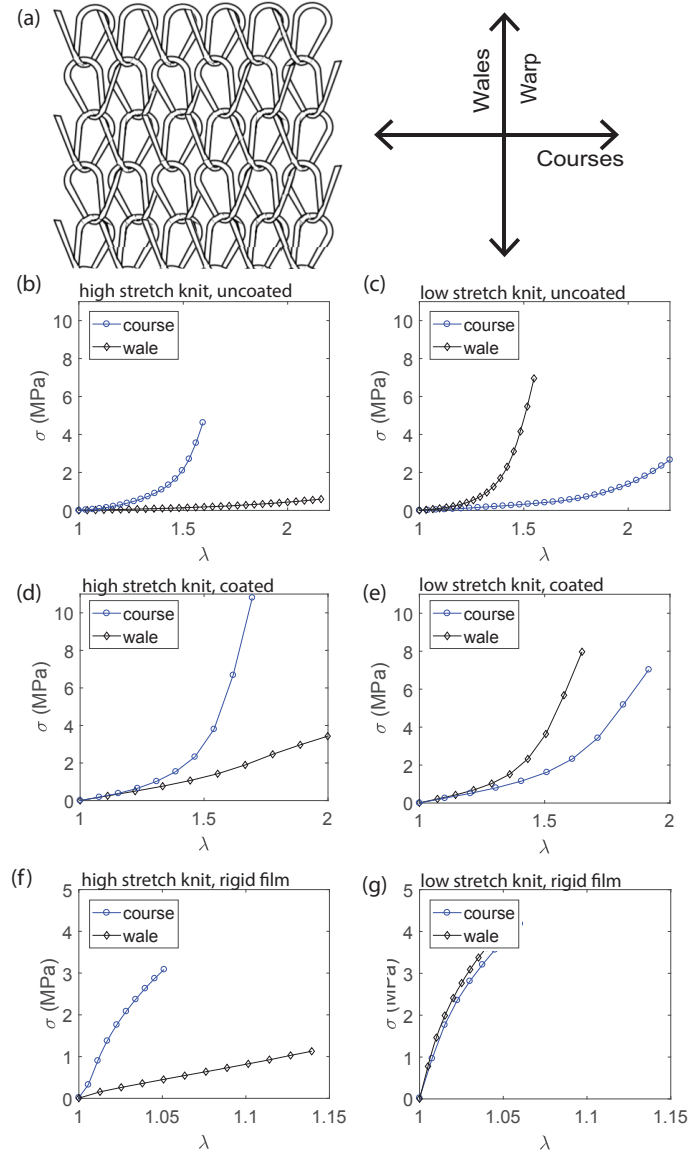


Figure B.1: (a) A schematic of a sample warp knit. The warp refers to the direction of manufacturing of the knit. The ‘wales’ refer to the loops parallel to this warp direction, while the ‘courses’ are the perpendicular loops. (b,c) Uniaxial tensile test results for the high stretch knit and low stretch knit in the uncoated state (d,e) Uniaxial tensile test results for the high stretch knit and low stretch knit coated with the air-impermeable film (f,g) Uniaxial tensile test results for the high stretch knit and low stretch knit coated with the rigid film

We find that for the uncoated case the high stretch knit is much stiffer in the course direction (see Figure B.1b), while for the low stretch knit the wale direction is much stiffer than the other (see Figure B.1c). Coating with the air-impermeable film increases the stiffness slightly overall, but

preserves the anisotropic properties of the textiles and preserves the difference in behavior between the two textiles (see Figures B.1d and e). Finally, coating with the rigid film increases the stiffness significantly in all cases (see Figures B.1f and g).

**Biaxial tensile testing.** The biaxial tensile tests were conducted using a custom-made setup consisting of four motorized linear translation stages (LTS300, Thorlabs, Inc.) controlled using Matlab (Mathworks, Inc). The specimens were attached to the stages via 3d printed grips (printed on an Objet Connex 500 printer – Stratasys) and two of the grips were attached to load cells (LSB200, 50lb capacity, FUTEK Advanced Sensor Technology, Inc.), which measured the force continuously as the specimen was deformed.

We used cruciform specimens, where the cruciform shape was aligned with the course and wale directions of the textile. The specimens had arm length 60 mm and arm width 20 mm and we marked a square gauge region with edges  $L = 10$  mm in the center of the specimen (dashed lines in Figure B.2a). To ensure that the displacement of the stages resulted in straining of the gauge region, rather than straining of the specimen arms, the arms were reinforced by applying a layer of rigid film (4220, Bemis Company, Inc).

To characterize the deformation of the gauge region as the specimen was stretched, we recorded images using a webcam (Logitech Webcam 300) and then extracted the length of the gauge region in the course ( $l_c$ ) and wale ( $l_w$ ) directions. The stretch in the course direction  $\lambda_c$  and the stretch in the wale direction  $\lambda_w$  were then calculated as

$$\lambda_c = \frac{l_c}{L}, \quad \lambda_w = \frac{l_w}{L}. \quad (\text{B.3})$$

Finally, we use the loads  $F_c$  and  $F_w$  measured by the load cells along the course and wale directions, respectively, to calculate the Cauchy stresses in the gauge region as

$$\sigma_c = \lambda_c \frac{F_c}{2LT}, \quad \sigma_w = \lambda_w \frac{F_w}{2LT} \quad (\text{B.4})$$

where  $T = 0.6$  mm is the initial thickness of the samples, and the factor 2 is introduced because the width of the gauge square is half the width of the specimen arm.

We performed equibiaxial tests on each textile coated with the air-impermeable film. In Figure

B.2b, we see that the high stretch knit is stiffer in the course direction than in the wale direction, as observed in the uniaxial tests. However, while in the uniaxial tests we observed a very large difference in stiffness between the course and wale directions, here the difference is less pronounced. For the low stretch knit, we see in Figure B.2c that the textile behaves similarly in each direction. This contrasts with the uniaxial tests, where the wale direction was much stiffer than the course. Finally, we performed an additional biaxial test on each textile, where we applied a greater displacement to the specimen in the compliant direction than in the stiff direction. The results are shown in Figure B.2d,e and will be used to validate our constitutive model in the next section.

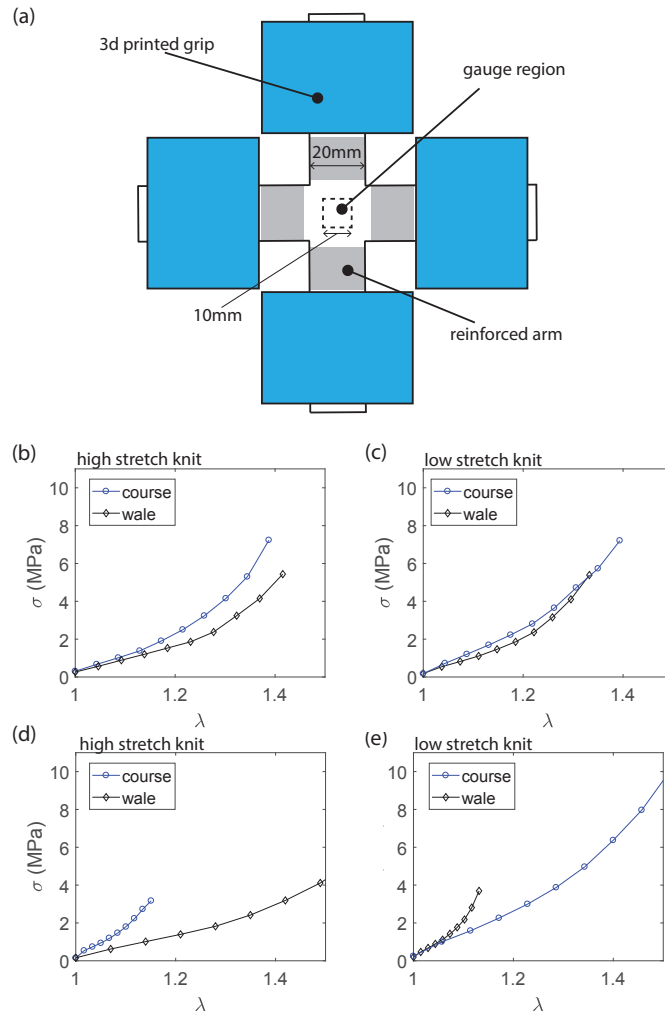


Figure B.2: (a) Schematic of a cruciform specimen. (b,c) Equibiaxial test results for high stretch knit and low stretch knit. (d,e) Biaxial test results for high stretch knit and low stretch knit - here, a higher displacement was applied to the textiles in their most compliant direction (as identified from the uniaxial tests).

### B.1.2 Modeling

From the uniaxial and biaxial experimental results on the coated textiles, we see that each textile has one direction which is much stiffer than the other. To capture this behavior, we used the Holzapfel-Gasser-Ogden continuum model [65], which is defined by the strain energy density

$$W = C_{10}(\bar{I}_1 - 3) + \frac{K}{2} \left( \frac{J^2 - 1}{2} - \ln J \right) + \frac{k_1}{2k_2} \sum_{\alpha=1}^N \left( e^{k_2 \bar{E}_\alpha^2} - 1 \right), \quad (\text{B.5})$$

with

$$\bar{E}_\alpha = \kappa(\bar{I}_1 - 3) + (1 - 3\kappa)(\bar{I}_{4(\alpha\alpha)} - 1). \quad (\text{B.6})$$

Here,  $N$  is the number of families of fibers and  $C_{10}$ ,  $k_1$ ,  $k_2$ ,  $K$  and  $\kappa$  are material parameters.  $K$  is the initial bulk modulus of the material, while  $\kappa$  ( $0 \leq \kappa \leq 1/3$ ) describes the level of dispersion in the fiber directions. Since in our textiles we have one characteristic orientation ( $N = 1$ ) and all ‘fibers’ being perfectly aligned, we have  $\kappa = 0$  and the strain energy given in Eq. (B.5) reduces to

$$W = C_{10}(\bar{I}_1 - 3) + \frac{K}{2} \left( \frac{J^2 - 1}{2} - \ln J \right) + \frac{k_1}{2k_2} \left( e^{k_2(\bar{I}_4 - 1)^2} - 1 \right), \quad (\text{B.7})$$

where  $J = \det \mathbf{F}$ ,  $\bar{I}_1 = J^{-2/3} \text{tr}(\mathbf{F}^T \mathbf{F})$  and  $\bar{I}_4 = J^{-2/3} \mathbf{M} \cdot (\mathbf{F}^T \mathbf{F}) \cdot \mathbf{M}$ ,  $\mathbf{F}$  being the deformation gradient and  $\mathbf{M}$  denoting the characteristic orientation (stiffest direction) of the textile.

To identify appropriate material parameters for each of the textiles, we performed finite element analysis using Abaqus (SIMULIA, Providence RI). This allowed us to fully account for boundary effects and stress inhomogeneities in the specimens. All models were generated using shell elements (S4R) and had geometry identical to that of the experimentally tested specimens. We performed quasi-static nonlinear analysis using Abaqus/Standard to simulate both uniaxial and biaxial tests. We extracted the stretch from the simulations using the same procedure as for the experiments. In the simulations we observed that the stress state was uniform within the gauge region, so we extracted the stress directly from the simulation output database. We then compared the stress-stretch relationships from the simulations to the relationships from the experiments. We repeated the simulations adjusting the material parameters  $C_{10}$ ,  $k_1$ ,  $k_2$  each time until we found the best match to the experimental results, for all stress-stretch curves (see Figure B.3c-h). We also adjusted the

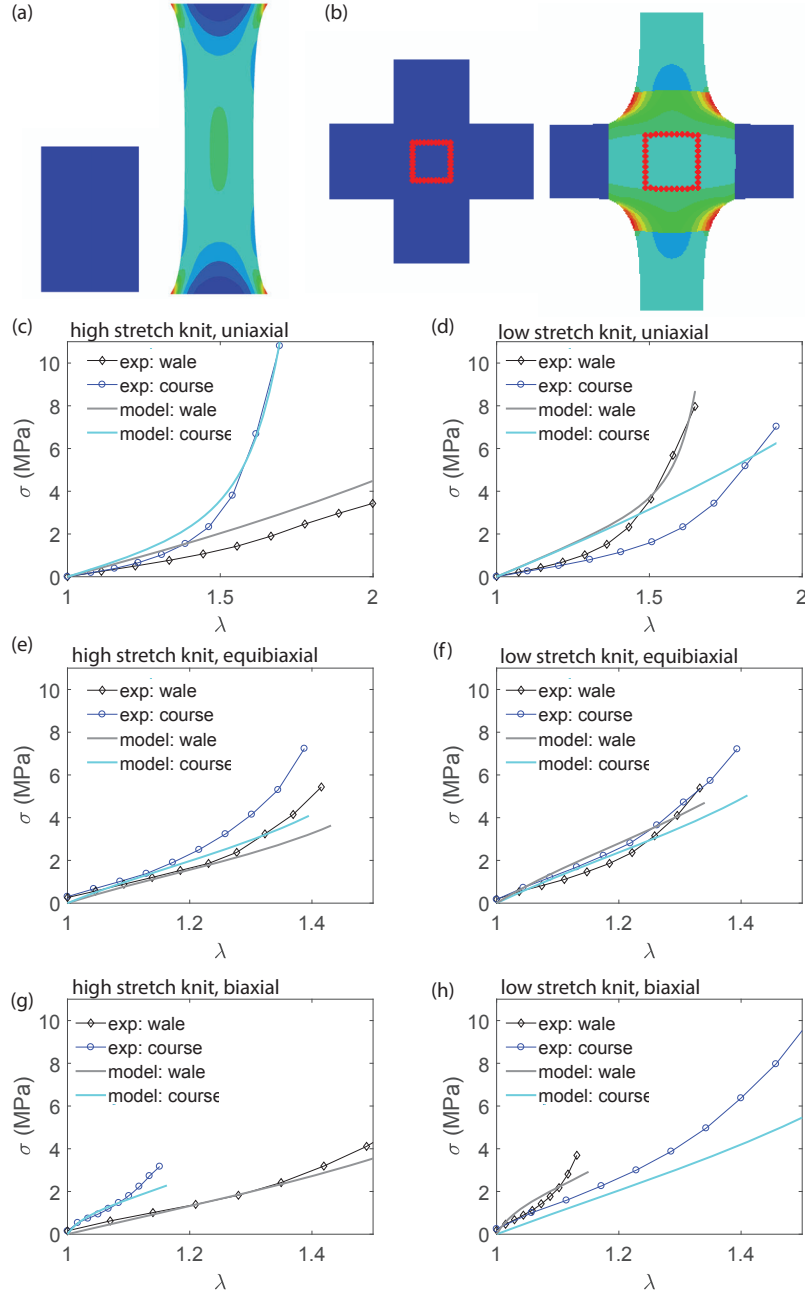


Figure B.3: (a) Sample FEA results for a uniaxial test, showing the sample in its initial and deformed configurations. (b) Sample FEA results for a biaxial test, showing the sample in its initial and deformed configurations. (c,d) Comparison of experimental and numerical results for uniaxial tests (e,f) Comparison of experimental and numerical results for equibiaxial tests (g,h) Comparison of experimental and numerical results for biaxial tests

value of the Poisson's ratio  $\nu = \frac{3K-4C_{10}}{2(3K+2C_{10})}$  to find the best fit for the deformation of the central region under uniaxial loading (see Figure B.4c,d). For the high stretch knit, we found that the

response is best captured using  $C = 0.64$  MPa,  $k_1 = 0.12$  MPa,  $k_2 = 0.52$ , and  $\nu = 0.49$ , while for the low stretch knit, we found  $C = 0.99$  MPa,  $k_1 = 0.017$  MPa,  $k_2 = 1.1$  and  $\nu = 0.49$ .

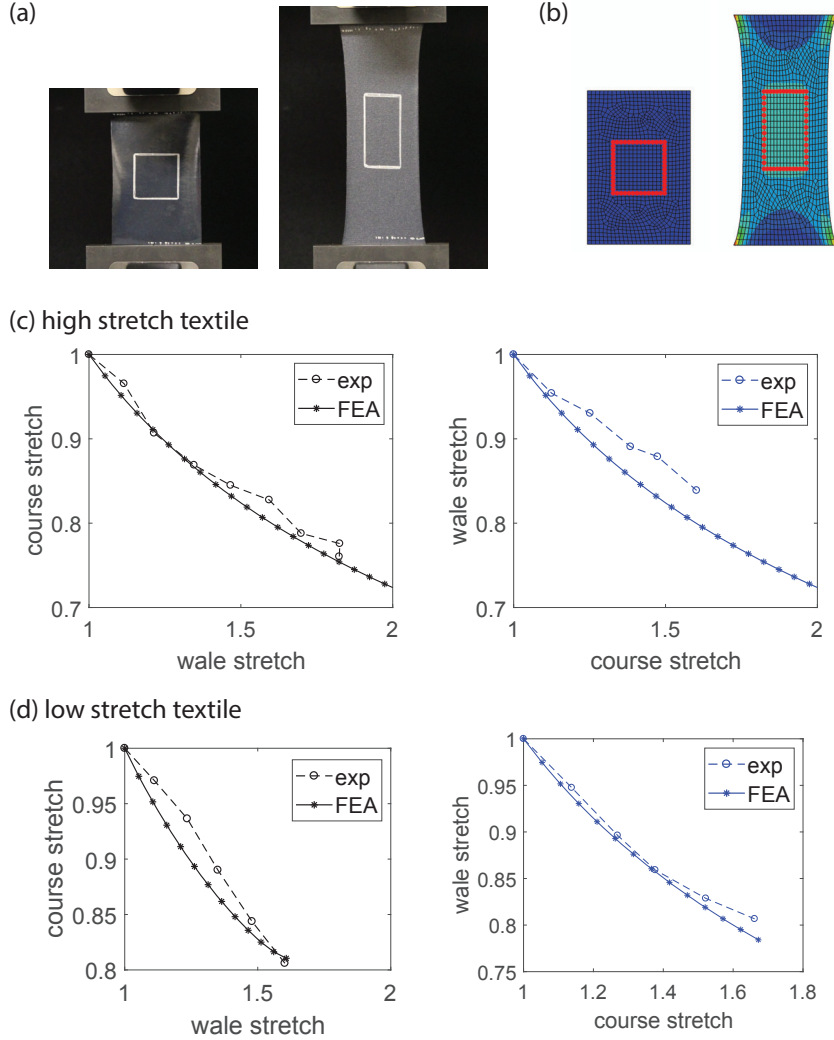


Figure B.4: (a) High stretch textile coated with air-impermeable film pictured in the relaxed and stretched configurations. (b) Snapshots of the relaxed and stretched configurations from finite element simulations of the high stretch textile coated with air-impermeable film. (c,d) A comparison of experimental stretch ratios in the course and wale directions with the ratios from finite element simulations

## B.2 Actuator Fabrication

To fabricate a textile actuator, we must first make the textiles air-impermeable. This can be achieved either by coating [108, 109] or by inserting a balloon into the textile pocket [110, 98]. Here, we choose to coat the textiles, as the coating has a dual functionality - making the textile



impermeable to air, and enabling us to bond textiles together without sewing. Note that we want the coating (i) to preserve the anisotropic properties of the textiles and does not overly inhibit their extensibility (see Figure B.3a,b) and (ii) to be quick and easy to be applied to the textile. Taking these two requirements into consideration, we chose to use a thermoplastic polyurethane film (3918, Bemis Company, Inc.), which exhibits 100% recovery after 100% elongation.

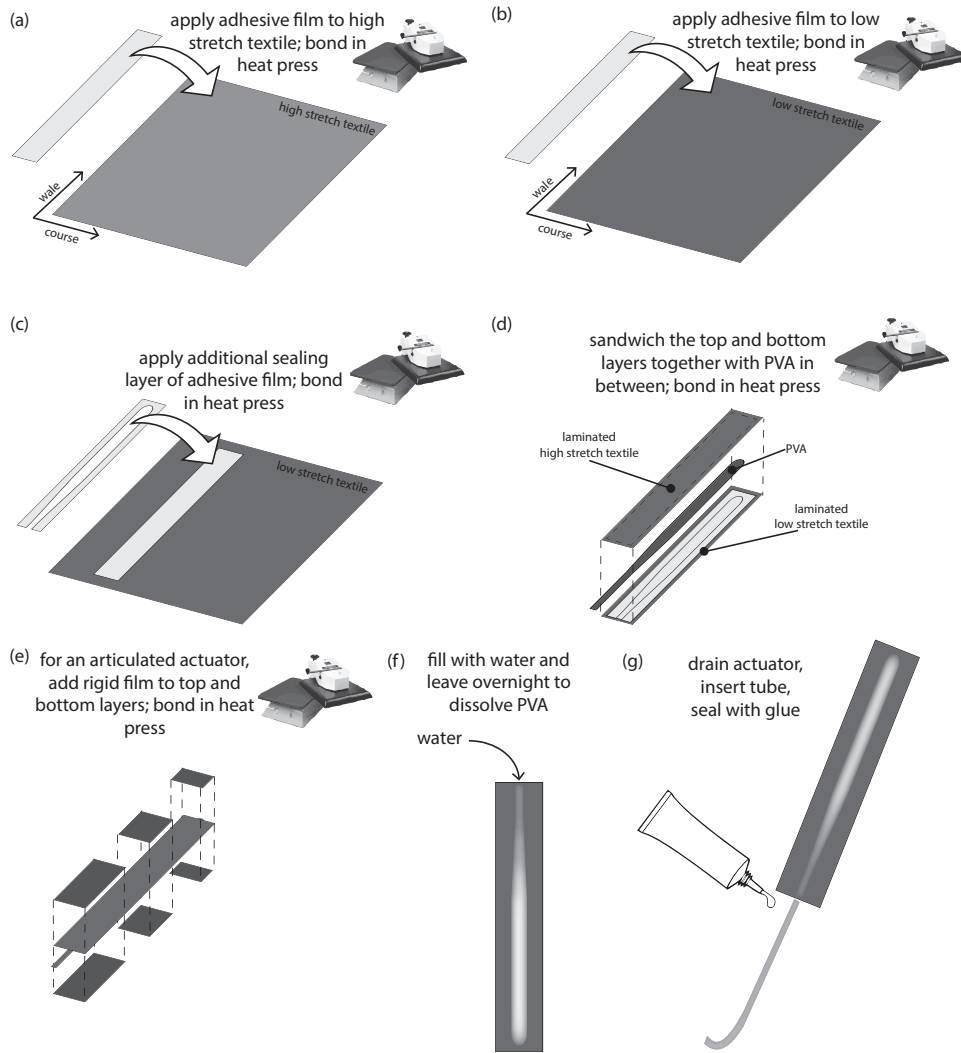


Figure B.5: Fabrication of sew-free actuators

The fabrication of our textile-based actuators consists of seven steps.

- (a) Using a Versa Laser, we cut the thermoplastic polyurethane film to the required shape of the actuator. For example, to create an actuator with initial air chamber width 15 mm, we cut

a rectangle of film of width 29 mm, which allows for a 7 mm seal around the actuator. We then adhere the film to the textile by placing the film on top of the textile and using a heat press (Digital Knight DK20S) to apply heat and pressure (340° F at 60 psi, as recommended by the film manufacturer) for 75 s (Figure B.5a,b). Finally, we rotate the textile and film 90° and apply the same heat and pressure again, to ensure a good bond.

- (b) We repeat this procedure for the low-stretch textile.
- (c) To ensure a strong seal when the top and bottom layers are bonded together, we add an extra layer of film around the edge of the actuator (Figure B.5c). This layer is adhered to the laminated textile using a heat press at 340° F and 60 psi. We apply heat and pressure for 75s, rotate the textile 90°, and apply heat and pressure for another 75s.
- (d) As well as making the textiles air-impermeable, the film enables us to heat seal the top and bottom layers of the actuator together. To stop the actuator chamber from sealing up, we need a material in the center which will not adhere to the film upon heating and which can easily be removed from the actuator at the end of the fabrication process. For this purpose, we choose a polyvinyl alcohol (PVA, Sulky Ultra Solvy Stabilizer). This does not adhere to the Bemis film, and it is water-soluble so it can simply be rinsed out of the actuator. The PVA is cut to the required width of the actuator chamber, and tapered at one end to the size of the tube which will be inserted later. We sandwich the PVA between the top and bottom layers, and seal using heat and pressure (Figure B.5d).
- (e) As well as using films for air-impermeability and to allow for sealing, we can use them to change the properties of the textile. For example, if we apply a polyamide film (4220, Bemis Company, Inc.), it restricts the deformation of the textile (Figure B.5e). Thus we can expand the design space of our actuators, since we can apply film in patterns to make actuators which deform into complex shapes upon pressurization (Figure 5.1d).
- (f) We leave the newly formed textile pocket to cool overnight. The next day we fill it with water, clamp it at the top, and leave it for a few hours to allow the PVA to dissolve (Figure B.5f). We then rinse it out and leave it to dry.

(g) Lastly we insert tubing at the open end of the actuator, and seal around the tubing using Loctite Flexible Adhesive for Vinyl, Fabric, and Plastic (Figure B.5g).

### B.3 Testing the actuators

All actuators were inflated to various different pressures using a pressure regulator (ER1-04-P000, Wilkerson Corporation) controlled through a dedicated graphical user interface written in LabView (LabView 2012, National Instruments). The actuators were secured by threading them through a 3d-printed fixture (see Figure B.6). The pressure value was read from a pressure gauge (BSP B010-EV002-A00A0B-S4, Balluff).

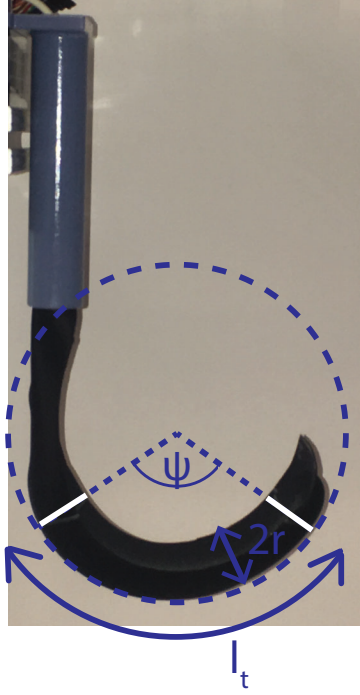


Figure B.6: An actuator of width  $20mm$  inflated to a pressure of  $141kPa$ . The section of interest has radius  $r$ , length  $l_t$ , and bend angle  $\psi$ .

To quantify the deformation of the actuators during inflation, we use a camera (Canon EOS Rebel T5i) and take photos of the actuators at various different inflation pressures. A sample photo is shown in Figure B.6. To remove end effects, we quantify the deformation of the part of the actuator between the white lines only (these lines mark the beginning of the taper at the proximal end of the actuator, and the rounded region at the distal end). We post-process the photos in

Matlab. We extract the radial stretch by monitoring the length of the white lines. We use edge detection to identify the outer edge of the actuator of length  $l_t$ . We then find the circle with radius  $\rho$  of best fit to this edge and calculate the bend angle per unit length as (Figure B.6)

$$\psi = \frac{l_t}{\rho_t} \quad (\text{B.8})$$

#### B.4 Actuator Modeling

To rapidly navigate the design space and identify actuator geometry leading to the desired response, we develop a mathematical model based on nonlinear elasticity. The model predicts the actuator deformation as a function of the applied internal pressure, the geometry of the actuator and the mechanical properties of the layers used to fabricate it.

As described in the main text, our textile-based actuators, which are completely flat prior to inflation, upon pressurization inflate first to take on a cylindrical shape with a circular cross-section of inner radius  $R_i = W/\pi$  (Figure B.7c), and then to the shape of a toroidal segment (Figure B.7d). To simplify the analytical model, we neglect the initial flat configuration of the actuator, and instead assume that they start inflating from a cylindrical configuration, characterized by an inner radius  $R_i$ , outer radius  $R_o = R_i + T$  (where  $T = 0.6$  mm is the measured thickness of the textile composite), and length  $L$ . Since the results from Section B.1 showed the textile composites to be almost incompressible, we simplify the model by assuming that we can treat them as incompressible materials, which reduces the strain energy to

$$W = C_{10}(I_1 - 3) + \frac{k_1}{2k_2} \left( e^{k_2(I_4 - 1)^2} - 1 \right), \quad (\text{B.9})$$

where  $I_1 = \text{tr}(\mathbf{F}\mathbf{F}^T)$  and  $I_4 = \mathbf{F}\mathbf{M} \cdot \mathbf{F}\mathbf{M}$ ,  $\mathbf{F}$  being the deformation gradient and  $\mathbf{M}$  denoting the stiffest direction of the textile in the undeformed configuration. When pressurized, the actuators deform into a segment of a torus, described by its inner radius  $r_i$ , outer radius  $r_o$ , radius of curvature

$\rho$ , and length  $l_t$ . Such deformation is fully described by the deformation gradients

$$\mathbf{F}^{(\mathbf{t})} = \begin{pmatrix} \lambda_r^{(t)}(\theta) & 0 & 0 \\ 0 & \lambda_\theta^{(t)} & 0 \\ 0 & 0 & \lambda_z(\theta) \end{pmatrix} \quad (\text{B.10})$$

and

$$\mathbf{F}^{(\mathbf{b})} = \begin{pmatrix} \lambda_r^{(b)}(\theta) & 0 & 0 \\ 0 & \lambda_\theta^{(b)} & 0 \\ 0 & 0 & \lambda_z(\theta) \end{pmatrix} \quad (\text{B.11})$$

where

- $\lambda_z(\theta)$  is the axial stretch given by

$$\lambda_z(\theta) = \frac{l(\theta)}{L} \quad (\text{B.12})$$

where

$$l(\theta) = \frac{l_t(\rho - r_i \cos \theta)}{\rho + r_i}. \quad (\text{B.13})$$

Note that  $\lambda_z$  is a function of the circumferential angle  $\theta$ , since a constant axial stretch would result in a cylindrical shape, rather than a toroidal one. Note also that strictly speaking,  $l$  should be a function of both  $r$  and  $\theta$ . However, since the difference between the inner and outer radius is so small, we approximate the radius as a constant  $r_i$ .

- $\lambda_\theta^{(b)}$  is the circumferential stretch of the bottom part of the actuator

$$\lambda_\theta^{(b)} = k \frac{r_i}{R_i}, \quad (\text{B.14})$$

where  $k \in (0, 2)$  is a parameter that describes the extension in circumferential direction of the bottom layer. More specifically, for an actuator with circumference  $2\pi r_i$ , we assume that  $k\pi r_i$  is covered by the bottom textile and  $(2 - k)\pi r_i$  by the top one. Note that, since in the undeformed configuration both textiles cover half of the circumference, for  $P = 0$  we have  $k = 1$ .

- $\lambda_\theta^{(t)}$  is the circumferential stretch of the top part of the actuator

$$\lambda_\theta^{(t)} = (2 - k) \frac{r_i}{R_i}. \quad (\text{B.15})$$

- $\lambda_r^{(b)}$  is the radial stretch of the bottom part of the actuator

$$\lambda_r(\theta)^{(b)} = \frac{1}{\lambda_\theta^{(b)} \lambda_z(\theta)} \quad (\text{B.16})$$

since we assume the material to be incompressible

- $\lambda_r^{(t)}$  is the radial stretch of the top part of the actuator

$$\lambda_r(\theta)^{(t)} = \frac{1}{\lambda_\theta^{(t)} \lambda_z(\theta)} \quad (\text{B.17})$$

since we assume the material to be incompressible

To fully determine the actuator deformation during inflation, we need to find the geometric parameters  $r_i$ ,  $l_t$ ,  $\rho_t$  and  $k$  as a function of the pressure  $P$  inside the actuator. To solve this problem,

1. we calculate the strain energy of the system. To do this, we integrate the strain energy density given by Eq. (B.9) over the initial volume of the actuator:

$$U(\rho, r_i, l_t, k) = \int_0^L \int_{-\frac{\pi}{2}}^{\frac{\pi}{2}} \int_{R_i}^{R_o} W^{(b)}(I_1^{(b)}, I_4^{(b)}) R dR d\Theta dZ + \int_0^L \int_{\frac{\pi}{2}}^{\frac{3\pi}{2}} \int_{R_i}^{R_o} W^{(t)}(I_1^{(t)}, I_4^{(t)}) R dR d\Theta dZ, \quad (\text{B.18})$$

where  $W^{(b)}(I_1^{(b)}, I_4^{(b)})$  and  $W^{(t)}(I_1^{(t)}, I_4^{(t)})$  are the strain energy densities of the bottom and top textiles,  $R$ ,  $\Theta$  and  $Z$  are the radial, circumferential, and axial coordinates in the initial configuration,  $R_i$  and  $R_o$  are the initial inner and outer radii of the actuator, and  $L$  is the initial length of the actuator. Moreover,

$$I_1^{(b)} = \text{tr}(\mathbf{F}^{(b)})^T \cdot \mathbf{F}^{(b)} = \lambda_\theta^{(b)-2} \lambda_z(\theta)^{-2} + \lambda_\theta^{(b)2} + \lambda_z(\theta)^2 \quad (\text{B.19})$$

$$I_1^{(t)} = \text{tr}(\mathbf{F}^{(t)})^T \cdot \mathbf{F}^{(t)} = \lambda_\theta^{(t)-2} \lambda_z(\theta)^{-2} + \lambda_\theta^{(t)2} + \lambda_z(\theta)^2 \quad (\text{B.20})$$

$$I_4^{(b)} = \mathbf{F}^{(b)} \mathbf{M}^{(b)} \cdot \mathbf{F}^{(b)} \mathbf{M}^{(b)} \quad (\text{B.21})$$

$$I_4^{(t)} = \mathbf{F}^{(t)} \mathbf{M}^{(t)} \cdot \mathbf{F}^{(t)} \mathbf{M}^{(t)} \quad (\text{B.22})$$

where  $\mathbf{M}^{(b)}$  and  $\mathbf{M}^{(t)}$  identify the stiffest direction of the bottom textile and the top textile in the reference configuration. Finally, we do some simple geometric calculations to relate the current circumferential angle  $\theta$  to the reference circumferential angle  $\Theta$  using the parameter  $k$  as follows:

$$\theta = \begin{cases} k\Theta, & \text{if } -\frac{\pi}{2} \leq \Theta < \frac{\pi}{2} \\ \frac{k\pi}{2} + (2-k)(\Theta - \frac{\pi}{2}), & \text{if } \frac{\pi}{2} \leq \Theta < \frac{3\pi}{2} \end{cases} \quad (\text{B.23})$$

2. we minimize  $U$  using the constrained nonlinear solver fmincon in Matlab. Since the volume enclosed by a toroidal segment is

$$V = \pi r_i^2 \frac{l_t}{\rho + r_i} \rho, \quad (\text{B.24})$$

given a supplied volume  $V_{supplied}$ ,  $U$  must be minimized subject to the constraint  $V_{supplied} = V$ .

3. We solve the Cauchy equilibrium equations to relate the geometric parameters to the internal pressure:

$$P = \frac{1}{2\pi} \int_{-\frac{\pi}{2}}^{\frac{\pi}{2}} \int_{r_i}^{r_o} \frac{\sigma_{\theta\theta}^{(b)}(\Theta) - \sigma_{rr}^{(b)}}{r} dr d\Theta + \int_{\frac{\pi}{2}}^{\frac{3\pi}{2}} \int_{r_i}^{r_o} \frac{\sigma_{\theta\theta}^{(t)}(\Theta) - \sigma_{rr}^{(t)}}{r} dr d\Theta \quad (\text{B.25})$$

where the Cauchy stress  $\sigma$  is given by

$$\sigma^{(i)} = -p\mathbf{I} + 2\frac{\partial W^{(i)}}{\partial I_1} \mathbf{F}^{(i)} \mathbf{F}^{(i)\mathbf{T}} + 2\frac{\partial W^{(i)}}{\partial I_4} \mathbf{m}^{(i)} \otimes \mathbf{m}^{(i)} \quad (\text{B.26})$$

where  $p$  is a hydrostatic stress and  $m$  is the stiffest direction of the textile in the current configuration ( $\mathbf{m}^{(i)} = \mathbf{F}\mathbf{M}^{(i)}$ ). Since the textiles are very thin, we assume that the stress in the radial direction is negligible ( $\sigma_{rr} = 0$ ), and this allows us to eliminate  $p$ .

To validate our analytical model, we performed finite element analysis (FEA) using Abaqus/Explicit. In all our models the actuator was meshed with shell elements (S4R) and the response of the material was captured using the Holzapfel-Gasser-Ogden model with suitable set of parameters. In the simulations one end of the actuator was kept fixed and the actuator was inflated under volume

control by modeling the actuator chamber as a fluid-filled cavity and increasing the temperature in the cavity, causing the fluid volume to increase.

To begin with, we used FEA to compare the inflation of actuators with initial flat and initial cylindrical configuration. To this end, we constructed a cylinder of length  $L$  and radius  $R = W/\pi$  and made of two materials (top textile and bottom textile) and a flat actuator made of two planar rectangular sheets of length  $L$  and width  $W$  (one for each textile) joined together at the edges using a tie constraint. Note that for the latter, we cannot immediately use volume control, as the air chamber has initially zero volume - a condition under which a fluid-filled cavity cannot be defined. To circumvent this problem, we initially applied a very small pressure load and then switched to volume control to avoid instabilities.

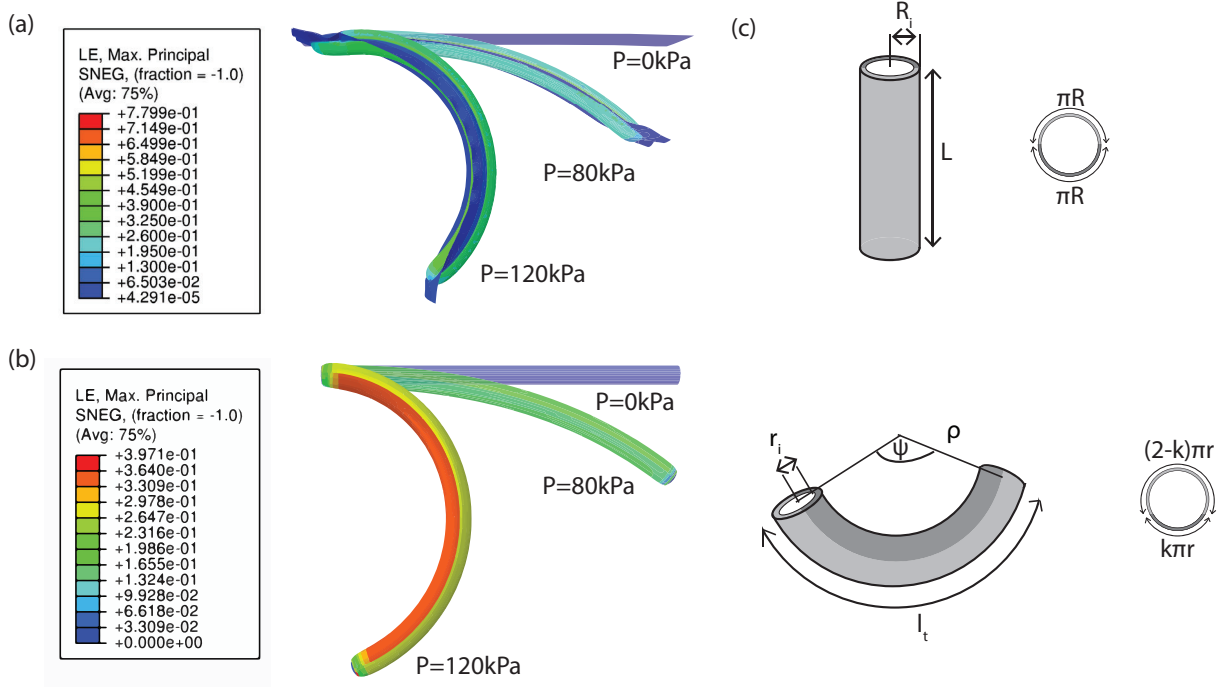


Figure B.7: (a) Finite element simulation of actuator starting from flat configuration. (b) Finite element simulation of actuator starting from cylindrical configuration. (c) Schematic of cylinder (and cross-section) representing initial actuator geometry and schematic of toroidal segment (and cross-section) representing current actuator geometry

In Figures B.7a,b we show numerical snapshots of such actuators at three different inflation pressures for  $L = 100$  mm and  $W = 15$  mm. In both actuators the top textile is modeled using a Holzapfel-Gasser-Ogden material with parameters  $C = 0.91$  MPa,  $k_1 = 0.07$  MPa, and  $k_2 = 2.4$ ,



while the bottom one is modeled using a Holzapfel-Gasser-Ogden material with  $C = 1.3$  MPa,  $k_1 = 0.006$  MPa, and  $k_2 = 1.6$ . We see in Figure B.7a,b that the actuators behave similarly. Their behavior is compared quantitatively in Figure B.8, where we plot bend angle per unit length, circumferential stretch, and maximum axial stretch as a function of pressure. We see that at lower pressures, the actuators behave the same way, and the behaviors deviate slightly at higher pressures. Moreover, we find that the analytical model matches the cylindrical FEA exactly. To further investigate the accuracy of the model, we performed FEA simulations for different geometries and different material properties for the top textile (always using the Holzapfel-Gasser-Ogden model). The results are shown in Figure B.8 and are compared to the analytical results. As before, the analytical model matches the cylindrical FEA exactly, while the flat FEA differs from the cylindrical FEA at high pressures. Since the discrepancy between the cylindrical and flat FEA results is quite small, we concluded that assuming cylindrical geometry was a reasonable approximation to make in the analytical model.

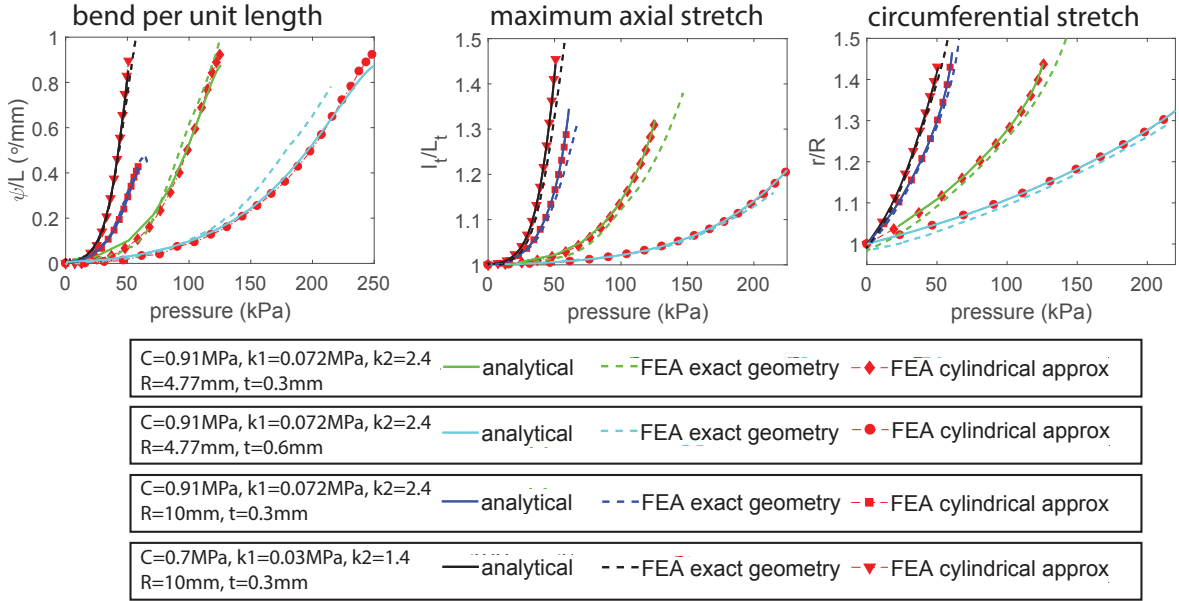


Figure B.8: Comparison of analytical results with finite element simulations using exact geometry from experiments and using cylindrical approximation

Next, we compare the predictions of our model with the experimental result collected during inflation of three actuators with length  $L = 110$  mm and widths 10 mm, 20 mm, and 30 mm. We see a reasonably good match between model and experiment, with discrepancies most likely due to

the constitutive models for the textiles not picking up all of the complexities of the textile behavior

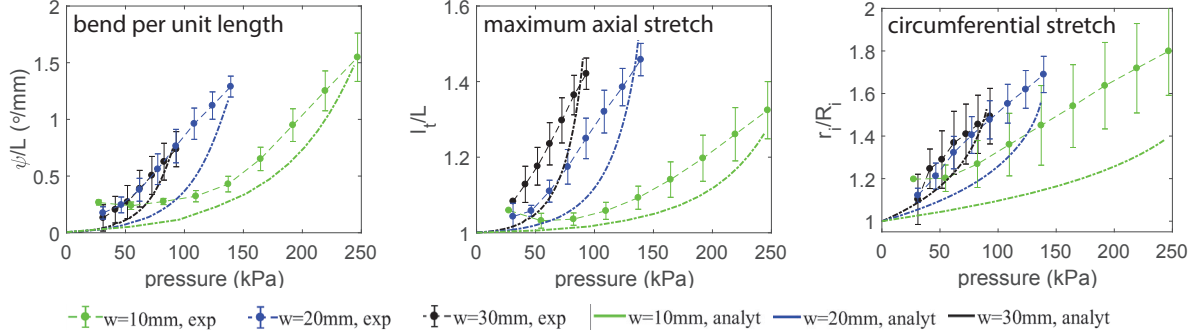


Figure B.9: Comparison of model prediction and experimental results for three actuators with different geometries. In each case, the bottom textile is a Holzapfel material with parameters  $C = 1.3MPa$ ,  $k_1 = 0.006MPa$ , and  $k_2 = 1.6$ , the top textile is a Holzapfel material with parameters indicated in the legend, and the actuator radius and material thickness are as indicated in the legend.

## B.5 Application to assistive glove

In this section, we describe how we use our modeling and manufacturing techniques to realize a glove which mimics hand motion and has the potential to assist users who have impaired hand function. We first describe how to design and fabricate individual articulated actuators which can mimic finger motion, and then show how to integrate those into a glove.

### B.5.1 Articulated actuators

To produce actuators which mimic the motion of a finger, we require some portions of the actuator to bend upon inflation, while other portions of the actuator resist deformation. These alternating bending and straight segments are connected by a single air channel, so each actuator requires only one pressure input. The straight segments are realized by applying polyamide film to the actuator, which significantly increases its stiffness in those areas.

**Actuator design** We chose an everyday task – grasping a glass or bottle – and designed articulated actuators to mimic the typical motion that a person’s fingers make when carrying out that task i.e. the initially flat actuators should inflate to a configuration which mimics a person’s fingers grasping a bottle. We defined a pressure operating range of  $0-35psi(0-240kPa)$ , as this range is reasonably easy to generate and safe for a wearable device.

The average joint angles for grasping a cylindrical object of diameter  $50.8mm$  (approximately the size of a water bottle) are shown in Table B.1[103] – these dictate what the bend angles of the actuators should be. To identify appropriate lengths for the straight segments of the actuators, we measured the hands of 12 people who wear a size large glove. We measured the distances between the joints on each of their fingers – the average values are reported in Table B.1. From these lengths and angles, we can draw the configuration which each actuator needs to take in order to grasp a bottle (Figure B.10a-d).

|           | index | middle | ring | little |
|-----------|-------|--------|------|--------|
| MCP angle | 52 °  | 56 °   | 50 ° | 46 °   |
| PIP angle | 56 °  | 52 °   | 48 ° | 32 °   |
| DIP angle | 38 °  | 44 °   | 40 ° | 36 °   |
| $L_1$     | 89mm  | 85mm   | 77mm | 70mm   |
| $L_2$     | 46mm  | 51mm   | 47mm | 38mm   |
| $L_3$     | 27mm  | 31mm   | 27mm | 19mm   |
| $L_4$     | 26mm  | 28mm   | 28mm | 26mm   |

Table B.1

Next, we use our analytical model to identify the actuator geometries which will result in the required motions upon inflation.

1. To select the actuator geometry, there are some requirements which should be taken into account. The actuator should
  - (a) have width between  $10mm$  and  $15mm$ , to ensure it is wide enough to be fabricated easily, but narrow enough to fit on a finger
  - (b) be as narrow as possible, to ensure it remains low-profile when inflated
  - (c) achieve the target configuration at a low pressure, to ensure safe operation
  - (d) have segment lengths which fit over the joints
2. We use our analytical model to find the smallest actuator width which will produce the required bend per unit length within the allowed pressure range. We found this was  $11.6mm$ . We fabricated all actuators with this width.

3. Now that we have chosen the width, we have determined that the bend per unit length for all bending segments will be  $2.07^\circ/mm$ . This allows us to calculate what the lengths of all the bend segments will be - we take the required angle for each joint and divide by the bend per unit length to find the lengths of the bending segments:

$$L_{MCP} = \frac{\psi_{MCP}}{\omega} \quad L_{PIP} = \frac{\psi_{PIP}}{\omega} \quad L_{DIP} = \frac{\psi_{DIP}}{\omega} \quad (B.27)$$

These are shown in green in Figure B.10e-h.

4. Finally, we calculate the lengths of the straight segments in between:

$$\begin{aligned} L_s^{(1)} &= L_1 - \frac{L_{MCP}}{2} & L_s^{(2)} &= L_2 - \frac{L_{MCP}}{2} - \frac{L_{PIP}}{2} \\ L_s^{(3)} &= L_3 - \frac{L_{PIP}}{2} - \frac{L_{DIP}}{2} & L_s^{(4)} &= L_4 - \frac{L_{DIP}}{2} \end{aligned} \quad (B.28)$$

shown in blue in Figure B.10e-h.

We fabricate the actuators as shown in Figure B.5. If our calculations results in any segments which are shorter than  $8mm$ , we ignore those segments to simplify fabrication e.g. the index finger design in Figure B.10e shows a straight segment of length  $4mm$ , but when fabricating this actuator, we remove this segment and instead have a continuous bending segment for the PIP and DIP joints. The fabricated actuators are shown in Figure B.10i-l.

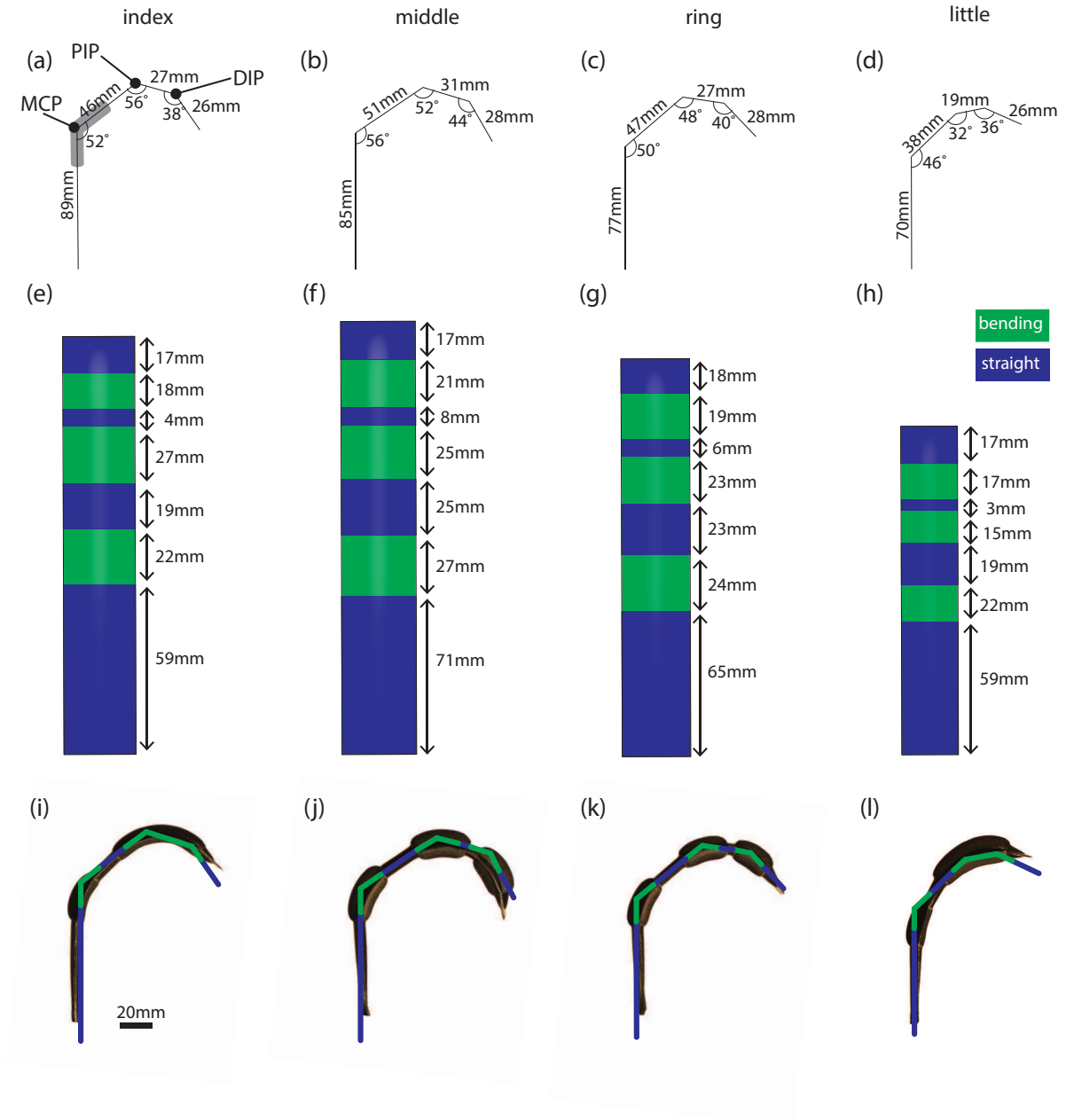


Figure B.10: (a) Target lengths and joint angles for the index finger actuator. The shaded region on the MCP joint indicates the longest allowed length of the bend segment for this joint. (b)-(d) Target lengths and joint angles for the middle, ring, and little finger actuators. (e)-(f) Designs for the index, middle, ring, and little finger actuators, as prescribed by the analytical model. (i)-(l) Actuator configurations at 240kPa, overlaid with the target configurations.

### B.5.2 Glove fabrication

We use the designs from the previous section to fabricate a glove which mimics hand motion. We use the designs shown in Figure B.10e-h, but now fabricate all actuators in parallel from the same sheet (see Figure B.11). Up to this point, we have not considered the motion of the thumb, since it is more complex than that of the fingers. In designing the glove, we do include an air chamber for the thumb, but do not analyze its motion nor attempt to replicate thumb motion exactly – this will be explored in our future work.

To easily align all the layers for the glove, we use a plastic board in which we have laser cut holes for alignment pins. Each design file has corresponding holes, so we can place each layer of the glove on the board, and use the pins to make sure they are aligned correctly. Figure B.11 illustrates the fabrication process:

- a First place the high stretch textile on the board, and place the air-impermeable film on top. Tack the film in place using an iron (green area in Figure B.11a), then trim the edges of the film (red area in Figure B.11a). Press the film onto the textile at a temperature of  $340^{\circ}F$  and a pressure of  $60psi$  for  $150s$ .
- b Repeat step a for the low-stretch textile (Figure B.11b).
- c Place the laminated low stretch textile back on the board (film side up). Place the seal layer of air-impermeable film on top. Tack it in place with an iron (green area) and trim away the excess film (red area). Remove the assembly from the board, and press it at a temperature of  $340^{\circ}F$  and a pressure of  $60psi$  for  $150s$ . This step leaves an additional thin layer of film around the edge of each of the actuators to improve the seal between top and bottom layers.
- d Place the laminated low stretch textile back on the board (film side up) and place the PVA on top (Figure B.11d). Lightly tack the PVA in place using an iron and trim away the excess. Place the laminated high stretch textile on top of the assembly (film side down). Tack the high stretch layer in place using an iron. Remove the assembly from the board, and press it at a temperature of  $340^{\circ}F$  and a pressure of  $70psi$  for  $180s$ .
- e Now that the top and bottom layers have been sealed together, place them back on the alignment board. Place the rigid film layer on top (Figure B.11e). Tack on the film and trim

the excess. Remove the assembly from the board and bond in the heat press. Repeat this step to add the bottom layer of rigid film.

f Trim the excess fabric from the edges of the glove and fill the five chambers with water to dissolve the PVA. When the PVA has dissolved, drain the water and leave the glove to dry (Figure B.11f). Insert a tube into each of the five chambers and glue the tubes in place. Sew the laminated glove to an off the shelf size large glove using a whip stitch.

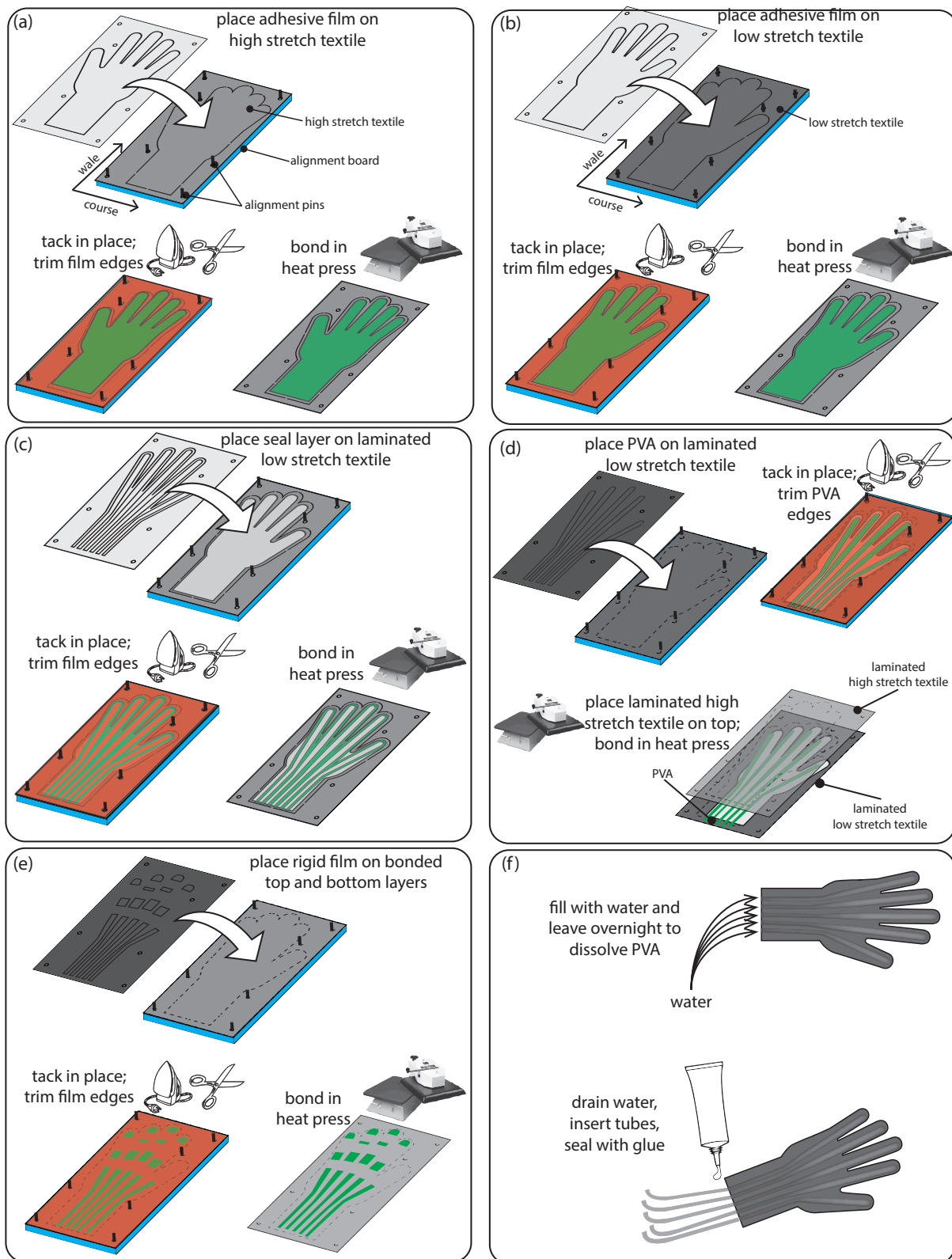


Figure B.11: Glove fabrication



Since we fabricate the glove all in one piece, we end up with the index, ring, and little fingers being fabricated at a slight angle to the wale direction of the textiles. We ran two finite element simulations to check that this would not adversely affect their behavior. In each case, we simulated a cylindrical actuator made from two Holzapfel materials: the top had material properties  $C = 0.64$  MPa,  $k_1 = 0.12$  MPa, and  $k_2 = 0.52$  while the bottom had material properties  $C = 0.99$  MPa,  $k_1 = 0.017$  MPa, and  $k_2 = 1.1$ . For the simulation shown in Figure B.12A, the materials were arranged such that the direction corresponding to the wale of the textile was aligned with the axial direction of the cylinder. In Figure B.12B, this direction was defined at an angle of  $10^\circ$  to the axial direction. We found that the two actuators behaved very similarly. In B.12B, we see that the deformation of the actuator is not symmetric - it undergoes some twisting. But this deformation is very small, and since in the fingers the bending segments are quite short, this effect would be even less pronounced.

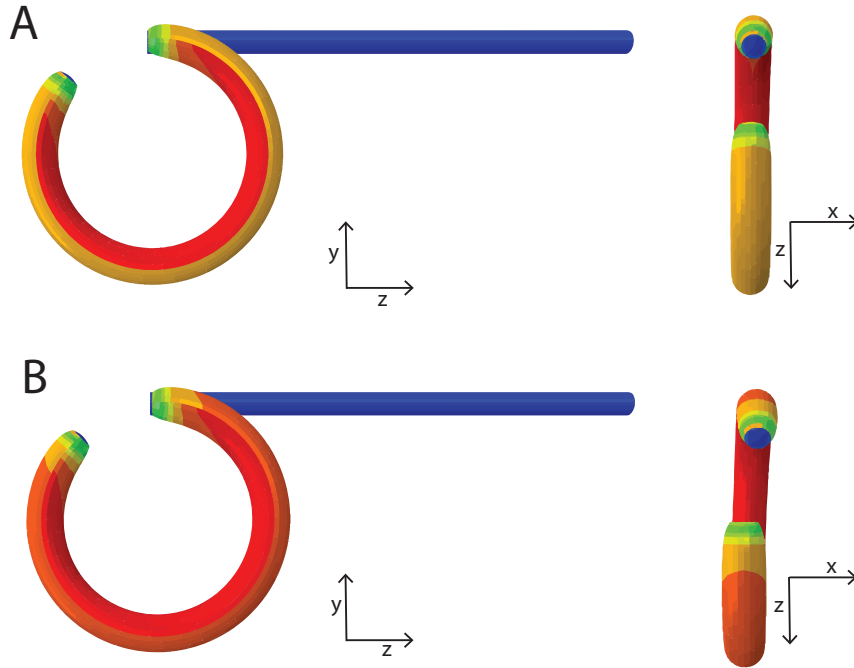


Figure B.12: Finite element analysis results comparing (A) an actuator with wale direction aligned with the axis to (B) an actuator with wale direction at an angle of  $10^\circ$  to the axis.

## References

- [1] Asimo. <http://hondau3-x.net/asimo>. Accessed: 2017-09-16.
- [2] A. H. Morin. Elastic diaphragm, December 19 1947. US Patent 2642091A.
- [3] P. Polygerinos, N. Correll, S. A. Morin, B. Mosadegh, C. D. Onal, K. Petersen, M. Cianchetti, M. T. Tolley, and R. F. Shepherd. Soft robotics: Review of fluid-driven intrinsically soft devices; manufacturing, sensing, control, and applications in human-robot interaction. *Advanced Engineering Materials*, 2017.
- [4] M. T. Tolley et al. A resilient, untethered soft robot. *Soft Robotics*, 1:213–223, 2014.
- [5] Roam robotics. <https://otherlab.com/>. Accessed: 2017-09-16.
- [6] Soft robotics inc. <https://www.softroboticsinc.com/>. Accessed: 2017-09-16.
- [7] M. Wehner, R. L. Truby, D. J. Fitzgerald, B. Mosadegh, G. M. Whitesides, J. A. Lewis, and R. J. Wood. An integrated design and fabrication strategy for entirely soft, autonomous robots. *Nature*, 536(7617):451–455, 2016.
- [8] R. F. Shepherd, F. Ilievski, W. Choi, S. A. Morin, A. A. Stokes, A. D. Mazzeo, X. Chen, M. Wang, and G. M. Whitesides. Multigait soft robot. *PNAS*, 108(51), 2011.
- [9] K. Suzumori, S. Iikura, and H. Tanaka. Applying a flexible microactuator to robotic mechanisms. *IEEE Control Syst*, 12:21–27, 1992.
- [10] R. Deimel and O. Brock. A novel type of compliant, underactuated robotic hand for dexterous grasping. *Proc Robotics: Science and Systems*, 2014.
- [11] F. Carpi, R. Kornbluh, P. Sommer-Larsen, and G. Alici. Electroactive polymer actuators as artificial muscles: are they ready for bioinspired applications? *Bioinspiration and Biomimetics*, 6(4):1–10, 2011.
- [12] Y. Bar-Cohen. *Electroactive polymer (EAP) actuators as artificial muscles: reality, potential, and challenges*. SPIE, 2004.
- [13] H. Lin, G. G. Leisk, and B. Trimmer. Gogobot: a caterpillar-inspired soft-bodied rolling robot. *Bioinspiration and Biomimetics*, 6(2), 2011.
- [14] H. F. Schulte, D. F. Adamski, and J. R. Pearson. Characteristics of the braided fluid actuator. Technical report, University of Michigan, 1961.
- [15] T. Takagi and Y. Sakaguchi. Pneumatic actuator for manipulator, October 7 1986. US4615260A.
- [16] C. P. Chou and B. Hannaford. Static and dynamic characteristics of McKibben pneumatic artificial muscles. *Int Conf Robot Autom*, pages 281–286, 1994.
- [17] C. P. Chou and B. Hannaford. Measurement and modeling of McKibben pneumatic artificial muscles. *IEEE Trans Robot Autom*, 12(1):90–102, 1996.

- [18] G. K. Klute and B. Hannaford. Accounting for elastic energy storage in McKibben artificial muscle actuators. *ASME J Dynamic Systems, Measurement and Control*, 122(2):386–388, 2000.
- [19] N. Tsagarakis and D. G. Caldwell. Improved modelling and assessment of pneumatic muscle actuators. *Proc IEEE Inc Conf Robot Autom*, pages 3641–3646, 2000.
- [20] S. Davis, N. Tsagarakis, J. Canderle, and D. G. Caldwell. Enhanced modelling and performance in braided pneumatic muscle actuators. *International Journal of Robotics Research*, 22:213–227, 2003.
- [21] S. Davis and D. G. Caldwell. Braid effects on contractile range and friction modeling in pneumatic muscle actuators. *International Journal of Robotics Research*, 25(4):359–369, 2006.
- [22] B. Tondu and P. Lopez. McKibben artificial muscle robot actuators. *IEEE Control Systems Magazine*, pages 15–38, 2000.
- [23] B. Tondu. Modeling of the McKibben artificial muscle: a review. *J Intelligent Material Systems and Structures*, 23(3):225–253, 2012.
- [24] F. Daerden and D. Lefeber. Pneumatic artificial muscles: actuators for robotics and automation. *Eur J Mech Eng*, 47(1):10–21, 1996.
- [25] A. Mettam. Inflatable servo actuators. Technical report, Ministry of Aviation, Aeronautical Research Council, 1964.
- [26] R. Niiyama, D. Rus, and S. Kim. Pouch motors: Printable/Inflatable soft actuators for robotics. *IEEE Int Conf Robot Autom*, pages 6332–6337, 2014.
- [27] K. Suzumori, S. Iikura, and H. Tanaka. Flexible microactuator for miniature robots. *IEEE MEMS*, pages 204–209, 1991.
- [28] P. Polygerinos et al. Modeling of soft fiber-reinforced bending actuators. *IEEE Trans Robot*, 31:778–789, 2015.
- [29] B. Mosadegh, P. Polygerinos, C. Keplinger, S. Wennstedt, R. F. Shepherd, U. Gupta, J. Shim, K. Bertoldi, C. J. Walsh, and G. M. Whitesides. Pneumatic networks for soft robotics that actuate rapidly. *Adv Funct Mater*, 24(15):2163–2170, 2014.
- [30] D. Yang, M. S. Verma, J. H. So, B. Mosadegh, C. Keplinger, B. Lee, F. Khashai, E. Lossner, Z. Suo, and G. M. Whitesides. Buckling pneumatic linear actuators inspired by muscle. *Advanced Materials Technologies*, 1(3):160055, 2016.
- [31] R. Niiyama, X. Sun, C. Sung, B. An, D. Rus, and S. Kim. Pouch motors: Printable soft actuators integrated with computational design. *Soft Robotics*, 2(2):59–70, 2015.
- [32] K. Suzumori, A. Koga, and R. Haneda. Microfabrication of integrated FMAs using stereo lithography. *Proc IEEE MEMS*, pages 136–141, 1994.
- [33] Y. Elsayed, A. Vincensi, C. Lekakou, T. Geng, C. M. Saaj, T. Ranzani, M. Cianchetti, and A. Menciassi. Finite element analysis and design optimization of a pneumatically actuating silicone module for robotic surgery applications. *Soft Robotics*, 1(4):255–262, 2014.

- [34] S. Hirai et al. Qualitative synthesis of deformable cylindrical actuators through constraint topology. *Proc IEEE/RSJ Int Conf Intell Robot Syst*, 1:197–202, 2000.
- [35] S. Hirai, T. Masui, and S. Kawamura. Prototyping pneumatic group actuators composed of multiple single-motion elastic tubes. *Proc IEEE Int Conf Robot Autom*, pages 3807–3812, 2001.
- [36] G. Krishnan J. Bishop-Moser and S. Kota. Fiber-reinforced actuator, February 12 2015. US20150040753 A1.
- [37] G. Krishnan, J. Bishop-Moser, C. Kim, and S. Kota. Kinematics of a generalized class of pneumatic artificial muscles. *J. Mech. Robot.*, 7:4, 2015.
- [38] G. Singh and G. Krishnan. An isoperimetric formulation to predict deformation behavior of pneumatic fiber reinforced elastomeric actuators. *IROS*, pages 1738–1743, 2015.
- [39] A. A. M. Faudzi, M. Rusydi, M. Razif, I. N. A. M. Nordin, K. Suzumori, S. Wakimoto, and D. Hirooka. Development of bending soft actuator with different braided angles. *IEEE/ASME Int Conf Advanced Intelligent Mechatronics*, pages 1093–1098, 2012.
- [40] I. N. A. M. Nordin, M. R. M. Razif, A. A. M. Faudzi, E. Natarajan, K. Iwata, and K. Suzumori. 3-D finite-element analysis of fiber-reinforced soft bending actuator for finger flexion. *IEEE/ASME International Conference on Advanced Intelligent Mechatronics*, pages 128–133, 2013.
- [41] Z. Wang, P. Polygerinos, J. T. B. Overvelde, K. C. Galloway, K. Bertoldi, and C. J. Walsh. Interaction forces of soft fiber-reinforced bending actuators. *IEEE/ASME Transactions on Mechatronics*, 22(2):717–727, 2017.
- [42] M. Memarian, R. Gorbet, and D. Kulic. Modelling and experimental analysis of a novel design for soft pneumatic artificial muscles. *Int Conf Intell Robot Syst*, pages 1718–1724, 2015.
- [43] F. Daerden and D. Lefeber. The concept and design of pleated pneumatic artificial muscles. *Int J Fluid Power*, 2(3):41–50, 2001.
- [44] S. Sanan, P. S. Lynn, and S. T. Griffith. Pneumatic torsional actuators for inflatable robots. *J Mech Robot*, 6(3), 2014.
- [45] F. Ilievski, A. D. Mazzeo, R. F. Shepherd, X. Chen, and G. M. Whitesides. Soft robotics for chemists. *Angewandte Chemie-International Edition*, 50(8):1890–1895, 2011.
- [46] Y. Sun, Y. S. Song, and J. Paik. Characterization of silicone rubber based soft pneumatic actuators. *IEEE/RSJ Int Conf Intell Robot Syst*, pages 4446–4453, 2013.
- [47] L. Paez, G. Agarwal, and J. Paik. Design and analysis of a soft pneumatic actuator with origami shell reinforcement. *Soft Robotics*, 3(3):109–119, 2016.
- [48] P. Moseley et al. Modeling, design, and development of soft pneumatic actuators with finite element method. *Adv. Eng. Mater.*, 2015.

- [49] S. Wakimoto, K. Suzumori, and K. Ogura. Miniature pneumatic curling rubber actuator generating bidirectional motion with one air-supply tube. *Advanced Robotics*, 25:1311–1330, 2011.
- [50] D. Yang, M. S. Verma, E. Lossner, D. Stothers, and G. M. Whitesides. Negative-pressure soft linear actuator with a mechanical advantage. *Advanced Materials Technologies*, 2(1):1600164, 2017.
- [51] R. V. Martinez et al. Robotic tentacles with three-dimensional mobility based on flexible elastomers. *Adv Mater*, 25:205–212, 2013.
- [52] R. V. Martinez, C. R. Fish, X. Chen, and G. M. Whitesides. Elastomeric origami: Programmable paper-elastomer composites as pneumatic actuators. *Adv Funct Mater*, 22(7):1376–1384, 2012.
- [53] R. F. Shepherd, A. A. Stokes, R. M. D. Nunes, and G. M. Whitesides. Soft machines that are resistant to puncture and that self seal. *Advanced Materials*, 25(46):6709–6713, 2013.
- [54] C. Majidi. Soft robotics: A perspective - current trends and prospects for the future. *Soft Robotics*, 1:5–1, 2013.
- [55] E. T. Roche, R. Wohlfarth, J. T. B. Overvelde, N. V. Vasilyev, F. A. Pigula, D. J. Mooney, K. Bertoldi, and C. J. Walsh. A bioinspired soft actuated material. *Advanced Materials*, 26(8):1200–1206, 2014.
- [56] P. Polygerinos, Z. Wang, K. C. Galloway, R. J. Wood, and C. J. Walsh. Soft robotic glove for combined assistance and at-home rehabilitation. *Robot Auton Syst*, 73:139, 2015.
- [57] S. Sanan, M. H. Ornstein, and C. G. Atkeson. Physical human interaction for an inflatable manipulator. *Proc IEEE Eng Med Biol Soc*, pages 7401–7404, 2011.
- [58] G. Andrikopoulos, G. Nikolakopoulos, and S. Manesis. A survey on applications of pneumatic artificial muscles. *19th Mediterranean Conference on Control and Automation*, pages 1439–1446, 2011.
- [59] Z. Zhang and M. Philen. Modeling, analysis and experiments of inter yarn compaction effects in braided composite actuators. *J Compos Mater*, 47:3211–3225, 2013.
- [60] K. Mortier. *Braided pneumatic muscles for rehabilitation apparatus*. PhD thesis, Politecnico di Torino, 2014.
- [61] M. B. Pritts and C. D. Rahn. Design of an artificial muscle continuum robot. *IEEE Trans Rob Autom*, 5:4742–4746, 2004.
- [62] S. Konishi, M. Nokata, O. C. Jeong, S. Kusuda, T. Sakakibara, M. Kuwayama, and H. Tsutsumi. Pneumatic micro hand and miniaturized parallel link robot for micro manipulation robot system. *IEEE Inc Conf Robot Autom*, pages 1036–1041, 2006.
- [63] J. B. Cowey. The structure and function of the basement membrane muscle system in amphiporus lactifloreus (nemertea). *Q J Microsc Sci*, 93:1–15, 1952.

- [64] R. B. Clark and J. B. Cowey. Factors controlling the change of shape of certain nemertean and turbellarian worms. *J Exp Biol*, 35:731–748, 1958.
- [65] G. A. Holzapfel, T. C. Gasser, and R. W. Ogden. A new constitutive framework for arterial wall mechanics. *J Elast*, 61:1–48, 2000.
- [66] K. J. Quillin. Kinematic scaling of locomotion by hydrostatic animals: ontogeny of peristaltic crawling by the earthworm *lumbricus terrestris*. *J Exp Biol*, 202:661–674, 1999.
- [67] R. S. McCurley and W. M. Kier. The functional morphology of starfish tube feet: The role of a crossed-fiber helical array in movement. *Biol Bull*, 188:197–209, 1995.
- [68] J. E. Adkins and R. S. Rivlin. Large elastic deformations of isotropic materials x. reinforcement by inextensible cords. *Philos Trans R Soc A*, 248:201–223, 1955.
- [69] A. S. D. Wang and A. Ertepinar. Stability and vibrations of elastic thick-walled cylindrical and spherical shells subjected to pressure. *Int J Nonlinear Mech*, 7:539–555, 1972.
- [70] D. M. Haughton and R. W. Ogden. Bifurcation of inflated circular cylinders of elastic material under axial loading-ii. exact theory for thick-walled tubes. *J Mech Phys Solids*, 27:489–512, 1979.
- [71] A. Goriely and M. Tabor. Rotation, inversion, and perversion in anisotropic elastic cylindrical tubes and membranes. *Proc Royal Soc A*, 469:20130011, 2013.
- [72] G. Krishnan, J. Bishop-Moser, C. Kim, and S. Kota. Evaluating mobility behavior of fluid filled fiber-reinforced elastomeric enclosures. *ASME IDETC/CIE*, 2012.
- [73] J. Bishop-Moser, G. Krishnan, C. Kim, and S. Kota. Kinematic synthesis of fiber reinforced soft actuators in parallel combinations. *ASME IDETC/CIE*, 2012.
- [74] J. Denavit and R. S. Hartenberg. A kinematic notation for lower pair mechanisms. *Applied Mechanics*, 22:215–221, 1955.
- [75] R. M. Murray, Z. Li, and S. S. Sastry. *A Mathematical Introduction to Robotic Manipulation*. CRC Press, 1994.
- [76] A. Aristidou and J. Lasenby. Inverse kinematics: a review of existing techniques and introduction of a new fast iterative solver. Technical report, University of Cambridge, 2009.
- [77] A. Colome and C. Torras. Redundant inverse kinematics: Experimental comparative review and two enhancements. *IEEE/RSJ Int Conf Intell Robot Syst*, 12:5333–5340, 2012.
- [78] A. D. Marchese, C. D. Onal, and D. Rus. Autonomous soft robotic fish capable of escape maneuvers using fluidic elastomer actuators. *Soft Robotics*, 1:75–87, 2014.
- [79] L. Connelly et al. Use of a pneumatic glove for hand rehabilitation following stroke. *IEEE EMBC*, pages 2434–2437, 2009.
- [80] D. Rus and M. T. Tolley. Design, fabrication and control of soft robots. *Nature*, 521:467–475, 2015.

- [81] J. C. Case, E. L. White, and R. K. Kramer. Soft material characterization for robotic applications. *Soft Robotics*, 2:80–87, 2015.
- [82] A. D. Marchese, R. Tedrake, and D. Rus. Dynamics and trajectory optimization for a soft spatial fluidic elastomer manipulator. *Int J Robotics Research*, page 10.1177/0278364915587926, 2015.
- [83] J. Bishop-Moser and S. Kota. Design and modeling of generalized fiber-reinforced pneumatic soft actuators. *IEEE Trans Robot*, 31:536–545, 2015.
- [84] F. Connolly, P. Polygerinos, C. J. Walsh, and K. Bertoldi. Mechanical programming of soft actuators by varying fiber angle. *Soft Robotics*, 2:26–32, 2015.
- [85] K. C. Galloway, P. Polygerinos, C. J. Walsh, and R. J. Wood. Mechanically programmable bend radius for fiber-reinforced soft actuators. *Int Conf Adv Robot*, pages 1–6, 2013.
- [86] K. Galloway et al. Multi-segment reinforced actuators and applications, May 7 2015. US20160252110A11.
- [87] A. Firouzeh, M. Salerno, and J. Paik. Soft pneumatic actuator with adjustable stiffness layers for multi-dof actuation. *Int Conf Intell Robot Syst*, 2015.
- [88] J. E. Adkins and R. S. Rivlin. Large elastic deformations of isotropic materials X. Reinforcement by inextensible cords. *Phil T Royal Soc A*, 248:201–223, 1955.
- [89] F. Kassianidis. *Boundary-value problems for transversely isotropic hyperelastic solids*. PhD thesis, University of Glasgow, 2007.
- [90] G. A. Holzapfel. *Nonlinear Solid Mechanics. A continuum approach for engineering*. Wiley, 2000.
- [91] R. W. Ogden. *Non-Linear Elastic Deformations*. Dover, 1984.
- [92] T. Noritsugu, M. Takaiwa, and D. Sasaki. Power assist wear driven with pneumatic rubber artificial muscles. *Int Conf Mechatronics and Machine Vision in Practice*, pages 539–544, 2008.
- [93] Y. L. Park, J. Santos, K. C. Galloway, E. C. Goldfield, and R. J. Wood. A soft wearable robotic device for active knee motions using flat pneumatic artificial muscles. *IEEE Int Conf Robot Autom*, pages 4805–4810, 2014.
- [94] O. C. Jeong, S. Kusuda, and S. Konishi. All pdms pneumatic balloon actuators for bidirectional motion of micro finger. *18th IEEE International Conference on Micro Electro Mechanical Systems*, pages 407–410, 2005.
- [95] J. W. Hetrick. Safety cushion assembly for automotive vehicles, August 18 1953. US Patent 2649311A.
- [96] W. A. Bary. Inflatable structure, April 28 1955. US Patent 2837101A.
- [97] E. C. Fink. Inflatable tent structure, July 16 1959. US Patent 3055379A.



- [98] L. Cappello, K. C. Galloway, S. Sanan, D. A. Wagner, R. Granberry, S. Engelhardt, F. L. Haufe, J. D. Peisner, and C. J. Walsh. Exploiting textile mechanical anisotropy for fabric-based pneumatic actuators. *in preparation*, 2018.
- [99] L. Cappello, J. T. Meyer, K. C. Galloway, J. D. Peisner, R. Granberry, D. A. Wagner, S. Engelhardt, S. Paganoni, and C. J. Walsh. A fabric-based soft robotic glove to restore hand function after spinal cord injury. *in preparation*, 2018.
- [100] K. Suzumori, S. Endo, T. Kanda, N. Kato, and H. Suzuki. A bending pneumatic rubber actuator realizing soft-bodied manta swimming robot. *IEEE Int Conf Robot Autom*, pages 4975–4980, 2007.
- [101] F. Connolly, C. J. Walsh, and K. Bertoldi. Automatic design of fiber-reinforced soft actuators for trajectory matching. *Proceedings of the National Academy of Sciences*, 114(1):51–56, 2017.
- [102] G. Singh and G. Krishnan. A constrained maximization formulation to analyze deformation of fiber reinforced elastomeric actuators. *Smart Materials and Structures*, 26(6), 2017.
- [103] J. W. Lee and K. Rim. Measurement of finger joint angles and maximum finger forces during cylinder grip activity. *J Biomed Eng*, 13:152–162, 1991.
- [104] A. Sedal, D. Bruder, J. Bishop-Moser, R. Vasudevan, and S. Kota. A constitutive model for torsional loads on fluid-driven soft robots. *Proc ASME IDETC/CIE*, 2017.
- [105] D. Trivedi, A. Lotfi, and C. D. Rahn. Geometrically exact models for soft robotic manipulators. *IEEE Trans Robot*, 24(4):1497–1502, 2008.
- [106] B. Gorissen, D. Reynaerts, S. Konishi, K. Yoshida, J. Kim, and M. De Volder. Elastic inflatable actuators for soft robotic applications. *Advanced Materials*, 29(43), 2017.
- [107] D. B. Reynolds, D. W. Repperger, C. A. Phillips, and G. Bandry. Modeling the dynamic characteristics of pneumatic muscle. *Annals of Biomedical Engineering*, 31:310–317, 2003.
- [108] G. Belforte, G. Eula, A. Ivanov, and S. Sirolli. Soft pneumatic actuators for rehabilitation. *Actuators*, 3:84–106, 2014.
- [109] S. E. Zacharski. *Nonlinear mechanical behavior of automotive airbag fabrics: an experimental and numerical investigation*. PhD thesis, The University of British Columbia, 2016.
- [110] D. Shea K. Albert S. Griffith, P. Lynn and T. Swift. Pneumatic exomuscle system and method.